

A Numerical Study of Swirl Flow in Pipes

Application to Inline Swirl Separators

by

Alireza Karimpoorheidari (AK.)

in partial fulfillment of the requirements for the degree of

Master of Science
in Petroleum Engineering

at the Delft University of Technology,
to be defended publicly on Friday December 13, 2019 at 10:00.

Student number:	4622219	
Under guidance and supervision of:	Dr. Luis Portela	TU Delft, supervisor
Thesis committee:	Dr. Luis Portela	TU Delft, supervisor
	Dr. Pacelli Zitha	TU Delft
	Dr. Denis Voskov	TU Delft

An electronic version of this thesis is available at <http://repository.tudelft.nl/>.

Abstract

For many decades, conventional gravitational separators have been the backbone of the fluid separation in the oil and gas industry. The stricter environment regulation for purification of the recycled water, together with a tighter profitable margin of the produced oil, requires more efficient and faster separators. Inline swirl separator uses centrifugal acceleration up to hundreds of gravitational accelerations to perform separation in a much faster time. However, its efficiency is still lower than the industry expectations. There are essential geometric parameters such as swirl intensity and the collector tube, and vital operating conditions such as flow-rate at the entrance and mass flow-rate at each exit that impact the dynamics behavior of swirl flow in the pipe. The dynamic behavior of the swirl flow determines the efficiency of the apparatus. Thus, the main objective is to understand the dynamics of the single-phase swirl flow in the pipe and determine an inline swirl separator that presents sufficient efficiency. The first part of the study focuses on a better understanding of the dynamic behavior of the swirl flow in a pipe. The second part utilizes the results from the first stage to determine an inline swirl separator that presents sufficient efficiency.

The performed numerical study suggests that the dynamic behavior of swirl flows in a pipe is determined by the intensity of the swirl flow, which is quantified by the swirl number. The swirl intensity shapes the axial velocity profile at the core of the vortex. When the swirl number increases beyond a critical number, a columnar vortex appears, with a reverse flow along with the center of the entire tube. The swirl intensity decays along the wall of the pipe; the swirl intensity and the decay of it form the shape of the axial velocity profile. In case the disturbance of the flow results in a stagnation point at the vortex axis, it may develop a vortex breakdown. The vortex breakdown in high Reynolds numbers ($Re_b > 100,000$) is a function of the swirl number, and the instability at the vortex core increases by increasing the swirl intensity. Furthermore, the results show that the stability of the vortex is a function of the Reynolds number. Considerable reduction of the Reynolds number kicks in the effect of viscous forces, which stabilize the vortex core. Reynolds and swirl numbers determine the dynamic of the low Reynolds number but turbulent, swirl flow. Therefore, the industry needs to rely on Reynolds Averaged Navier-stokes (RANS) simulations; Direct Numerical Simulation predictions obtained at much lower Reynolds numbers may not predict the occurrence of the vortex breakdown inside the pipe.

These findings show that there are essential design considerations, which determine the efficiency of the swirl separator. Thus, a combination of the geometry parameters and the swirl flow characteristics should be considered to avoid the reverse flow zone and vortex breakdown inside the inline separator. One of the vital elements of the inline swirl separator is the collector tube. The study shows that the collector tube at the neutral flow split, with no bias of the mass flow-rate at each outlet, changes the velocity to the extent that the reverse flow zone for $Sw=0.5$ is eliminated. Pressure actuators can control the flow; therefore, controlling the flow split at both outlets. The numerical results show that an additional percentage of flow split enhances efficiency by eliminating the reverse flow zone for the higher swirl numbers. Additionally, the study reveals the counter effect of the extreme flow splits, which hinders the efficiency of the inline swirl separator. These optimal settings for the geometry of this research were found at swirl number 1.6 and flow split of 50%.

Contents

List of Tables	iv
List of Figures	v
1 Introduction	1
1.1 Research	2
1.2 Methodology	2
1.3 Thesis outline	2
2 Theory of swirling pipe flows	3
2.1 Equations of vortex motion	3
2.1.1 Vorticity and circulation	3
2.1.2 Velocity and Vorticity equations in cylindrical coordinate system	3
2.2 Characteristics of swirl flows	4
2.2.1 The swirl number	4
2.2.2 Helicity	4
2.3 Vortex structure	5
2.3.1 Rankine Vortex	5
2.3.2 Vortex breakdown	5
2.3.3 Precessing Vortex Core	6
2.3.4 Decay of swirl	6
2.4 Relevant Parameters	6
2.4.1 Flow split	6
2.4.2 Forces on droplets	6
2.4.3 The droplet equation of the motion	7
2.4.4 Timescales	8
2.4.5 Dimensionless numbers	8
3 Computational fluid dynamics	9
3.1 Turbulence modeling	9
3.2 Wall function	11
3.3 Computational mesh	11
3.4 Flow straightener	12
3.5 Boundary Conditions	13
3.5.1 Initial velocity distributions	13
3.5.2 Outlet boundary conditions	15
3.6 Comparison with the experiments and numerical models	15
3.6.1 Inside of the separator tube $0 < Z < 1.5 m$.	15
3.6.2 Just upstream of the collector tube $1.6 < Z < 1.7 m$.	15
3.7 Numerical simulations cases	17
3.7.1 Fundamental study of swirl flows	18
3.7.2 Inline swirls separators.	19
4 Fundamental study of swirl flows	21
4.1 Mean quantities analysis	21
4.1.1 Axial velocity profiles	21
4.1.2 Tangential velocity profiles.	23
4.1.3 Radial velocity profiles	25

4.2	Swirl flow dynamic and structure	25
4.2.1	Relative helicity	25
4.2.2	Precessing vortex core and pressure tomography of swirl flow	27
4.2.3	Vortex breakdown	29
4.2.4	Turbulent swirl flows	31
4.2.5	Laminar swirl flows	31
4.3	Flow morphology	33
5	Inline swirls separators	34
5.1	An accurate velocity field	34
5.1.1	Indispensable change	35
5.1.2	Collector tube and velocity field	35
5.2	Design considerations	36
5.2.1	Essential design factors	36
5.2.2	The optimum Inline Swirl Separator	38
5.2.3	Separator efficiency	38
6	Conclusions and recommendations	40
6.1	Conclusions.	40
6.2	Recommendations	40
A	Initial velocity distributions	42
B	Time-Averaged Velocity Profiles	43
C	Wall-pressure and velocity components signals	45
D	Circular motion of the axis of the vortex	46
E	Similarity Turbulent Vortex flow	48
F	Comparison between turbulent and laminar Vortex flow	50
G	Inline swirl separator design $S_w = 0.5$	52
H	Inline swirl separator design $S_w = 1.6$	55
I	Inline swirl separator design $S_w = 2.5$	58
	Bibliography	61

List of Tables

3.1	Quadratic Reynolds stress model coefficients	10
3.2	Computational mesh statistics	12
3.3	Fundamental study of swirl flows cases (swirl intensity vs. turbulent & viscous forces effects)	18
3.4	Design of swirl separators cases (swirl intensity vs. flow split); $Re_b = 150,000$	19
5.1	Specification of the oil that $S_w = 1.6$ & $F_s = 50\%$ separates effectively - constant brine specification	39
C.1	Equation of the signals - $S_w = 0.5$ - Velocity signals at the location of the maximum U_θ , and Pressure signals at the wall cross-section	45
C.2	Equation of the signals - $S_w = 3.6$	45

List of Figures

1.1	Schematic of inline swirl separator - static swirl element, separation tube, and collector tube. . .	1
2.1	Global classification of swirl types [7]	5
2.2	Photographs of vortex breakdowns, with the flow generally from left to right. (a) Bubble form; (b) Spiral form. [9]	5
3.1	Computational mesh on cross-sectional plane in separator's tube, $z = 1\text{ m}$	12
3.2	Internal swirl element with key features Slot [2]	14
3.3	Test-case domain; the boundary conditions as per describe in section 3.19, 3.25,3.5.1 & 3.5.2, design as per Van Campen setup [1] - $R_b = 181,000$	15
3.4	Comparison of the axial velocities at different axial distances.Grey symbols Van Campen [1], grey dashed Slot's results[2], and colored symbols are this research	16
3.5	Comparison of the tangential velocities at different axial distances.Grey symbols Van Campen [1], grey dashed Slot's results[2], and colored symbols are this research	16
3.6	Comparison of the axial velocities at vicinity of the collector- $Z= 1.70\text{ m}$.Grey symbols Van Campen [1] and grey dashed Slot's results[2], and colored symbols are this research	17
3.7	Comparison of the tangential velocities at vicinity of the collector- $Z= 1.70\text{ m}$.Grey symbols Van Campen [1] and grey dashed Slot's results[2], and colored symbols are this research	18
3.8	Boundary conditions used for simulations of fundamental study cases	19
3.9	Boundary conditions used for simulations of design study cases	20
4.1	Dimensionless time-averaged axial velocity contours and profiles for various S_w on the plane $\frac{X}{D} = 0$ and $\frac{Z}{D} = 3, 5, 17\&19$	22
4.2	Dimensionless time-averaged axial velocity contours and profiles for various high S_w on the plane $\frac{X}{D} = 0$ and $\frac{Z}{D} = 3, 5, 17\&19$	23
4.3	Dimensionless time-averaged tangential velocity contours and profiles for various S_w on the plane $\frac{X}{D} = 0$ and $\frac{Z}{D} = 3, 5, 17\&19$	24
4.4	Dimensionless time-averaged tangential velocity contours and profiles for various S_w on the plane $\frac{X}{D} = 0$ and $\frac{Z}{D} = 3, 5, 17\&19$	24
4.5	Tangential velocity profiles Steenbergen [7]	25
4.6	Dimensionless time-averaged helicity contours for various S_w on the axial cross-section plane- $X=0$	25
4.7	Dimensionless time-averaged helicity contours on various S_w on the transversal cross-section planes - $Z/D = 5, 10 \& 15$	26
4.8	Flow streamlines on various S_w (Rake is created at $Z/D = 10$ plane. The relative helicity is used to color the streamlines	27
4.9	Fourier transformation of the axial, tangential, radial velocities, at the point of the maximum U_θ and associated wall pressure at the same cross-section	28
4.10	Fourier transformation of the axial, tangential, radial velocities, at the point of the maximum U_θ and associated wall pressure at the same cross-section	28
4.11	Circular motion of the axis of the vortex in three projections - $S_w = 3.6$	30
4.12	Dimensionless axial velocity - stagnation point at $Z/D=13.18\text{m}$ - $S_w = 2.5$	30
4.13	Relative helicity flow structure- stagnation point at $Z/D=13.18\text{m}$ - $S_w = 2.5$	31
4.14	Dependence of swirl stability on Reynolds number - Relative helicity	32
4.15	Comparison between unsteady laminar and turbulent swirl flows in a pipe	32
4.16	Prediction of the flow morphology based on Reynolds and swirl numbers- Axes are not scaled	33
5.1	Intensified swirl design performance results - Cross-sectional at $X=0$	35
5.2	Dimensionless pressure, axial, and tangential velocity field at various trasversal planes.	35

5.3	Effect of the collector tube and comparison with no collector- $S_w = 0.5$ & $F_s = 25\%$	36
5.4	Effect of the flow split on velocity field at entrance of the collector tube. Top: $S_w = 1.6$ & Bottom $S_w = 2.5$	37
5.5	Dimensionless time-averaged axial, tangential, and pressure field. Colored flow-streamline $S_w = 1.6$	39
5.6	The oil droplet trajectory for $D_o = 100\mu m$. & $API = 30^\circ$ - Based on simulated velocity field	39
A.1	pictures 1,2,3- Dirkwager[8] & 4: Van Campen [1] experiments for different swirl elements. Solid lines are simplified distribution - pictures from cross-section, close to the inlet $Z/D < 4$	42
A.2	Left: Dirkwager & Right: Van Campen experiments for the weak, strong, and big swirl elements- the circles indicate the radial position of the maximum and minimum of the axial velocity at inlet position $Z/D = 10$,	42
B.1	Dimensionless time-averaged radial velocity contours for various S_w on the cross-sectional and transversal planes	43
B.2	Dimensionless time-averaged radial velocity contours for various S_w on the cross-sectional and transversal planes	44
B.3	Dimensionless time-averaged axial,radial, and tangential velocity profiles for various S_w on the transversal planes	44
D.1	Circular motion of the axis of the vortex at $Z=1.9m$ - $S_w = 1.6$	46
D.2	Circular motion of the axis of the vortex at $Z=1.9m$ - $S_w = 0.5$	47
E.1	Dimensionless time-averaged axial velocity profiles on various Reynolds numbers- $\frac{X}{D} = 0$	48
E.2	Dimensionless time-averaged axial velocity profiles of various Reynolds numbers- $\frac{Z}{D} = 3, 5, 17\&19$	48
E.3	Dimensionless time-averaged tangential velocity profiles of various Reynolds numbers- $\frac{X}{D} = 0$	48
E.4	Dimensionless time-averaged Tangential velocity profiles on various Reynolds numbers- $\frac{Z}{D} = 3, 5, 17\&19$	49
F.1	Comparison between unsteady laminar and turbulent swirl flows in a pipe -Axial Velocity profile	50
F.2	Comparison between unsteady laminar and turbulent swirl flows in a pipe -Tangential Velocity profile	51
F.3	Comparison between unsteady laminar and turbulent swirl flows in a pipe, cross-section profile in the middle of the pipe	51
F.4	Comparison between unsteady laminar and turbulent swirl flows in a pipe - Structure of the flow	51
G.1	Dimensionless time-averaged axial velocity for various Flow Splits - $\frac{X}{D} = 0$	52
G.3	Dimensionless time-averaged tangential velocity for various Flow Splits - $\frac{X}{D} = 0$	52
G.2	Dimensionless time-averaged axial velocity for various Flow Splits - Dimensionless radial coordinate	53
G.4	Dimensionless time-averaged tangential velocity for various Flow Splits - Dimensionless radial coordinate	53
G.5	Dimensionless time-averaged pressure on various Flow Splits - Dimensionless radial coordinate	54
G.6	Flow streamlines on various Flow Split (Rake is created on $Z/D = 10$ plane) - The colored streamlines are used to differentiate them	54
H.1	Dimensionless time-averaged axial velocity for various Flow Splits - $\frac{X}{D} = 0$	55
H.3	Dimensionless time-averaged tangential velocity for various Flow Splits - $\frac{X}{D} = 0$	55
H.2	Dimensionless time-averaged axial velocity for various Flow Splits - Dimensionless radial coordinate	56
H.4	Dimensionless time-averaged tangential velocity for various Flow Splits - Dimensionless radial coordinate	56
H.5	Dimensionless time-averaged pressure for various Flow Splits - Dimensionless radial coordinate	57
H.6	Flow streamlines for various Flow Split, Rake is created on $Z/D = 10$ plane - The colored streamlines are used to differentiate them	57

I.1	Dimensionless time-averaged axial velocity for various Flow Splits - $\frac{X}{D} = 0$	58
I.3	Dimensionless time-averaged tangential velocity for various Flow Splits - $\frac{X}{D} = 0$	58
I.2	Dimensionless time-averaged axial velocity for various Flow Splits - Dimensionless radial coordinate	59
I.4	Dimensionless time-averaged tangential velocity for various Flow Splits - Dimensionless radial coordinate	59
I.5	Dimensionless time-averaged pressure for various Flow Splits - Dimensionless radial coordinate	60
I.6	Flow streamlines for various Flow Split, Rake is created on $Z/D = 10$ plane - The colored streamlines are used to differentiate them	60

1

Introduction

Technology and innovation continuously displace conventional practices. The advancements of computational power increase the pace of the old methodology transformations. For many decades, conventional gravitational separators have been the backbone of the fluid separation in the oil and gas industry. However, the recent transformations in the energy sector demand an alternative method of separation that delivers the multi-phase separation more efficiently. The vast use of the swirling flow in cyclone separators made it an alternative multi-phase flow splitter to replace the conventional gravitational separators.

The idea behind harnessing the swirl flow in a pipe is to reduce the size and weight, and to enhance the efficiency of the multi-phase separator. The separator is composed of a separation tube that provides the housing, a static swirl element, and a collector tube inside the pipe. The stationary swirl element generates a vortex that provides a centrifugal force up to hundreds of gravitational accelerations. The vortex concentrates the lighter fluid at the center of the pipe; so, the collector separate it from the denser fluid, figure 1.1. Swirl flow motions are known for the decay of the swirl intensity inside the pipe, the reverse flow zone, and the vortex breakdown. The flow swirl motion acts as a centrifugal force on the pipe wall, causing the wall pressure to become higher than the pressure at the center of the tube, roughly, the pressure gradient in the axial direction is determined by the fluid density, ρ , tangential velocity, U_θ , $\frac{\rho U_\theta^2}{r} \approx \frac{\partial P}{\partial r}$. The radial pressure gradient decreases along the downstream direction because of the decay of the tangential velocity. Thus, the axial gradient of the wall pressure is negative. However, the axial pressure gradient at the center of the tube could become positive, due to the decay of the radial pressure gradient along the downstream direction. This positive axial pressure gradient, at the center of the tube, could cause a reverse flow in the separation tube. Furthermore, the flow disturbance could develop a vortex breakdown. The reverse flow zone hinders the efficiency, and the vortex breakdown terminates the separation process. Despite the basic concept, the operation and dynamics of the swirl separators are still unclear.

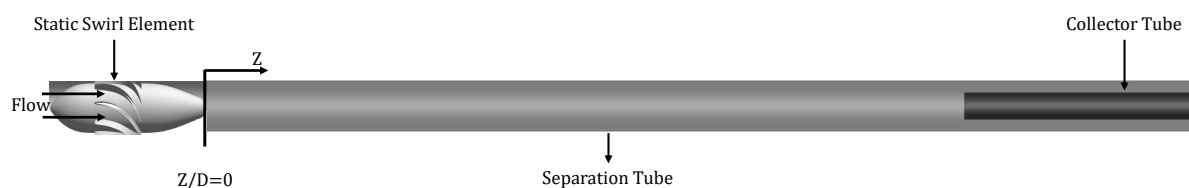


Figure 1.1: Schematic of inline swirl separator - static swirl element, separation tube, and collector tube.

Moreover, previous researches highlighted several hurdles in the operation of the inline swirl separator. Van Campen [1] concluded that his work is not ready for commercial development of the inline swirl separator. Slot [2] referred that the numerical simulation fails to predict the behavior of the emulsion seen in the center of the pipe in the experiments, Star [3] highlighted that the PIV measurements were not reproducible and resulted in significant uncertainties in the quantities computed, such as the pressure distribution and the swirl number. Zoeten [4] concluded that the mechanistic model predicts the inline swirl separator efficiency far-off from experimental measurements.

It appears that a better understanding of the behavior of the dynamic of swirl flows is required. Unveiling the dynamic of the flow inside the swirl separator, in order to determine the reason behind low-efficiency, is the first building block to overcome the low separation efficiency of the inline swirl separators.

1.1. Research

Previous researches were conducted based on the concept that a strong static swirl element delivers enough centrifugal force to perform liquid-liquid separation of two fluids with small differences in specific gravity. The current research goes one step further and reviews the essential understandings that are substantial to a successful separation.

The main objective is to understand the dynamics of the swirl flow in the pipe, in the absence of the collector tube, and how several parameters influence the dynamics of the swirl flow. Here, the focus is to understand the effect of the non-dimensional Reynolds and swirl numbers on the behavior of the swirl motion. Thus, the geometry of the pipe remains intact during the research. The non-dimensional numbers are explained in chapter 2. The first part of the research reveals the flow morphology, and relates the instability of the vortex to the axial velocity profiles; and it shows how the vortex breakdown is related to the Reynolds number and the swirl number.

The second objective is to determine an inline swirl separator that presents sufficient efficiency. The utilization of the results from the previous stage allows constructing the essential design considerations. Furthermore, this research targets to investigate the effect of the collector tube in the downstream of the pipe. This thesis reviews the functionality of the separator based on the swirl number and the mass flow-rate through each of the outlets. In the last part, some considerations are made on the design of the optimum inline swirl separator for the separation of crude oil from brine.

1.2. Methodology

The geometry of the tube separator remains constant in both stages of the research. In the second stage, the collector tube is placed inside the separation tube to build the inline swirl separator. Commercial software Ansys 19.1 is exploited to create a mesh that contains over three million hexahedral elements; also, the same software is used to solve the governing equations. Ansys 19.1 discretizes the equations using a finite-volume formulation. Control volumes are constructed around the nodes of the elements. These control volumes are employed as the volumes on which the integral conservation form of the Navier-Stokes equations is applied. A total of 28 cases are considered in this thesis.

1.3. Thesis outline

This thesis consists of six chapters. The first chapter is the introduction and covers the research outline. The second chapter serves as the fundamental background and provides a brief introduction to the governing equations. The third chapter describes the CFD methodology used, in some detail; also, it provides the detail of the numerical domain structure, the mesh construction, and the solver settings. At the end of this chapter, the test-case results are compared with the previous experimental and numerical studies. Chapter four covers the fundamental studies of the swirl flow in the pipe, and presents the swirl flow morphology, based on the Reynolds and swirl numbers. The results from chapter four are utilized in chapter five, which covers the inline swirl separator setup and analysis the performance of different separators in the supplementary appendixes G, H, and I. In the final chapter, a conclusion is given, and recommendations for further research are provided.

2

Theory of swirling pipe flows

This chapter provides a brief introduction to the governing equations and properties required to the analysis the swirl flows. Chapters 4 and 5 utilize the equations introduced to present and discuss the result of the numerical studies. In section 2.1, the equation of motion is provided, and in sections 2.2 & 2.3, the behavior and characteristics of swirl flows are illustrated, and at the end of this chapter, in section 2.4 the relevant parameters are reviewed.

2.1. Equations of vortex motion

2.1.1. Vorticity and circulation

The vorticity vector is a vital term in the fluid dynamics, and it is obtained by taking the curl of the velocity vector. By definition, irrotational motion has zero vorticity.

$$\vec{\omega} = \nabla \times \vec{u} = \varepsilon_{ijk} \frac{\partial u_k}{\partial x_j} \quad (2.1)$$

The interpretation of the vorticity lies in the fact, that it is equal to the twice the local angular velocity of a fluid element.

$$\Omega = \frac{1}{2} \omega \quad (2.2)$$

In conjunction with vorticity, circulation Γ provides a scalar definition of the dynamics of rotating flows. Circulation is the curvilinear integral of the velocity field. If vorticity describes the local feature of rotating flows, circulation can be referred as a macroscopic measure of the rotation. By applying the stockes theorem, if the curve is reducible, the linear integral is transformed to surface integral.

$$\Gamma = \oint_C \vec{u} \cdot d\vec{l} = \iint_S (\nabla \times \vec{u}) \cdot \vec{n} dA = \iint_S (\vec{\omega} \cdot \vec{n}) dA \quad (2.3)$$

Here A is the surface area of bounded by circuit l ; and n is the unit vector normal to the surface.

2.1.2. Velocity and Vorticity equations in cylindrical coordinate system

In cylindrical coordinate, z , r , and θ represent axial, radial, and azimuthal direction, respectively. In the same order, u_z , u_r , and u_θ correspond to axial, radial, and azimuthal components of the velocity vector. The Navier-Stokes equations of incompressible fluids in the cylindrical coordinates read:

$$\frac{\partial u_r}{\partial t} + u_r \frac{\partial u_r}{\partial r} + \frac{u_\theta}{r} \frac{\partial u_r}{\partial \theta} + u_z \frac{\partial u_r}{\partial z} - \frac{u_\theta^2}{r} = -\frac{1}{\rho} \frac{\partial p}{\partial r} + \nu \left[\frac{1}{r} \frac{\partial}{\partial r} \left(r \frac{\partial u_r}{\partial r} \right) + \frac{1}{r^2} \frac{\partial^2 u_r}{\partial \theta^2} + \frac{\partial^2 u_r}{\partial z^2} - \frac{u_r}{r^2} - \frac{2}{r^2} \frac{\partial u_\theta}{\partial \theta} \right] + g_r \quad (2.4)$$

$$\begin{aligned} \frac{\partial u_\theta}{\partial t} + u_r \frac{\partial u_\theta}{\partial r} + \frac{u_\theta}{r} \frac{\partial u_\theta}{\partial \theta} + u_z \frac{\partial u_\theta}{\partial z} + \frac{u_r u_\theta}{r} \\ = -\frac{1}{(\rho r)} \frac{\partial p}{\partial \theta} + \nu \left[\frac{1}{r} \frac{\partial}{\partial r} \left(r \frac{\partial u_\theta}{\partial r} \right) + \frac{1}{r^2} \frac{\partial^2 u_\theta}{\partial \theta^2} + \frac{\partial^2 u_\theta}{\partial z^2} - \frac{u_\theta}{r^2} + \frac{2}{r^2} \frac{\partial u_r}{\partial \theta} \right] + g_\theta \end{aligned} \quad (2.5)$$

$$\begin{aligned} \frac{\partial u_z}{\partial t} + u_r \frac{\partial u_z}{\partial r} + \frac{u_\theta}{r} \frac{\partial u_z}{\partial \theta} + u_z \frac{\partial u_z}{\partial z} = -\frac{1}{\rho} \frac{\partial p}{\partial z} + \\ \nu \left[\frac{1}{r} \frac{\partial}{\partial r} \left(r \frac{\partial u_z}{\partial r} \right) + \frac{1}{r^2} \frac{\partial^2 u_z}{\partial \theta^2} + \frac{\partial^2 u_z}{\partial z^2} \right] + g_z \end{aligned} \quad (2.6)$$

while the continuity equation is given by

$$\frac{\partial u_z}{\partial z} + \frac{1}{r} \frac{\partial r u_r}{\partial r} + \frac{1}{r} \frac{\partial u_\theta}{\partial \theta} = 0 \quad (2.7)$$

The equations of vorticity are derived by applying the curl operator to both sides of the Navier-stokes equations (2.6, 2.4, and 2.5). The pressure and gravity terms vanish because the curl of a gradient reads zero. The vorticity vector is composed of the following components:

$$\omega_z = \frac{1}{r} \frac{\partial r u_\theta}{\partial r} - \frac{1}{r} \frac{\partial u_r}{\partial \theta} \quad (2.8)$$

$$\omega_r = \frac{1}{r} \frac{\partial u_z}{\partial \theta} - \frac{\partial u_\theta}{\partial z} \quad (2.9)$$

$$\omega_\theta = \frac{\partial u_r}{\partial z} - \frac{\partial u_z}{\partial r} \quad (2.10)$$

The primary vorticity transport equation in this study is the axial vorticity equation. Thus, here only the axial transport equation is shown.

$$\begin{aligned} \frac{\partial \omega_z}{\partial t} + u_z \frac{\partial \omega_z}{\partial r} + u_r \frac{\partial \omega_z}{\partial r} + \frac{u_\theta}{r} \frac{\partial \omega_z}{\partial \theta} = \omega_z \frac{\partial u_z}{\partial z} + \omega_r \frac{\partial u_z}{\partial r} + \frac{\omega_\theta}{r} \frac{\partial u_z}{\partial \theta} + \\ \nu \left[\frac{1}{r} \frac{\partial}{\partial r} \left(r \frac{\partial \omega_z}{\partial r} \right) + \frac{1}{r^2} \frac{\partial^2 \omega_z}{\partial \theta^2} + \frac{\partial^2 \omega_z}{\partial z^2} \right] \end{aligned} \quad (2.11)$$

2.2. Characteristics of swirl flows

2.2.1. The swirl number

A non-dimensional number quantifies the swirl intensity in the swirling pipe flow: swirl number, S_w . The swirl number presents the angular momentum in the flow and its streamwise decay. Hence, it is coupled with the tangential wall shear stress. This thesis utilizes Kitoh's definition of the swirl number.[5]

$$S_w = \frac{\int_0^R 2\pi\rho U_z U_\theta r^2 dr}{\rho\pi R^3 U_b^2} \quad (2.12)$$

The angular momentum flux is made dimensionless by the bulk velocity, pipe radius and density.

2.2.2. Helicity

Helicity is an invariant property of an ideal flow, one of the four invariant, and unlike the kinetic energy is not sign definite. Consider a localized vorticity distribution, $\vec{\omega} = \nabla \times \vec{u}$ (2.1.1), the helicity of the domain that flow exist is defined by

$$\mathcal{H} = \iiint_V \vec{u} \cdot \vec{\omega} dV \quad (2.13)$$

We utilise helicity to illustrate dynamic structures of the swirl flow in a pipe.

Helicity density

The helicity density $\vec{u} \cdot \vec{\omega}$ indicates how close a streamline (an integral curve of the velocity field) is to right hand-side screw (positive helicity) or left-hand one (negative helicity).

Relative helicity

Helicity density is a scalar quantity, and in a turbulent flow there will be a region that the value of $|\vec{u} \cdot \vec{\omega}|$ will be near to maximum, therefore \vec{u} is parallel to $\pm \vec{\omega}$. In such a region the nonlinear term of $\vec{u} \times \vec{\omega}$ is small. The ratio of the helicity density to the maximum possible magnitude of the helicity density defines the relative helicity.

$$\frac{\vec{u} \cdot \vec{\omega}}{|\vec{u}||\vec{\omega}|} = \frac{(\nabla \times \vec{u}) \cdot \vec{u}}{|\nabla \times \vec{u}||\vec{u}|} \quad (2.14)$$

Relative helicity is the cosine of the angle between velocity and vorticity[6].

2.3. Vortex structure

The swirl conditions usually are classified in three major types. This research focuses on the first two types, and the definition of the vortex structure is given based on the similarity they resemble these types.

- Concentrated Vortex (CV) is characterized by a concentration of the vorticity in a region near the pipe center, surrounded by an annulus of low vorticity.
- Solid body (SB) is usually obtained by guiding the fluid either through a pipe section containing a twisted tape, or through a rotating pipe section filled with a honeycomb.
- Wall Jet (WJ) is created by allowing swirling fluid to enter the pipe in the inlet plane through an annular hole adjacent to the wall.

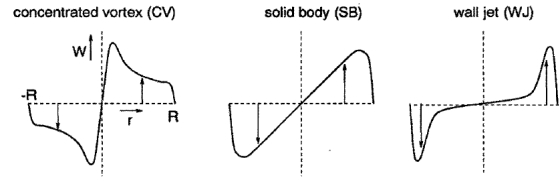


Figure 2.1: Global classification of swirl types [7]

2.3.1. Rankine Vortex

The vortices are also classified based on the tangential component of the velocity vector. The two major types are Rankine and Gaussian vortex; neither of them has a radial component. The experimental data exhibit that high swirl flow in the pipe resembles more the Rankine tangential velocity distribution. Steenbergen [7], Drikzwagenr [8], and Van Campen [1] experiments revealed this type of vortex. This research uses their experimental data to construct the inlet boundary conditions. Appendix A presents a snapshot of Rankine the vortex from all three experimental. The tangential velocity component is approximated by:

$$U_{\theta}(r, z) = \begin{cases} U_{\theta_z} & \text{for } R_c < r < R \\ \frac{r}{R_c} U_{\theta_z} & \text{for } 0 \leq r \leq R_c \end{cases} \quad (2.15)$$

2.3.2. Vortex breakdown

Leibovich [10] defines a vortex breakdown as a flow disturbance, which most usefully is identified by the development of a stagnation point on the vortex axis, followed by a region of reversal axial flow, encapsulated by a much-swollen stream surface. Leibovich classifies the vortex breakdown in six types. Two categories appear to be predominant: the bubble-like breakdown and the spiral breakdown. Faler [9] defines that, in the bubble-like structure, the axial velocity becomes positive again after the stagnation point at each radial position. Beyond this region, a new vortex structure is established with an expanded core. The entire region of vortex breakdown becomes unsteady, and the forward and backward movement is unpredictable.

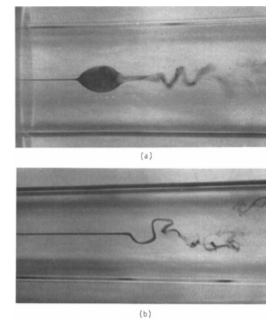


Figure 2.2: Photographs of vortex breakdowns, with the flow generally from left to right. (a) Bubble form; (b) Spiral form. [9]

2.3.3. Precessing Vortex Core

As the swirl number reaches a critical number of 0.5, a reverse flow zone is formed at the center of the vortex's core, and as the Reynolds number increases, an instability develops that is known as the vortex breakdown. Further increase of Reynolds number causes the precessing vortex core (P.V.C.). Yazdabadi [11] shows that P.V.C. consists of the rotation of the center of the vortex around a center, which may not coincide with the pipe axis. He explains that P.V.C. has a regular frequency and amplitude, and dependent upon the system configuration and flow-rate. Actual displacement of the center of the vortex and precession around the axis of the pipe causes tangential velocities, a new rotating coordinate center. Conservation of the angular momentum flux based on this new coordinate center explains why the P.V.C. phenomena accelerate the tangential component.

2.3.4. Decay of swirl

An exponential decay function gives the decay of the swirl number in the literature:

$$S_w(z) = S_w(0) \exp \frac{-C_{decay}(z-Z_0)}{2R} \quad (2.16)$$

where $S_w(0)$ is the swirl number at position Z_0 , and C_{decay} is the decay coefficient.

Dirkzwager [8] measurements revealed that the decay coefficient is not constant, and it changes with the swirl number. This research, later on, demonstrates that the swirl decays faster for intensify swirl flows. Some scholars measure the decay of the swirl based on decay of the tangential velocity. However, the precessing vortex core can accelerate the tangential component. A careful review is required when the efficiency of swirl equipment is compared based on the swirl decay model, as the coefficient is not constant for different swirl numbers in one apparatus.

2.4. Relevant Parameters

This section covers the parameters or factors that were introduced or discussed in this research, and defines them in advance.

2.4.1. Flow split

A tube is placed at the end of the swirl separator tube, with its center located at the pipe axis. This thesis refers to this tube as collector-tube. The placement of the collector tube will split the outlet of the pipe into a Heavy Phase Outlet (HPO) and a Light Phase Outlet (LPO). These outlets and their boundary conditions are explained in section 3.5.2. Van Campen [1] used a pressure valve to control the mass flow-rate through each of these outlets. The distribution of the flow streams is called Flow Split (FS).

$$FS = \frac{\Phi_{LPO}}{\Phi_{HPO} + \Phi_{LPO}} \quad (2.17)$$

with Φ the volumetric flow-rate. The numerical setup considered the flow split as the ratio of the mass flow-rate crossing through each outlet, as the fluid is incompressible. The details of the geometry of the separator are shown in section 3.7.

2.4.2. Forces on droplets

The interaction between continuous phase and the dispersed phase exerts several of the forces on the droplet. Here, the forces that are relevant to inline swirl separator selection are listed.

Interfacial force

In a dispersed two-phase flow, the oil droplets exist due to interfacial tension force, which keeps them together.

$$F_\sigma = \pi \sigma D \quad (2.18)$$

with σ the surface tension between oil droplets and the continuous phase (brine). The breakup of the dispersed flow is beyond the objective of this study. However, when the pressure or velocity oscillations are exerted on the droplet and exceed the surface tension, the droplet breaks.

Buoyancy force

The radial pressure gradient of the swirling flow exerts a centripetal force on the oil droplet with volume V_d

$$F_{centripetal} = \frac{V_d \rho_c U_\theta^2}{r} \quad (2.19)$$

Where ρ_c and U_θ are the density of the continuous phase and tangential velocity of the continuous phase at radius r , respectively. Furthermore, the centrifugal force acts in the opposite direction to keep the oil droplet at a given radial position r , is:

$$F_{centrifugal} = \frac{V_d \rho_d U_\theta^2}{r} \quad (2.20)$$

Where ρ_d is the density of the oil. Therefore, the buoyancy force acting on the oil droplet and pointing towards the center of the swirl flow is given by

$$F_B = \frac{V_d \Delta \rho U_\theta^2}{r} \quad (2.21)$$

where $\Delta \rho = \rho_c - \rho_d$

Drag force

The droplet accelerates in the radial direction because of the inward direction of the buoyancy force, the difference between radial velocity of the droplet and the surrounding liquid induces a drag force which is counteracting the buoyancy force. The drag force is given by:

$$F_D = \frac{1}{2} \rho_c C_D A_d |\vec{U}_d - \vec{U}_c| (\vec{U}_d - \vec{U}_c) \quad (2.22)$$

Where ρ_c , C_D , A_d , U_d , and U_c are the density of the continuous phase, the drag coefficient, the area of the oil cross-section, the droplet velocity and the continuous phase velocity, respectively.

We neglected the Basset force due to the order of the magnitude. Additionally, virtual mass and Saffman lift forces are not considered in the droplet trajectory calculation. Thus, we do not introduce them in here.

2.4.3. The droplet equation of the motion

The droplet trajectory is used to define the suitability of the selected inline swirl separator. In order to derive the oil droplet trajectory, we made several assumptions. The backbone of this simplification is the balance of the forces exerted on the dispersed oil droplets. Therefore, the buoyancy force and drag force are balanced. An initial calculation of the relative velocity (hereafter radial velocity of the oil droplet) revealed that the droplet motion is not a Stokes flow. Hence, the drag coefficient is estimated from:

$$C_D = 0.445 + \frac{24}{Re} \quad (2.23)$$

while Re is the droplet Reynolds number which is calculated from

$$Re = \frac{\rho_c D_d U_r}{\mu_c} \quad (2.24)$$

Where U_r is the radial velocity of the droplet. We assume the following:

- The dispersed oil droplet is spherical, no breakup
- Oil droplet is in a quasi-steady state, means the forces acting on the droplet are balanced.
- Flow-field is in a quasi-steady state, means the mean-flow properties do not change with the time
- The effect of turbulence on the droplet motion is neglected. Only the forces due to the mean velocity field are considered
- Distribution of the velocity for two-phase flow is similar to that of single-phase flow.

the the radial velocity of the oil droplet is given by:

$$U_r^2 \left(0.445 + \frac{24}{Re} \right) = \frac{4}{3} D_d \frac{\Delta \rho}{\rho_c} \frac{U_\theta^2}{r} \quad (2.25)$$

The above equation shows that the radial velocity of the oil droplet can be calculated from the velocity profile of the continues fluid. Additionally, the radial velocity of the droplet is a function of the droplet size, time, and the velocity field inside the inline swirl separator.

2.4.4. Timescales

In the turbulent flow, the time of the microstructure is related to the dissipation-rate and the viscosity. Resolution of the equations down to the kolmogrov scale, Direct Numerical Simulation, for the high reynolds number is not feasible. We use Reynolds-Averaged Navier-stokes (RANS) unsteady simulation. The mesh and time step need to be chosen such that they can resolve the dynamic of the unsteady RANS equations.

Here, the time scale is referred to as the time is required to capture flow physics. Swirl flow is known for double pressure, static, and dynamic pressure. However, another phenomenon that needs to be resolved is the temporal behavior of the flow.

The angular velocity of the swirl motion at the core of the Rankine vortex defines the time scale. It appears that the highest swirl element generates swirl motion around 850Hz, (rotation per minute) at the core of the Rankine vortex. It was required to reduce the solution time to 2.5×10^{-4} seconds in order to capture the temporal behavior of the flow. The time-averaged data shows a little improvement at 2.5×10^{-4} seconds, so the time was increased to 5×10^{-4} seconds for the time-average studies.

2.4.5. Dimensionless numbers

Mass, length, and time are independent dimensions. The parameters in this research are

- Geometry: L & D - Length and diameter of the pipe
- Properties : ρ & μ - Density and viscosity of the fluid
- Velocity profiles : U_b , U_z & U_θ - Bulk velocity and the velocity profiles at inlet

The frequent eight non-dimensional numbers that are used:

$$a: \frac{Z}{D} \qquad b: \frac{r}{D} \quad (2.26)$$

a and b present dimensionless axial and radial length, respectively.

$$c: \frac{U_z}{U_b} \qquad d: \frac{U_\theta}{U_b} \qquad e: \frac{U_r}{U_b} \quad (2.27)$$

c,d, and e present dimensionless axial, tangential, and radial velocity, respectively.

$$f: \frac{P}{\frac{1}{2} \rho U_b^2} \qquad g: F_s = \frac{\dot{m}}{\pi \rho U_b \frac{D^2}{4}} \qquad h: Re = \frac{U_b D}{\nu} \quad (2.28)$$

f,g, and h present dimensionless pressure, Flow Split, and Reynolds number, respectively. With ν is kinematic viscosity and \dot{m} is mass flow-rate through the Light Phase Outlet. The last non-dimensional number is swirl number provided in 2.12.

3

Computational fluid dynamics

One of the significant closure models to resolve the turbulent flows is the Boussinesq closure hypothesis, which is mainly known as K-theory. Boussinesq closure hypothesis models assume a relation between the Reynolds stress and the local average strain rate tensor. The K-theory can lead to erroneous results, in cases that the skewness of the flow causes the velocity gradient and the shear stress have different directions[12]. Moreover, the experimental results from kitoh[5],Dirkzwagner[8], and steenbergen[7]reveal that the K-theory fails in swirling pipe flows. However, from two-equation turbulence models, the realizable $k - \epsilon$ model was utilized, and the numerical results proved that the realizable $k - \epsilon$ model predicts the flow field of low intensify swirling flow ($S_w < 0.5$) adequately.

Nevertheless, the complete second-order closure model was required to study the strongly anisotropic turbulence cases ($S_w > 0.5$). One of the advantages of the second-order closure model is that the production of Reynolds stress by gradients are in the average velocity field, and the Reynolds stress is described precisely by the second-order closure. Thus, the Quadratic Reynolds Stress Model is deployed for all the numerical cases in the present research.

It was found that predicting the flow field by the realizable $k - \epsilon$ model before switching to the Reynolds stress model supports the stability of the Reynolds stress model, as they are prone to divergence. As a result, all cases were initialized by the realizable $k - \epsilon$, and after one second of the flow time, the simulation methods were switched to the quadratic Reynolds stress model.

3.1. Turbulence modeling

This section provides an overview of the governing equations and explains the quadratic Reynolds stress model. The details derivations are omitted, and reader is referred to text of the Turbulent flows [12] and [13].This section, 3.1, uses the summation convention to illustrate the formulations.

Reynolds stress transport equation

The incompressible Reynolds stress equation is derived by multiplying the transport equations for velocity fluctuation u'_i with u'_j and adding the results to the transport equations for velocity fluctuation u'_j multiplied with u'_i .

$$\frac{D\overline{u'_i u'_j}}{Dt} \equiv \frac{\partial \overline{u'_i u'_j}}{\partial t} + \overline{u_k} \frac{\partial \overline{u'_i u'_j}}{\partial x_k} = P_{ij} + T_{ij} + \Pi_{ij} - \epsilon_{ij} \quad (3.1)$$

where:

P_{ij} : the production term (3.2) describes the production of Reynolds stress by gradients in the average velocity field. The Reynolds stress is exactly described by gradients in the average velocity field.

$$P_{ij} = -\overline{u'_i u'_k} \frac{\partial \overline{u'_j}}{\partial x_k} - \overline{u'_j u'_k} \frac{\partial \overline{u'_i}}{\partial x_k} \quad (3.2)$$

ϵ_{ij} : viscose dissipation (3.3) describes the dissipation of Reynolds stress by viscosity, and it is an isotropic tensor.

$$\epsilon_{ij} = 2\nu \overline{\frac{\partial u'_i}{\partial x_k} \frac{\partial u'_j}{\partial x_k}} \quad (3.3)$$

T_{ij} : transport term (3.4) fulfills the function of the spatial distribution of the Reynolds stress, and as a result of strongly anisotropic turbulence, this term is no longer negligible. Transport term is consist of three tensors, namely: transport by pressure fluctuations, transport by velocity fluctuations, and transport by viscosity effects. There are several closure hypotheses for transport term, and almost all of them are based on the gradient hypothesis. These closure models are not discussed here.

$$T_{ij} = -\frac{\partial}{\partial x_k} \left[\frac{1}{\rho} \overline{p' u'_j} \delta_{ik} + \frac{1}{\rho} \overline{p' u'_i} \delta_{jk} + \overline{u'_i u'_j u'_k} - \nu \frac{\partial \overline{u'_i u'_j}}{\partial x_k} \right] \quad (3.4)$$

Π_{ij} : pressure-velocity correlation (3.5) can formally be derived as an expression, but for this, an equation for pressure fluctuations (p') is required.

$$\Pi_{ij} = \frac{1}{\rho} \overline{p' \left[\frac{\partial u'_i}{\partial x_j} + \frac{\partial u'_j}{\partial x_i} \right]} \quad (3.5)$$

The p' equation is derived by taking the divergence of a transport equation for the velocity fluctuations and using the fact that the velocity field is incompressible results in the so-called Poisson equation. The equation 3.6 presents the exact expression of the pressure fluctuations.

$$\frac{1}{\rho} \nabla^2 p' = -2 \frac{\partial \overline{u'_i}}{\partial x_j} \frac{\partial u'_j}{\partial x_i} - \frac{\partial^2}{\partial x_i \partial x_j} (\overline{u'_i u'_j} - \overline{u'_i} \overline{u'_j}) \quad (3.6)$$

The closure hypothesis often simplifies the first term of the pressure fluctuations equation. The second argument of the equation 3.6 restores isotropy, and better known as Rotta's hypothesis. An optional pressure-strain model proposed by Speziale, Sarkar, and Gatski [14] replaces Rotta's hypothesis for numerical studies in this research.

Quadratic pressure-strain model

The model Speziale, Sarkar, and Gatski [14], which defines the second term of the equation 3.6 is written as follows:

$$\begin{aligned} \phi_{ij} = & -(C_1 \rho \epsilon + C_1^* P) b_{ij} + C_2 \rho \epsilon (b_{ik} b_{kj} - \frac{1}{3} b_{mn} b_{mn} \delta_{ij}) + (C_3 - C_3^* \sqrt{b_{ij} b_{ij}}) \rho K S_{ij} + \\ & C_4 \rho K (b_{ik} S_{jk} + b_{jk} S_{ik} - \frac{2}{3} b_{mn} S_{mn} \delta_{ij}) + C_5 \rho K (b_{ik} \Omega_{jk} + b_{jk} \Omega_{ik}) \end{aligned} \quad (3.7)$$

Where b_{ij} is the Reynolds-stress anisotropy tensor defined as

$$b_{ij} = - \left[\frac{-\rho \overline{u'_i u'_j} + \frac{2}{3} \rho k \delta_{ij}}{2 \rho K} \right] \quad (3.8)$$

The mean strain rate, S_{ij} , is defined as

$$S_{ij} = \frac{1}{2} \left(\frac{\partial u_j}{\partial x_i} + \frac{\partial u_i}{\partial x_j} \right) \quad (3.9)$$

The mean rate-of-rotation tensor, Ω_{ij} , is given by

$$\Omega_{ij} = \frac{1}{2} \left(\frac{\partial u_i}{\partial x_j} - \frac{\partial u_j}{\partial x_i} \right) \quad (3.10)$$

Table 3.1 presents the constants given in equation 3.7.

Table 3.1: Quadratic Reynolds stress model coefficients

C_1	C_1^*	C_2	C_3	C_3^*	C_4	C_5
3.4	1.8	4.2	0.8	1.3	1.25	0.4

3.2. Wall function

Accurate numerical resolution of the turbulent flow near to the wall requires a finer mesh because of steeper gradient close to the wall, and the current computational mesh of this research is designed to be harnessed for future researches with more complexity in the system. Moreover, section 3.3 explains the adequate solution of numerical simulation of the swirl flow at the center of the pipe requires ultimately a magnificently fine mesh with an excellent resolution. Hence, wall function is utilized to ensure the number of cells in the computational domain remains under the limit of the available computation power.

The wall function is a semi-experimental function that bridges the wall to the fully-turbulent region over the viscosity affected region, and this function employs the log law.

$$u^+ = \frac{1}{\kappa} (\ln(y^+) + \Pi) \quad y^+ > 30 \quad (3.11)$$

where κ is the Von Karman constant with a value $\kappa \cong 0.41$ and $\Pi = 2$. The two dimensionless variables u^+ and y^+ , which are known as the wall units, are defined as the following

$$u^+ = \frac{\bar{u}}{u_*} \quad \text{and} \quad y^+ = y \frac{u_*}{\nu} \quad (3.12)$$

Furthermore, the wall friction velocity u_* is defined as

$$u_* = \sqrt{\frac{\tau_w}{\rho}} \quad (3.13)$$

While the wall shear stress is denoted by τ_w , and y in equation 3.12 is the normal distance to the wall.

The shortcoming lies in the numerical results that the mesh grid in wall-normal direction is either significantly refined or extremely enlarged because the wall region is only valid for a specific range of the values of y^+ . So, the first grid node placement near the wall is very critical. The first node is referred to as the wall adjacent, and its height should ideally reside inside the log-law region. Also, the logarithmic layer intersects the viscous sublayer at $y^+ = 11$, which is accepted as the closest distance of the adjacent wall node in many mesh designs.

Nonetheless, during the pre-processing stage, the first cell height was estimated precisely with an iterative process from 3.11 equation to achieve the desired range of $30 < y^+ < 95$. The post-processing confirmed that the y^+ value remained within the targeted range, along the pipe wall for all simulation times and cases. Section 3.6 confirms the numerical simulations predicted the near-wall behavior accurately, as it was reported previously by Murphy [15] and Slot[2]. Additionally, Kitoh [5] measurements agree with the log-law for $y^+ < 100$. Thereby the wall function applications are validated for strongly swirling pipe flows.

3.3. Computational mesh

Ansys 19.1 was exploited to design the computational mesh. The numerical simulation domain was split into the eighteen connected zones, and each zone was divided into hexahedral elements, resulting in the creation of a mesh without hanging nodes between zones and a complete matching mesh parts. As was discussed in section 3.1, the mesh confronts a system of 10 extra coupled, nonlinear differential equations; thus, complying with the mesh quality standards (the minimum and maximum angles of the hexahedral elements, the variation of the volumes, the growth rates, orthogonality, skewness, and aspect ratio) was vital. Moreover, the pre-processing revealed that capturing the subtle changes in axial velocity at the center of the separator tube requires an extreme fine mesh at the center of the pipe, and section 3.6 discusses this matter in detail.

Figure 3.1 illustrates the cross-section of the mesh at $z = 1\text{ m}$, and the radial and azimuthal distribution of the mesh elements. It turned out the azimuthal spacing plays a crucial role in mesh convergence for high intensify swirl flows ($S_w > 1.6$).

The radial distribution of the mesh elements can be divided into four different radial sections. The central section constructs the smallest part of the mesh structure and resolves subtle variation in axial velocity. The inner middle section accounts for the wall of the collector and provides high-resolution mesh at the leading edge of the pick-tube, where the flow experiences a high-velocity gradient. Also, this section provides a smooth transition from the inner section to the outer-middle part of the mesh. The outer-middle part contains the coarser elements in the cross-section of the mesh structure without hindering the numerical

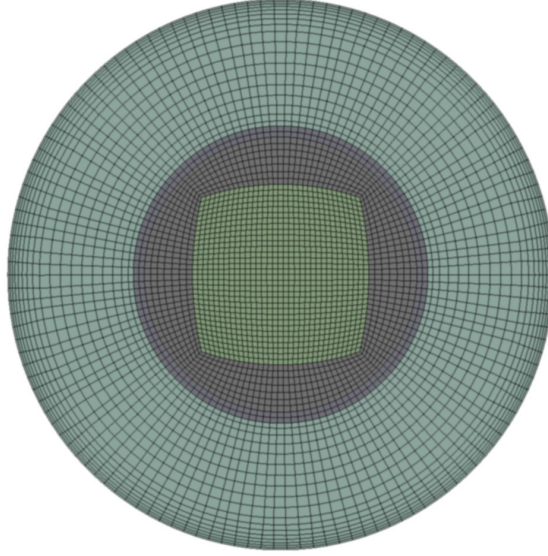


Figure 3.1: Computational mesh on cross-sectional plane in separator's tube, $z = 1 \text{ m}$.

solutions. Ultimately, the near-wall region ensures proper employment of wall function as it was described in section 3.2. The computational convergence in the axial direction is less dependent on the mesh distribution in the axial direction; however, the mesh distribution in axial direction is designed in such a way that ensures the maximum value of aspect ratio does not exceed 7.2. Special care was taken to ensure that the mesh element growth-rate remains constant and not exceeding more than 1.28 in any direction. The minimum and maximum angle between hexahedral elements were kept within 60° to 125° , and 99.1% of the elements have orthogonal more than 0.95, while 97.5% of them have skewness of less than 0.25.

A similar domain to Van Campen's test setup[1] validated the mesh performance. A series of simulations were set exactly with velocity profiles and outlet boundary conditions that were reported by him, while the computational domain structure respected his setup. The results confirmed that the mesh is robust, and the numerical simulations were stable for the highest swirl number. The final computational mesh consists of 3.2 million hexahedral cells, and table 3.2 summarizes the statistical properties of this mesh.

Table 3.2: Computational mesh statistics

Mesh quality parameter	Minimum	Average	Maximum	Excellent quality criterion
Orthogonal	0.86	0.993	1	0.7 - 1
Skewness	$1.2e^{-4}$	$5.2e^{-2}$	0.34	0 - 0.5
Aspect Ratio	1.01	2.12	7.13	1-18
Element Quality	0.26	0.80	0.999	0.5 - 1

3.4. Flow straightener

Flow straightener reduces the magnitude of the tangential velocity further downstream of the pipe. An additional advantage of the flow straightener is the recovery of static pressure by a tangential velocity loss. Van Campen[1] placed a 0.03 m PVC flow-straightener downstream of the Heavy-Phase Outlet (HPO) with an estimated porosity (ϕ) of 0.27. Accurate modeling of the flow straightener requires honeycomb structure models but at the expense of massive numerical cost. Considering that the flow behavior through the flow straightener is not a primary objective of this study, and the downstream of the flow straightener is located outside of the zone of interest, a porous medium modeled the flow straightener. The momentum loss in a simple homogeneous porous media is calculated by

$$S_i = - \left[\frac{\mu}{\alpha} v_i + K \frac{1}{2} \rho |v| v_i \right] \quad (3.14)$$

Where the α and K are the permeability and the inertial resistance tensors, respectively.

Very low viscous resistance value vanishes the Darcy term from 3.14 equation, but an accurate estimate of the inertial resistance tensor is impossible since the pressure drop across the flow straightener used in the experiment is unknown. Hence, several simulations were set to estimate the value of the elements of the K tensor. In reality, the flow straightener suppresses the swirl flow. Therefore, the axial component estimated one order of magnitude lower than radial and tangential components. The loss tensor K is approximated by the tensor

$$K = \begin{bmatrix} 200 & 0 & 0 \\ 0 & 200 & 0 \\ 0 & 0 & 20 \end{bmatrix} [m^{-1}] \quad (3.15)$$

The flow straightener is embedded into the structure of the numerical domain. The meshing strategy remains the same as explained in section 3.3 for flow straightener. The main objective of the flow straightener is eliminating the radial and azimuthal velocity components. So, slight adjustments may be applied to ensure those components are negligible downstream of the flow straightener.

3.5. Boundary Conditions

Section 3.5.1 covers an overview of experimental researches on swirling pipe flows to construct an initial velocity field that is required for the numerical cases. It appears that the most precise approach to restoring the velocity field at the aft of the static swirl tail is to generate a complete design of the static element and mesh it afterward. Slot [2] went through a cumbersome process of meshing only one swirl element and inhabited a complete design in his research. Here, we try to restore the possible velocity profiles at the aft of static swirl tail by approximating velocity profiles based on experimental data. The challenge remains that the aft of the swirl element is out of the zone of interest in experimental studies, so no one has measured the velocity field at the vicinity of the static element. Section 3.5.2 covers the outlet boundary conditions of numerical analysis.

3.5.1. Initial velocity distributions

The experimental results (Kitoh [5], Steenbergen [7], Drikzwagner [8], and Van Camp [1]) suggest the azimuthal component of velocity resembles a distribution similar to a Rankine vortex at the inlet, with a solid body rotation in the center and potential flow vortex at the larger radius. Additionally, the axial velocity profile at the inlet encounters its minimum value at the radius of the core of Rankine vortex, while, its maximum value, occurs at $\frac{7}{10}$ of the pipe radius (r). More details is illustrated in Appendix A

Also, the reviewed experimental data reveals that it is possible to approximate both profiles (axial and tangential) with a linear function. This approximation was tested by setting a simulation based on the Van Camp's [1] result from the strong swirl, and regenerating the velocity profiles that match his experimental results further downstream of the pipe.

Drikzwagner [8] provides the nearest measurements in the vicinity of the swirl element. Based on his measurements, the radius of the core of Rankine vortex is placed at $\frac{1}{5}$ of the pipe radius (R). Additionally, we know that the minimum axial velocity possible at the swirl element is zero. So the distribution of the axial velocity at the cross-sectional plane at the aft of the swirl element is given by

$$U_{zp} = \begin{cases} 0 & \text{for } 0 \leq r \leq 0.2R \\ 2\frac{r}{R}U_{zmax} - 0.4U_{zmax} & \text{for } 0.2R < r \leq 0.7R \\ U_{zmax} & \text{for } 0.7R < r < R \end{cases} \quad (3.16)$$

While U_{zp} is the axial velocity profile function and U_{zmax} is its maximum value. The axial velocity goes to zero at the wall. We considered a linear profile from U_{zmax} to zero from the radial distance of 0.0993R to R.

The bulk velocity at this cross-section is given by

$$U_b = \frac{1}{\pi R^2} \int_0^R 2\pi U_{zp} r dr \quad (3.17)$$

The axial velocity goes to zero at the wall. We considered a linear profile from U_{zmax} to zero from the radial distance of 0.0993R to R.

Calculating the bulk velocity by placing U_{zp} (function 3.16) in equation 3.17, and performing the integration, yields

$$U_{zmax} = 1.3U_b \quad (3.18)$$

Now, the axial velocity profile at the aft of the tail of the static swirl element is given by

$$U_{zp} = \begin{cases} 0 & \text{for } 0 \leq r \leq 0.2R \\ 2.6 \frac{r}{R} U_b - 0.52 U_b & \text{for } 0.2R < r \leq 0.7R \\ 1.3 U_b & \text{for } 0.7R < r < R \end{cases} \quad (3.19)$$

We considered a linear profile from $1.3U_b$ to zero between the radial distance of $0.0993R$ to R .

Rankine vortex formulation provides the linear function of the azimuthal velocity profile, the Rankine vortex core radius, R_c is updated to $R_c = 0.2R$ based on observation made from the measurements of Drikzwagner[8].

$$U_{\theta p} = \begin{cases} U_{\theta_{max}} & \text{for } R_c < r < R \\ \frac{r}{R_c} U_{\theta_{max}} & \text{for } 0 \leq r \leq R_c \end{cases} \quad (3.20)$$

An assumption is made that the tail of the static swirl element is short and smooth enough that there is no momentum lost between the edge of the vane geometry to the aft of the swirl element. Figure 3.2 illustrates the static swirl element and its key features. So, the axial flux of the azimuthal momentum in two cross-sections is equal.

$$\int_{R_{gap}}^R 2\pi\rho U_{zt} U_{\theta t} r^2 dr = \int_0^R 2\pi\rho U_{zp} U_{\theta p} r^2 dr \quad (3.21)$$

Where $U_{zt}, U_{\theta t}$ are the axial and the tangential velocity at the edge of the wane, and U_{zp} and $U_{\theta p}$ are axial and tangential velocity at aft of element, respectively. ρ presents the density of the fluid, while R and R_{gap} are the tube radius and radius of the gap between the tube and the body of the static swirl element, respectively.

The swirl intensity of an element is defined by the swirl number at the cross-section at the edge of the wane, definition of the swirl number 2.12 gives

$$S_w = \frac{\int_{R_{gap}}^R 2\pi\rho U_{zt} U_{\theta t} r^2 dr}{\rho\pi R^3 U_b^2} \quad (3.22)$$

Now, the axial flux of the azimuthal momentum at the aft of the element for incompressible fluid can be written as

$$\int_0^R U_{zp} U_{\theta p} r^2 dr = \frac{1}{2} R^3 U_b^2 S_w \quad (3.23)$$

Placing the axial velocity profile (3.19) and Rankine Vortex (3.20), and performing the integration, yields

$$U_{\theta_{max}} = 2U_b S_w \quad (3.24)$$

Finally, the tangential velocity profile at the tail of the static swirl element is given by

$$U_{\theta p} = \begin{cases} 2U_b S_w & \text{for } R_c < r < R \\ 2 \frac{r}{R_c} U_b S_w & \text{for } 0 \leq r \leq R_c \end{cases} \quad (3.25)$$

Where S_w and U_b are the swirl number of the swirl element and the bulk velocity. The tangential velocity goes to zero at the wall. We considered a linear profile from $2U_b S_w$ to zero from the radial distance of $0.0993R$ to R .

The two velocity profiles 3.19 and 3.25 predict the velocity field at the aft of the swirl element. To ensure that the assumptions and simplifications reflect the reality, a test simulation was run with simplified profiles and the simulation results were compared with the experimental results from van Campen[1] and the numerical study of Slot[2]. Section 3.6 confirms that the simplifications are adequate.

These simplifications enable us to perform the numerical studies for variety of bulk velocities or swirl elements without going through the meshing of each individual swirl element.

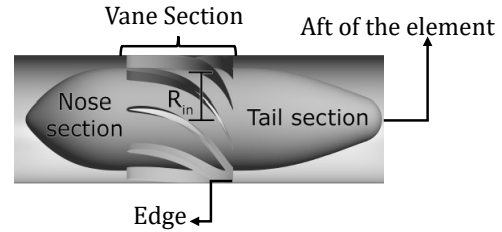


Figure 3.2: Internal swirl element with key features Slot [2]

3.5.2. Outlet boundary conditions

Two types of the outlet boundary condition(BC) were used, as they are shown in section 3.7.

Fundamental study of swirl flows

At Outlet, a standard pressure outlet boundary condition, referenced to atmospheric pressure, is set to zero at $r=0$.

Inline swirl separators

At Heavy Phase Outlet(HPO), a standard pressure outlet boundary condition, referenced to atmospheric pressure, is set to zero at the outer wall of the collector tube; and for Light Phase Outlet (LPO), a mass flow-rate outlet boundary condition is set. The flow split (FS) defines the mass flow-rate reference for each case, the details of the flow split definition are provided in section 2.4.1.

3.6. Comparison with the experiments and numerical models

This section covers the details of the last test-case, which was set to confirm the accuracy of the numerical system. The ultimate numerical system is prepared according to the instructions are given in sections 3.3, 3.4, and implementation of the simplified velocity profiles 3.19, 3.25 and tuning the solver with quadratic Reynolds stress model. The test case revealed that the prepared numerical system is valid, and the set up can be deployed for further studies in this research. The results of the test-case simulation were plotted against Slot simulation and Van Campen experiments [1]. Figure illustrates the key features and boundary conditions for the ultimate test case; its results are discussed in section 3.6.1 and 3.6.2

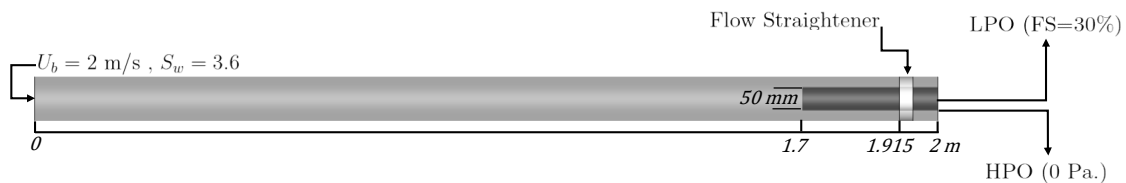


Figure 3.3: Test-case domain; the boundary conditions as per describe in section 3.19, 3.25,3.5.1 & 3.5.2, design as per Van Campen setup [1] - $R_b = 181,000$

3.6.1. Inside of the separator tube $0 < Z < 1.5 m$.

Figure 3.4, and figure 3.5 present the obtained axial and tangential velocities from the test-case and compares them with the results form Van Camp experiment and Slot simulation.

Central separator tube - $r < 30 mm$.

Figure 3.4 illustrates an accurate axial velocity prediction by the test-case in the center of the tube region. A subtle but significantly vital discovery is the prediction of the negative axial velocity at the central region as Van Camp reports it. The detection of the negative axial velocity is detrimental to the separation process efficiency. Slot numerical results (the grey dashed) fail to detect the negative velocity at the center of the pipe, and we show that mesh refinement in this region allows to capture this behavior.

Figure 3.5 reveals more accurate tangential velocity profile predictions, compared to the axial velocity field, and the test-case presents a visible prediction improvement of the tangential field behavior, compared to Slot simulation, at the center of the pipe.

Near-Wall region - $r > 30 mm$.

Figures 3.4 and 3.5 present an overlap between all three results (Test-case, Van Camp, and Slot) in the near-wall region ($r > 30 mm$), and that is because the velocity fields (Tangential and Axial) are both more stable in the near-wall region, and the wall function could bridge between the wall and main turbulent field. Whereas the pipe center, which is the prime zone of the interest for separation purpose, remains the most challenging part to be predicted.

3.6.2. Just upstream of the collector tube $1.6 < Z < 1.7 m$.

Figures 3.6 and 3.7 illustrate the behavior of the velocity fields further in the separation tube, less that one diameter of the pipe from the verge of the collector tube.

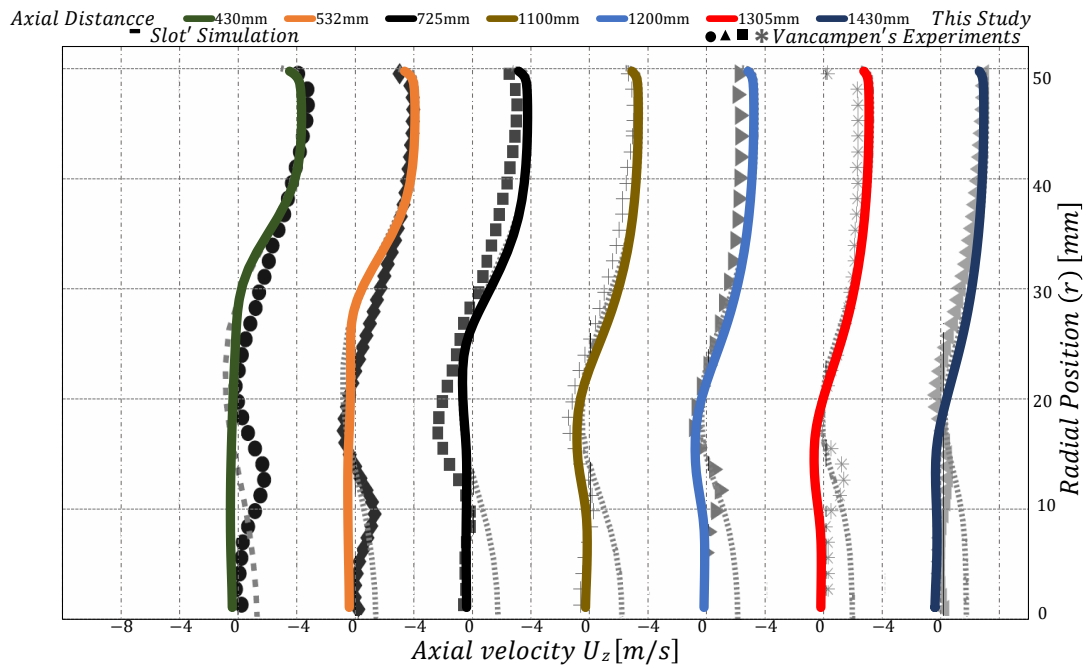


Figure 3.4: Comparison of the axial velocities at different axial distances. Grey symbols Van Campen [1], grey dashed Slot's results[2], and colored symbols are this research

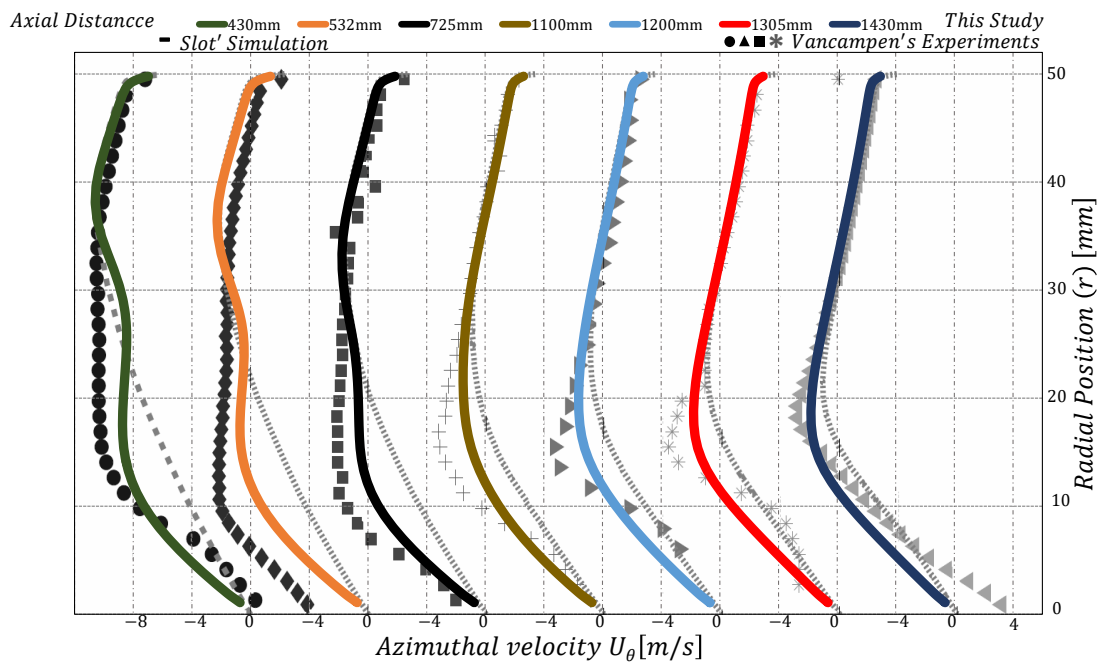


Figure 3.5: Comparison of the tangential velocities at different axial distances. Grey symbols Van Campen [1], grey dashed Slot's results[2], and colored symbols are this research

Central separator tube - $r < 30 \text{ mm}$.

Figure 3.6 reveals that the test-case does not predict the axial velocity field as accurately as the field measured by Van Campen, and as the flow progress towards to the entrance of the pick-up tube the discrepancies between the data increases. The main reason behind the discrepancy is related to the length of the domain, as figure 3.3 presents, the outlet of the domain in the test-case is only 0.27 m . further from the entrance of the pick-up tube. Therefore the boundary condition applied at the outlet influences the results of the velocity field in upstream (vicinity of the collector). Additionally, Slot [2] mentioned that he had to extend the collector length by 1.2 m . to predict the measured data from Van Campen. Moreover, Van Campen did not place the straightener in the collector (only in outer annular), which is embedded in the test-case domain. Also, it might be possible that Van Campen measured the reflected fluids at the bent of the collector, or vortex breakdown, but we cannot confirm this hypothesis.

However, the conclusion is that the behavior at the outlet much depends on the physical condition of the outlet, and mimicking the exact test setup is not the purpose of the test-case. In contradiction, tangential

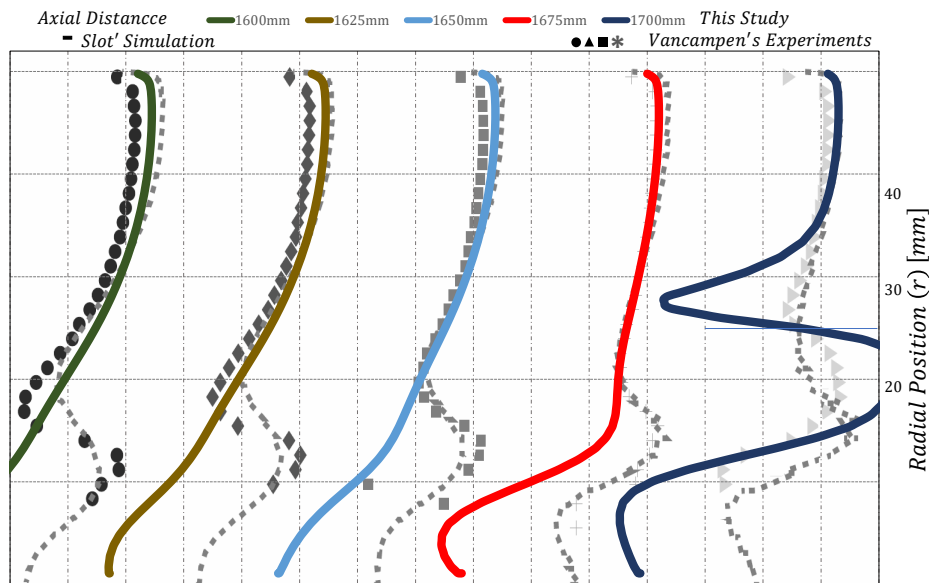


Figure 3.6: Comparison of the axial velocities at vicinity of the collector- $Z = 1.70 \text{ m}$. Grey symbols Van Campen [1] and grey dashed Slot's results [2], and colored symbols are this research

velocity is predicted very well, figure 3.7, and the improvement of the prediction to Slot simulations are still noticeable. That confirms the axial velocity field is more difficult to be predicted at the center of the pipe, and it is less affected by changes in the gradient of the pressure in axial and radial directions.

Near-Wall region - $r > 30 \text{ mm}$.

Figures 3.6 and 3.7 confirm the fact that the velocity fields are more stable in the near-wall region, and velocity field prediction in the region close to the wall is precise and accurate in the numerical analysis.

conclusions

Numerical study of the test-case simulated the velocity field accurately, and more precise in the region close to the wall ($r > 30 \text{ mm}$). The inlet velocity simplifications were adequate to predict the velocity field behavior, and the mesh resolution is high enough to capture the subtle behavior of the axial velocity field at the center of the pipe. Section 3.7 explains the implementation of findings mentioned earlier into the final cases.

3.7. Numerical simulations cases

The design of the first tomography-controlled inline swirl separator relies on a better understanding of the dynamic of confined vortices in the pipe; a series of studies were conducted to fulfill this matter. Section

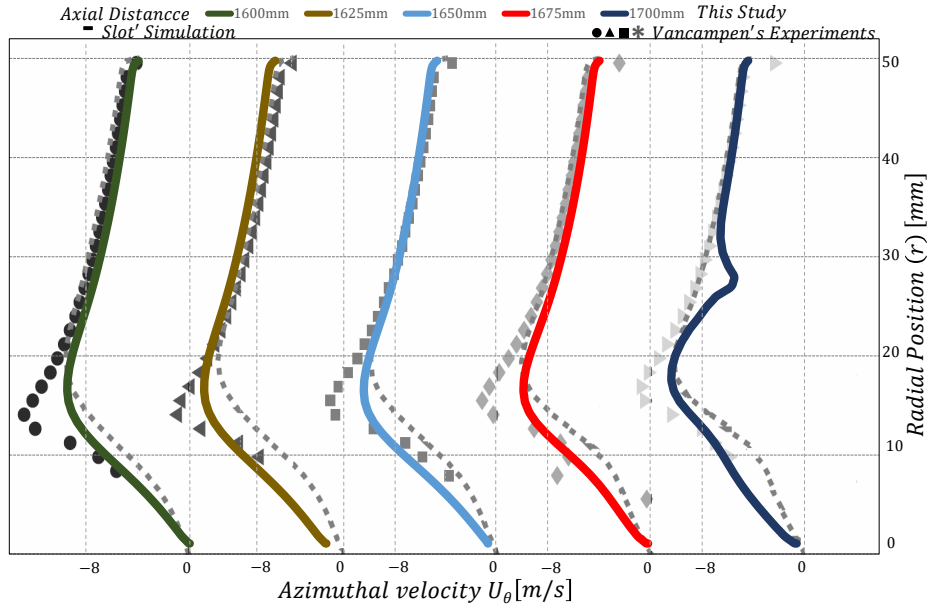


Figure 3.7: Comparison of the tangential velocities at vicinity of the collector- $Z= 1.70 \text{ m}$. Grey symbols Van Campen [1] and grey dashed Slot's results[2], and colored symbols are this research

3.7.1 provides an overview of fundamental study cases. Also, the ultimate goal is an effective separation of the lighter from denser fluid, so design consideration cases were executed to provide the pillar of the design strategies. Section 3.7.2 provides reviews of the design strategy case.

3.7.1. Fundamental study of swirl flows

The static swirl element generates tangential motion at the expense of the static pressure. The generated swirl motion acts as a centrifugal force on the pipe wall, causing the wall pressure to become higher than the pressure at the center of the tube. Swirl flow motions are known for the decay of the swirl intensity inside the pipe, the reverse flow zone, and the vortex breakdown. The flow swirl motion acts as a centrifugal force on the pipe wall, causing the wall pressure to become higher than the pressure at the center of the tube, roughly, the pressure gradient in the radial direction is determined by the fluid density, ρ , tangential velocity, U_θ ; $\frac{U_\theta^2}{r} \approx \frac{1}{\rho} \frac{\partial P}{\partial r}$. The radial pressure gradient decreases in the downstream direction because of the decay of the tangential velocity. Thus, the axial gradient of the wall pressure is negative. The fight between the two pressure fields continues until either the vortex is not stable and vortex breaks down, or the static pressure loss is recovered. The complexity of the swirl flows and their dynamics are studied through the research cases provided in table 3.3. This section provides an overview of the setup of the cases, and chapter 4 reviews the flow behavior of the cases presented in table 3.3 in detail. Table 3.3 reflects that the studies were focused on the swirl intensity, turbulence, and viscous forces effects.

Table 3.3: Fundamental study of swirl flows cases (swirl intensity vs. turbulent & viscous forces effects)

S_w	0.1	0.2	0.5	1.0	1.6	2.5	3.6
	150,000	150,000	150,000	-	150,000	150,000	150,000
Re_b	-	-	-	-	100,000	-	-
	-	-	-	-	8,000	-	-
	-	-	-	500	-	500	-
	-	-	-	100	-	100	-

Solver setting

In all studies, a bulk velocity (U_b) equal to 1.5m/s is imposed at the inlet. The inlet and outlet boundary conditions are as per prescriptions in sections 3.5.1 and 3.5.2. Additionally, the final domain design is changed based on the lesson learned from section 3.6. While the meshing and flow straightener design remains the same as it is explained earlier in this chapter. Moreover, the gravity vector is pointed into the negative z-direction; the fluid is flowing upward. Figure 3.8 presents the latest domain design and the boundary conditions applied for the fundamental studies.

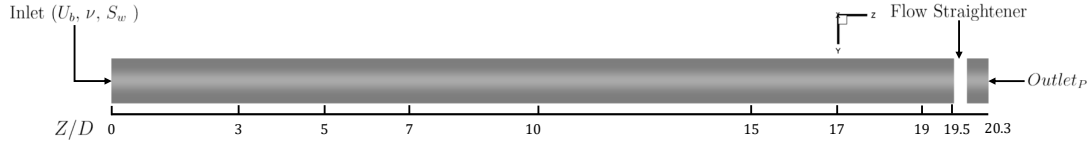


Figure 3.8: Boundary conditions used for simulations of fundamental study cases

The transient time-step, Δt , is set at 0.5ms, for the spatial time-averaged numerical analysis; and it is updated to 0.25ms, for analyzing the temporal behavior of the flow, as per time scales explanation in Section 2.4.4.

The Root Mean Square residual criteria were set at 5×10^{-6} for all convergence parameters. An operational state is defined after a minimum of 2 seconds of the flow-time. Then a recording of the data started for another one second of flow-time, which means 2000 time-steps for time-averaged spatial behavior, and 4000 time-steps for temporal behavior analysis.

3.7.2. Inline swirls separators

The proper design of an inline swirl separator relies on identifying the exact operational limits of the separator. The inline separator uses an essential principle to operate, centrifugal force. Liquid-liquid separators are known for their low separation efficiency due to the slim difference between their specific gravities. Therefore, some designs tried to overcome that challenge by empowering the separator with higher centrifugal force, but the strong vortex introduces new obstacles to the operation. The main objective is to design a smart inline swirl separator that is efficient within its operational limits. The purpose of the control system is to maintain the operational limits of the separator when the flow conditions are changed.

This research tries to find out where the limits are standing when it comes to changing the key features of the separator. The main key features are the static element, which provides the separation power, and pressure values that control the mass flow-rate through each outlet (Heavy Phase and Low phase). In this section we introduce the case setup and chapter 5 reviews the results in detail. Table 3.4 provides the cases that were studied throughout this research.

Table 3.4: Design of swirl separators cases (swirl intensity vs. flow split); $Re_b = 150,000$

S_w	0.1	0.2	0.5	1.6	2.5	3.6
15			✓	✓	✓	
25			✓	✓	✓	
F_s 50			✓	✓	✓	✓
75			✓	✓	✓	
85			✓	✓	✓	

Solver setting

In all studies, a bulk velocity (U_b) equal to 1.5m/s is imposed at the inlet. The inlet and outlet boundary conditions are as per prescriptions in sections 3.5.1 and 3.5.2. Additionally, the final domain design is changed based on the lesson learned from section 3.6, while the meshing and flow straightener design remains the same, as it is explained earlier in this chapter. Moreover, the gravity vector is pointed into the negative z-direction; the fluid is flowing upward. Thus, there have been no changes in the setting up the solver for inline separator design, to ensure the results can be compared with the data from the fundamental study for swirl pipe flows, except that the collector tube is placed in the domain. Placement of the collector inside the tube splits the outlet into two separate outlets, namely Heavy Phase Outlets (HPO) and Low Phase Outlet (LPO),

with boundary conditions explained earlier in this section. Additionally, we were only interested in the time-averaged spatial behavior of the flow, and water is used as the fluid. The collector is a tube with 0.53m length, 0.05m internal diameter, and 0.002m wall thickness. The solid wall boundary with a no-slip condition, the same as the outer tube, is applied to the wall of the collector as a boundary condition. Figure 3.9 illustrates the domain and boundary conditions that were applied in for design studies.

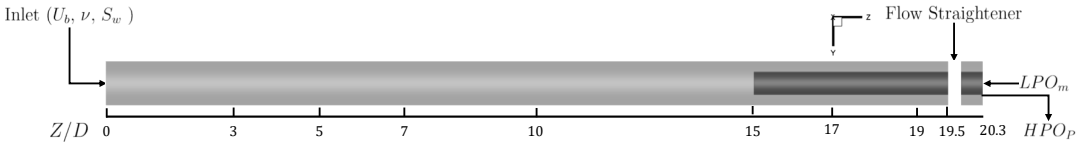


Figure 3.9: Boundary conditions used for simulations of design study cases

4

Fundamental study of swirl flows

This chapter focuses on the understanding of the dynamic behavior of swirl flows in a pipe. Quite different devices have been used to generate swirl flows and an equally wide variety of initial velocity distributions. The two types most often reviewed are referred to as "concentrated vortex" and "solid body" rotation. The concentrated vortex is found in Sven Grundman [16], Li Tornia [17], Steenbergen [7], Alekseenko [18], and Kitoh [5] works. In most of these cases, the fluid was set in rotation before entering the pipe in the radial direction. In such cases, swirl intensity decays rapidly, due to the action of the adverse pressure gradient, and sometimes, vortex instability encountered as vortex core breakdown.

In contrast, swirl flows generated at the inlet of a tube and constrained inside of the tube, are prone to absorb less attention by scholars. These type of experimental studies are found in Kitoh [5], Steenbergen [7], Dirkwegenr [8], Van Campen [1], Rocklage-Marliani [19], and Pashtapanska [20]. Even fewer numerical simulations on this type of flows are performed. Most of the numerical studies are focused on low Reynolds numbers, covering the laminar swirl flows that are generated by a rotating honeycomb in a controlled laboratory environment, H. A. Vaidya [21]. However, high Reynolds numbers and turbulent swirl flows are the most encountered in the industry. Slot [2] covers the numerical studies in a range from 150,000 to 200,000. Perhaps, the requirement of magnificent mesh refinement, the it requires a lot of simulation time and computational power. The static swirl elements generate a swirling field that resembles the Rankine vortex with a solid body rotation as Drikzwagner and Van Campen's report. In order to understand the physics underlying this type of swirl flows, the case studies presented in section 3.7.1 were performed.

This chapter discusses the flow properties based on what is characterized as low and high swirl intensity. In the classical definition of the swirl intensity, the swirl numbers higher than 0.5 are known as adverse swirl flows. In this research, we classified the $S_w = 0.5$ as a low swirl number for the sake of the presentation and illustrating the flow structure. This chapter focuses on the visualization of the flow structure and dynamics of the swirl flow.

4.1. Mean quantities analysis

This section deals with the time-averaged velocity profiles (axial, tangential, and radial), and illustrates the flow structure for increasing swirl intensity. The longitudinal contours on the planes $\frac{x}{D} = 0$, through the axis of the pipe, and the cross-section contours at $\frac{z}{D} = 3, 5, 10, 17, \& 19$ are provided, to analyze the velocity fields. The flow straightener is indicated by white color, as the turbulent results inside this region is not a prime objective of the research, even though the solver was set to solve the turbulent equations in this region.

4.1.1. Axial velocity profiles

Figures 4.1 and 4.2 present the dimensionless time-averaged axial velocity contours and profiles for six different swirl intensity with Reynolds number of 150,000.

$S_w < 0.5$

The case of the swirl motions $S_w = 0.1$ & 0.2 . Increasing the swirl number creates a negative axial velocity at the entire of the pipe. The development of the reverse flow happens at a critical swirl number; beyond this swirl number, the axial velocity at the core of the vortex remains negative, $S_w = 0.5$. The reverse flow zone

shows a minor development in the entire of the tube, and its diameter remains constant throughout the tube. The maximum axial velocity is located close to the wall, at $r/D=0.35$; and it decreases and moves toward the center for increasing in Z direction, figure 4.1.

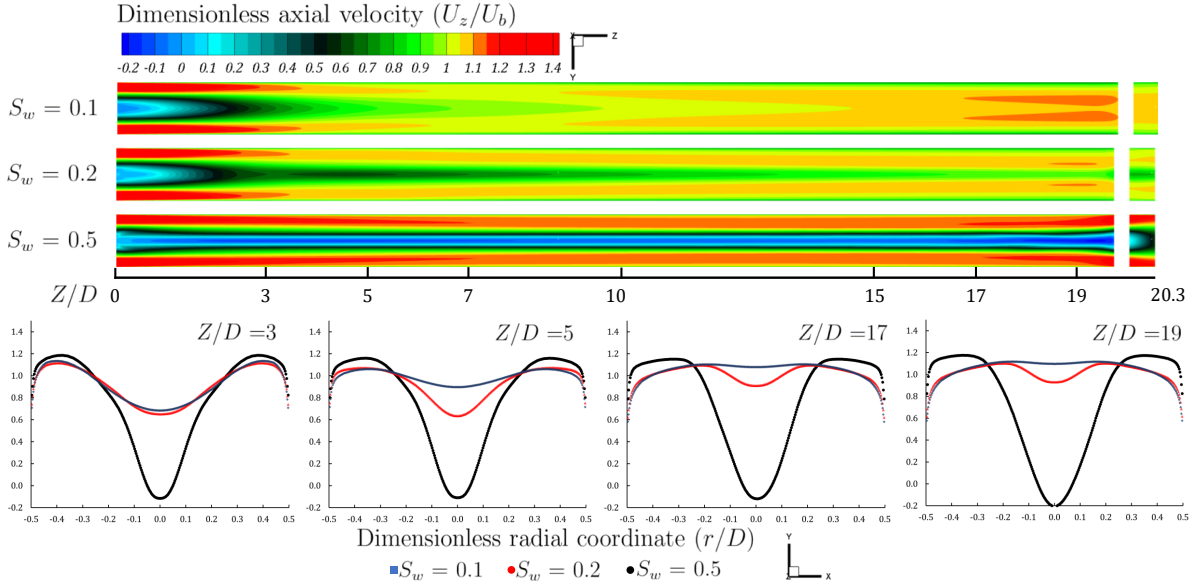


Figure 4.1: Dimensionless time-averaged axial velocity contours and profiles for various S_w on the plane $\frac{X}{D} = 0$ and $\frac{Z}{D} = 3, 5, 17 \& 19$

$S_w > 0.5$

The axial velocity profile for strong swirl elements shows a more complex pattern, when compared to low swirl flows. The velocity profile develops a broad reverse flow region: the maximum axial velocity appears at $r/D = 0.4$, and the region of maximum axial velocity becomes more flat and reduces in the streamwise direction. This configuration resembles a positive annular flow with a negative core center. At the macro scale level, the flow forms two positive and negative regions. The maximum diameter of the reverse region located around $Z/D=4$, and it reduces when moving in the streamwise direction, figure 4.2. A stronger swirl element creates a more larger negative axial velocity diameter at $Z/D = 5$. The negative region shrinks while its intensity (absolute value of axial velocity) increases. This behavior is coupled with the displacement of the maximum value of the tangential velocity to the center in the streamwise direction. Section 4.1.2 explains this behavior. At the same time, the maximum negative velocity remains at axis of the pipe. To explain this behavior, let us assume that the viscosity and Reynolds stresses can be neglected. Therefore the flow is an ideal flow and with no fluctuations.

At the pipe axis, $\overline{\omega_r}$ and $\overline{\omega_\theta}$ are zero. Thus, the mean vorticity vector contains the mean axial vorticity component only. The material derivative of mean vorticity vector couples the behavior of axial velocity with $\overline{\omega_z}$, at the centerline.

$$\frac{D\overline{\omega_z}}{Dt} = \overline{\omega_z} \frac{\partial U_z}{\partial z} \quad (4.1)$$

Let us neglect the fluctuation, as it is presented in figure 4.2 the $\frac{\partial U_\theta}{\partial r} = \overline{\omega_z}$ increases in the streamline direction. So, on the centerline, the maximum reverse velocity coincides with the cross-section that the maximum of the $\frac{\partial U_\theta}{\partial r}$ occurs.

Axial velocity morphology

Figures 4.1 and 4.2 present longitudinal-section contours at $X=0$, which reveal that by increasing the swirl number, the flow dynamics moves inside of the reverse flow region. $S_w=1.6$ presents the beginning of a bubble shape formation, and an entire bull eye region is visible at the center of the reverse zone on $S_w=2.5$. The bull eye shape is referred to as the light blue color inside the negative axial velocity core on $S_w = 2.5$. This bull eye resembles the development of instability inside the vortex core. Section 4.2.1 reviews this feature by

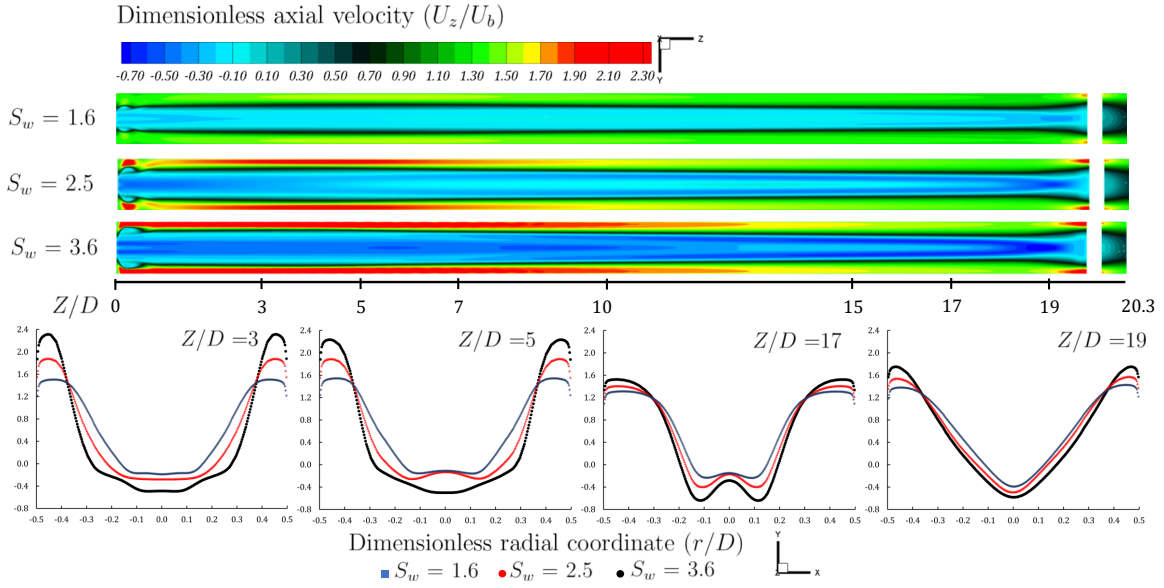


Figure 4.2: Dimensionless time-averaged axial velocity contours and profiles for various high S_w on the plane $\frac{X}{D} = 0$ and $\frac{Z}{D} = 3, 5, 17, 19$

considering relative helicity. Also, figures 4.1 and 4.2 show the profiles distance cross-sections. The shape of the profile changes from a wide U to W and returns to V in various axial positions, for high swirl numbers. The change of the profile indicates the development of instability dynamics in the core center and reformation of a new reverse flow with different velocity speeds. Section 4.2.3 reviews these instabilities in the form of the vortex breakdown. For now, we consider the sharp V shape generated with $S_w=0.5$ as a sign of stable vortex. The change of the axial velocity profile suggests that the instability at the center of the vortex is higher for a stronger swirl.

4.1.2. Tangential velocity profiles

Figures 4.3 and 4.4 present the dimensionless time-averaged tangential velocity contours for various swirl numbers.

$S_w < 0.5$

The tangential velocity presents two regions of flow behavior, same as axial velocity. For a low intensified swirl flow, it appears the profile is much flatter in the outer part of the central region $S_w=0.1$. The maximum tangential velocity behaves non-monotonic behavior with increasing the swirl number. As a result, $\frac{\partial U_\theta}{\partial r}$ exists with different behaviors with increasing the swirl number. Surprisingly, the swirl motion does not die in the entire length of the tube ($Z=2m$) even for such a low swirl intensity as the one equal to 0.1, figure 4.3.

Also, the solid-body rotation shape is (the central region) formed at $S_w=0.1$, and that confirms the initial velocity distribution (the device that generates the swirl motion) influences the shape of the swirl, but as we will see later on, it does not dictate its destiny.

$S_w > 0.5$

Figures 4.4 presents the tangential velocity profiles for adverse swirl intensity flows. The solid-body rotation stretches itself to $r/D = 0.4$ and forms a firm solid-body rotation swirl flow at $Z/D = 3$. The solid-body rotation is evident for the high swirl numbers in the first half of the pipe length. The other profile specifications remain the same as low swirl numbers, and only minor changes in the shape of tangential velocity profiles are visible, figures 4.3 and 4.4. The tangential velocity behavior is similar for all different swirl numbers.

Tangential velocity morphology

As it was described, the solid-body rotation is evident in the central region in all swirl flows despite their swirl number. At a low swirl intensity, $S_w = 0.1$, swirl stretches itself to the wall, so it shows free swirl flow morphology. As the swirl number increases, the swirl flow changes its profile to a "Concentrated Vortex," and

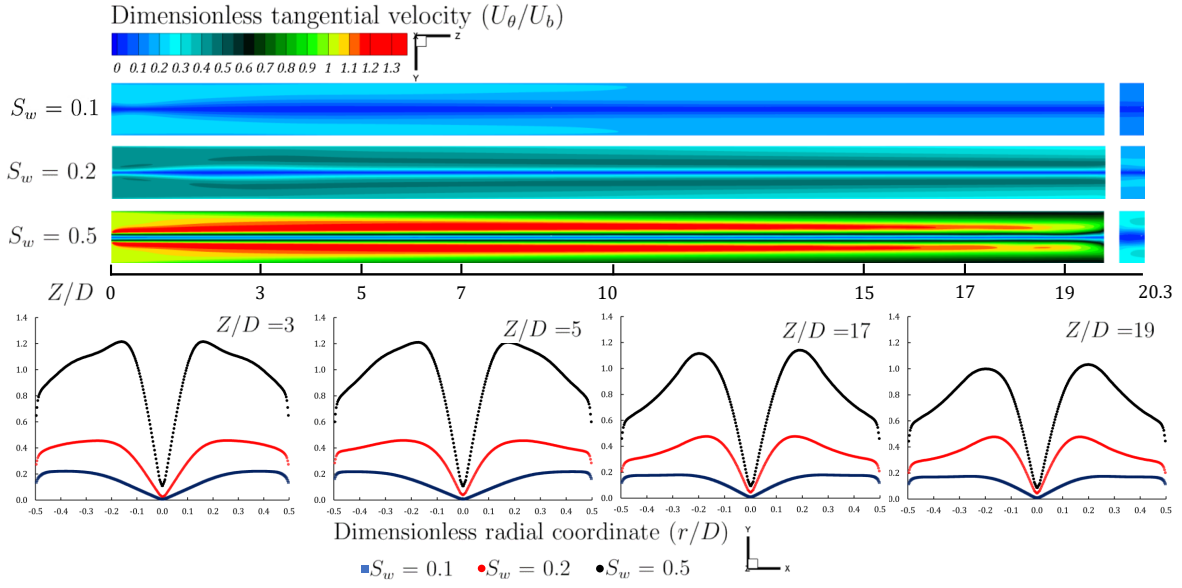


Figure 4.3: Dimensionless time-averaged tangential velocity contours and profiles for various S_w on the plane $\frac{X}{D} = 0$ and $\frac{Z}{D} = 3, 5, 17, 19$

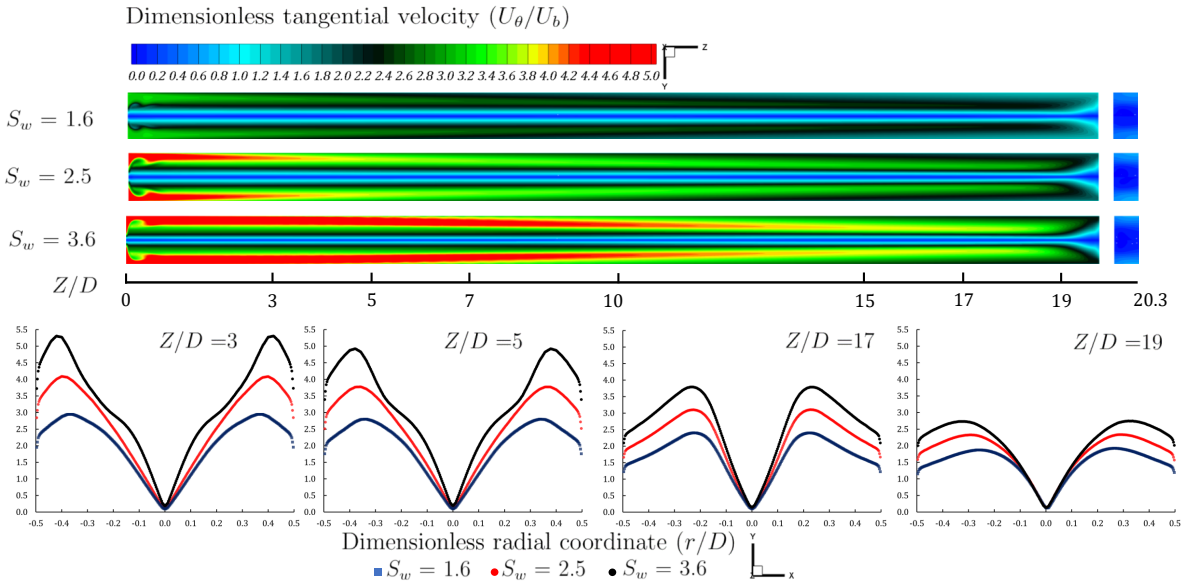


Figure 4.4: Dimensionless time-averaged tangential velocity contours and profiles for various S_w on the plane $\frac{X}{D} = 0$ and $\frac{Z}{D} = 3, 5, 17, 19$

development continues till $S_w = 0.5$. Figure 4.5 is a reference to the "Concentrated Vortex," and the tangential velocity profile of $S_w = 0.5$ at $Z/D = 3$ resembles this figure.

It appears that the stronger swirl numbers go through two types of swirl profiles. Near the inlet, $Z/D=3$, they exhibit "Solid-Body," and they change to the "Concentrated Vortex" profile, while moving along the streamwise direction.

The solid-body profile is more evident in the strongest swirl number, $S_w = 3.6$, and it reflects the solid-body profile for the first half of the length of the pipe, change happens because the tangential velocity decays, and its maximum moves toward the center, when moving in the streamwise direction. However, the displacement to the center happens at a faster pace than the decay of the tangential velocity magnitude. Figure 4.4 reveals that the tangential velocity decays faster for higher swirl elements; it shows that the decay coefficient

is not constant for different swirl numbers, even in one apparatus.

4.1.3. Radial velocity profiles

The time-averaged radial velocity, regardless of the intensity of the swirl, is in the order of 10^3 smaller when compared to its concomitants components. Perhaps, one can omit the radial component in the Reynolds averaging equations, and turbulent field ($U_r \cong 0 \rightarrow \overline{U_r} = 0$ & $U_r' = 0$). However, this section shows that the smallest component of the velocity vector has a different flow morphology. The disk or ring profile in the cross-sectional planes suggests that radial velocity profiles needs more investigations to reveal its profile for the highest swirl number. Figures B.2, B.1 present the dimensionless time-averaged profile of the radial velocity for all the swirl numbers, and B.3 shows the transverse-section of all velocities for all swirl numbers at $Z/D = 10$. The Next section introduces another method of visualization of the flow, and tries to explain the structure of the flow more concisely.

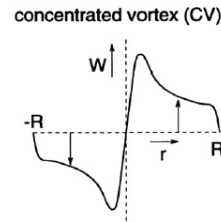


Figure 4.5: Tangential velocity profiles Steenberg [7]

4.2. Swirl flow dynamic and structure

4.2.1. Relative helicity

The sign and magnitude of the relative helicity are combined with the direction of the axial velocity to complete the flow morphology of the swirl flows. The colored streamlines illustrate the different structures of the flow. The sign of helicity identifies the primary and secondary vortices in the graphical representation. The magnitude of the helicity locates the vortex core axis, while the flow-streamline describes the nature of the flow.

Figures 4.6 and 4.7 show the time-averaged helicity contours in cross-sectional and longitudinal planes. The magnitude of relative helicity indicates the local curvature of the streamlines. In this research, it is acceptable to assume that the streamlines are locally straight when the velocity and vorticity vectors are parallel. Thus, the absolute maximum of the magnitude of the relative helicity locates the core axis of the vortex. Figure 4.7 reveals that the core of the vortex of the time-averaged flow locates itself at the center of the tube irrespective of the swirl number.

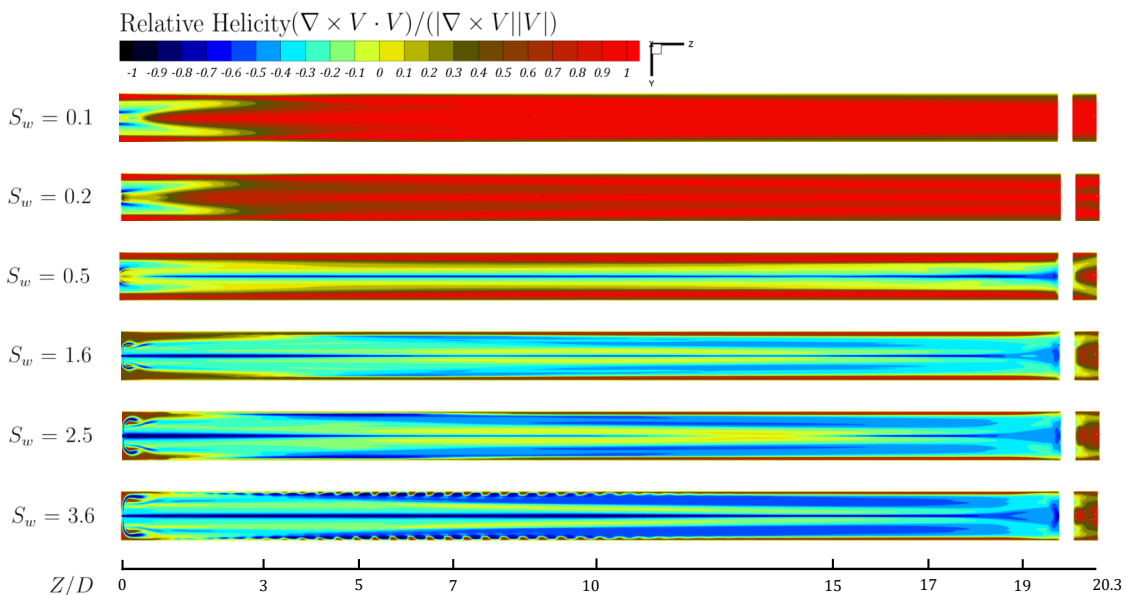


Figure 4.6: Dimensionless time-averaged helicity contours for various S_w on the axial cross-section plane- $X=0$

$S_w < 0.5$

The maximum relative helicity happens at unity for the low swirl intensities ($S_w = 0.1$ and $S_w = 0.2$); the intense red color in figure 4.6 indicates that these types of swirl flow, the velocity, and vorticity vectors are parallel throughout the pipe. The alignment of the velocity and vorticity stretches the flow-streamlines from a helix to straight lines; figure 4.8 illustrates the flow-streamlines stretched from a helix to straight-line at $Z/D = 19$. The vortex constructs a single vorticity structure. Figure 4.6 and 4.7 shows the relative helicity reaches roughly to the maximum possible value of 1 at $Z/D = 10$ for $S_w = 0.1$ the entire pipe diameter. This figure imitates a free vortex flow structure. Indeed, the central part of the flow tends to rotate as a solid-body.

Doubling the swirl intensity, $S_w = 0.2$, the vortex core is visible the entire length of the pipe. The area of the vortex core remains roughly the same in the streamwise direction. However, from $Z/D = 15$, $S_w = 0.2$ tends to present the same morphology as $S_w = 0.1$ due to decay of the swirl. The streamlines, figure 4.8, exhibit more helical nature which is common to this type of flow, and the axis of vortex remains on the axial axis of the pipe. The maximum relative helicity is located at the vortex axis, and it is equal to -1 (maximum absolute number) for Swirl number 0.5; indicated by dark blue in figure 4.8, 4.6, and 4.7. Consider the local vorticity vector relative to a local streamline. One component is parallel to the local velocity vector, and the other two are perpendicular to it. When the helicity changes sign, the parallel component of the local vorticity vector is in the opposite direction as the local velocity vector. Figure 4.7 illustrates at the wall-region, the parallel component of the vorticity vector is in the same direction as the local velocity vector, while further from the wall-region, the same component is in the opposite direction of the local velocity vector. We classify these two directions of the vorticity vectors as primary and secondary structures; Figure 4.8. The relative helicity

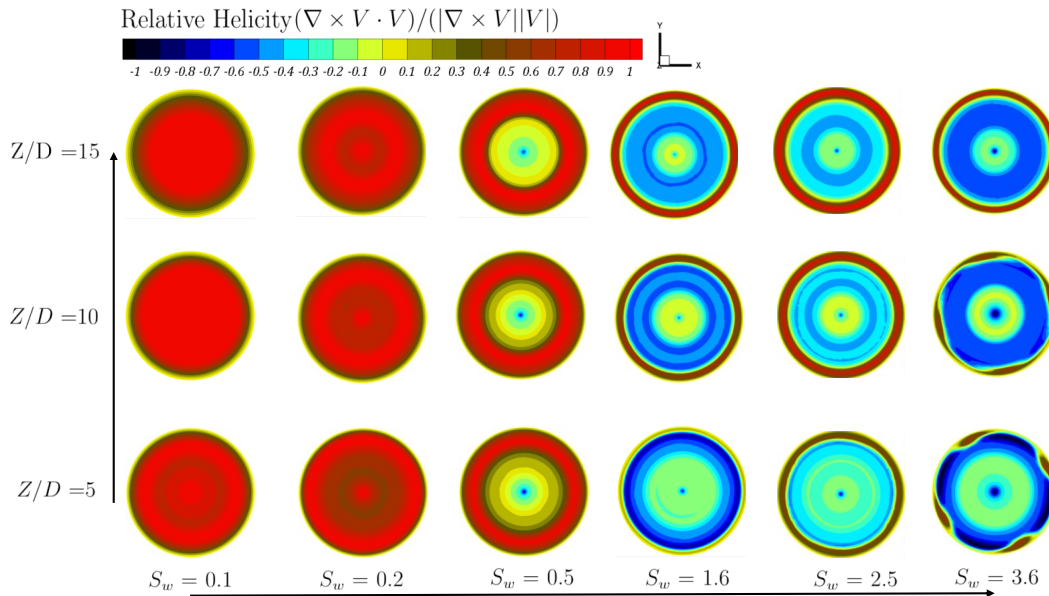


Figure 4.7: Dimensionless time-averaged helicity contours on various S_w on the transversal cross-section planes - $Z/D = 5, 10$ & 15

does not change the sign anymore, but the axial velocity changes a sign, which does not coincide with the sense change of the relative helicity. Thus, at the reverse flow zone, the parallel component of the local vorticity vector is in the opposite direction of the local velocity vector. We refer to this as a third structure. To summarize, at the wall-region, the axial velocity component of the local velocity is positive, and the parallel component of the local vorticity component is in the same direction; this is referred to as the primary structure. Further away from the wall, the axial velocity is positive, but relative helicity has changed the sign, so the parallel component of the local vorticity vector is in the opposite direction; this is referred to as the secondary structure. At last, in the reverse zone, the axial velocity of the local velocity vector is negative, and the relative helicity is negative; thus, the parallel component of the local vorticity vector is in the opposite direction. We refer to this as a third structure.

 $S_w > 0.5$

The relative helicity of the high swirl numbers appears to maintain similar characteristics, and the same three structures can be classified, compared to $S_w = 0.5$. However, the wall-region size shrinks significantly com-

pared to $S_w = 0.5$.

Figures 4.6 and 4.7 illustrate the magnitude of the relative helicity increases in downstream direction for all the swirl numbers, and the absolute maximum relative helicity happens at the center of the vortex.

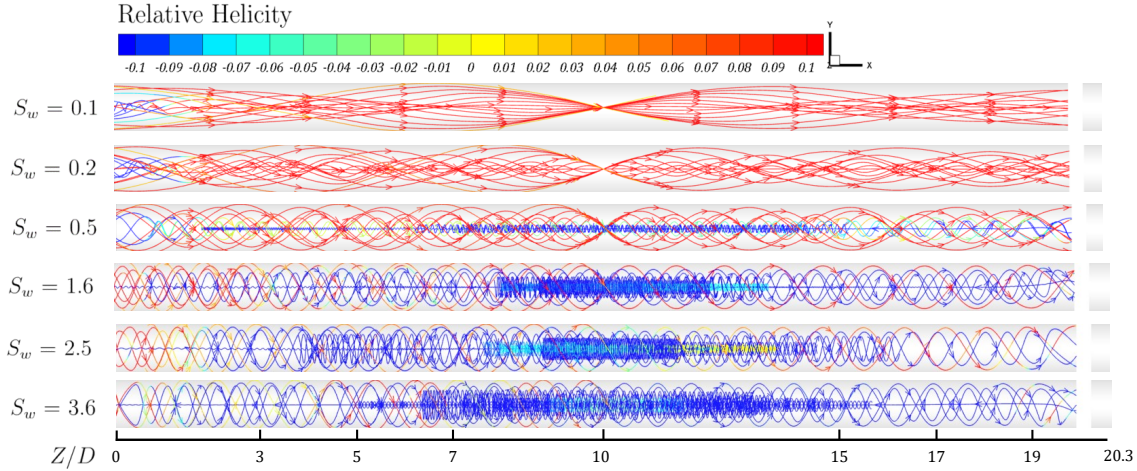


Figure 4.8: Flow streamlines on various S_w (Rake is created at $Z/D = 10$ plane. The relative helicity is used to color the streamlines)

$S_w = 3.6$ structures appear to be analogous with the one observed in the radial velocity profiles, and evidence of the swirl flow goes through a change of morphology is noticeable, from a "solid-body" to "Concentrated Vortex." Figure 4.8 exhibits helical nature which is common to swirl flow, and the pitch of these helical streamlines increases by increasing the swirl number.

Section 4.2.2 reviews the link between these structures and morphology of the flows with a possible pressure tomography of swirl flow.

4.2.2. Precessing vortex core and pressure tomography of swirl flow

We try to explore the possibility of using the pressure signals at the wall of the pipe for tomography of the swirl flows. The approach is to correlate the signal of the velocity components inside the fluid domain with the wall-pressure signals. Therefore the temporal behavior of the swirl flow is considered. Analyzing the temporal behavior of swirl flow requires to reduce the time steps to 0.25×10^{-4} seconds and increase the recording rate to 250 Hz. Another second of the flow-time was required to obtain the full resolution of the temporal flow behavior. This section analyzes two of the high swirl numbers.

Precessing vortex core frequency

Figures 4.9 and 4.10 exhibit the Fourier transform of the velocity components, and the associated wall-pressure at the same cross-section. The Fourier transform of the velocity components is obtained at a point where U_θ is maximum; also, the wall-pressure is obtained at the wall of the same cross-section.

The Fourier transform of the velocity component of the $S_w = 0.5$ marks the three different harmonies in the frequency domain. The signals were probed from the coordinate in the cross-section that the U_θ is maximum on that cross-section. The maximum axial and tangential velocities happen at a radial distance from the wall, and on this location, the relative helicity has a negative sign. As per introduced structures in section 4.2.1, this region is closer to the wall rather than the center of the pipe, but it is far enough to allow examination of the possible pressure tomography.

As it is expected, the amplitude of the tangential velocity in all domains is higher, and it follows with the amplitude of the axial component. At $Z/D = 19$, figure 4.9, the amplitude of the radial velocity is higher because of the presence of the flow straightener.

The wall pressure signal illustrates harmony between the strongest signal of the these velocity components, and the wall-pressure strongest signal correlates with frequency from the velocity components, at the different streamwise locations. The signal equations from these peaks, strongest pressure and velocity components show both signals happen with the same frequency domain, table C.1.

Figure 4.10 exhibits that there are no harmonies in neither velocities nor pressure signals for the first half of the tube, and the signal with the low frequency appears to be noise, but the judgment is difficult. If

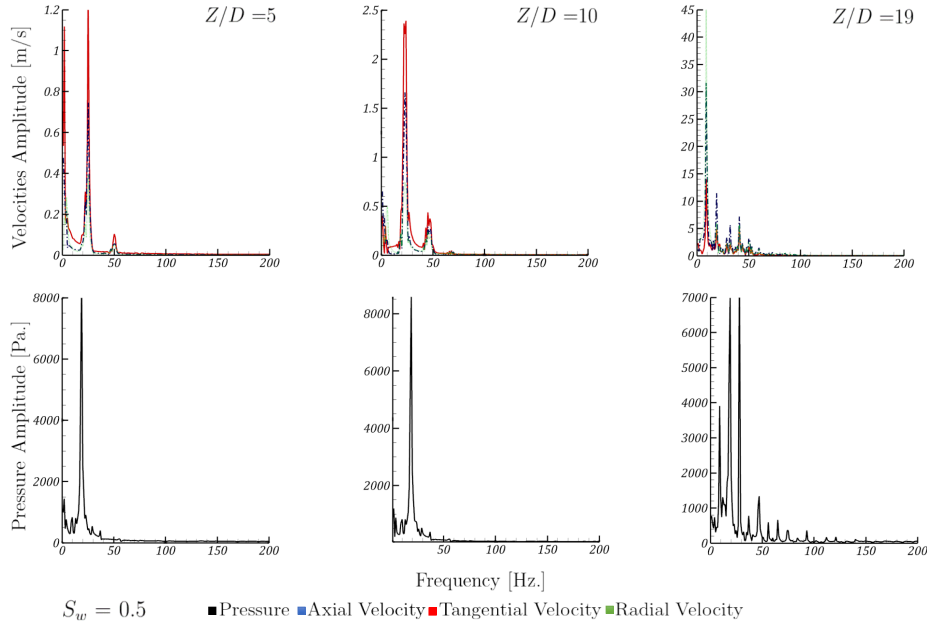


Figure 4.9: Fourier transformation of the axial, tangential, radial velocities, at the point of the maximum U_θ and associated wall pressure at the same cross-section

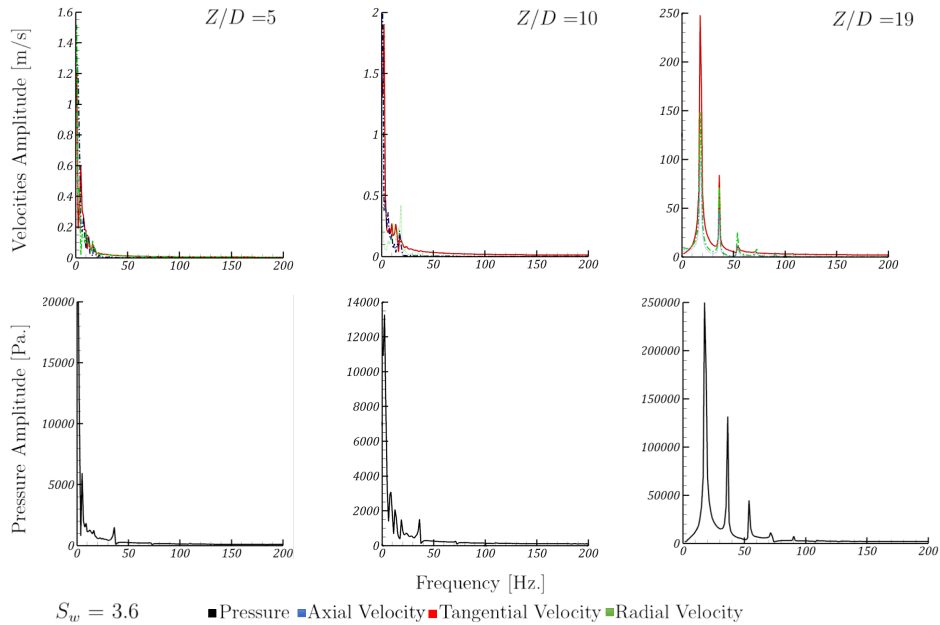


Figure 4.10: Fourier transformation of the axial, tangential, radial velocities, at the point of the maximum U_θ and associated wall pressure at the same cross-section

we assume, the peak at 4 Hz is not noise and considering the Fourier transform of the velocity components is obtained at a point where U_θ is maximum on that cross-section, then this signal represents the "solid-body" structure, Sections 4.1.2 and 4.2.1 explained that $S_w = 3.6$ behaves as a solid-body rotation flow until $Z/D=10$. In the solid-rotation, the maximum of the tangential velocity happens very close to the wall, and no free potential vortex shape is formed. Therefore, we expect a high amplitude and low frequency in from

the velocity components. This is the case, as the both pressure and velocity component signal show a strong amplitude signal at low frequency.

Further downstream a full correlation between the velocity components signals and the wall-pressure signal exists. The signal equations for the three peaks suggest they correlate in the exact same frequencies, Table C.2. Thus, there are possibilities for pressure tomography.

Star [3] studied the pressure distribution in swirl flows, and she reported a low-frequency signal 5Hz was presented in all of the power density spectra from all of the wall-pressure sensors. The same frequency is observed in this numerical study. The numerical results suggests that the 5Hz signal reported by her originated from the flow structure, and pressure sensors at the wall were detecting the flow morphology of the flow.

Also, the simulation results show that increasing the swirl intensity causes an increase in the amplitude and frequency of the region close to the wall. Tables C.1 and C.2 present the relation between swirl intensity and the frequency domain.

Van Camp [1] reported a 43Hz signal from the power spectrum of a single LDA measurement; the pump on his setup operated at the same frequency. Therefore, he could not conclude that it comes from the flow structure. Both Star [3] and Van Camp [1] concluded the low frequencies do not relate to precessing vortex core (equivalent to 5-12 and 25-36 Hz in our numerical), In this study, we only probe the signals at the location that the tangential velocity is maximum. The study suggests the signals from this point have a low frequency. The experiments report the existence of the signals in almost the same frequencies. Therefore, we believe that the low-frequency signals are originated from the wall region. . However, we cannot confirm that.

Star and Van Camp presented a higher frequency in a range of 80 - 100 Hz in their reports, while the maximum frequency observed in numerical studies is around 50Hz. The assumption is that the difference between these frequencies is related to the test setup. Both of them measured the frequencies of the flow with the presence of the collector tube while in our numerical setup the flow splitter is absent in the domain. Chapter 5 shows the presence of the flow split forces the core vortex inside the flow splitter, and the harmonics change.

Precessing vortex core behavior

Time-averaged relative helicity figure 4.7 and the flow-streamlines figure 4.8 show that the vortex core axis of the time-averaged velocity locates itself on the pipe axis. The temporal analysis shown that the core axis alternates around the pipe axis. So, the time-averaged presents the two axes overlay. However, the axis vortex core gradually drifts away from the pipe axis near the outlet, $Z/D = 15$, and the alternation around the pipe axis changes to a circular motion around the pipe axis, with the center of the circle located at the pipe axis, again. Figure 4.11 captures the circular motion at $Z/D=19$ for $S_w = 3.6$, and shows the local minimum of the pressure at the cross-section turns around the pipe axis. The radius and phase shift of the minimum local pressure in various cross-sectional planes shows that the radius of the circle increases as it gets closer to the outlet. The phase shift reveals that the pressure isosurfaces twist more toward the exit. We believe this circular motion does not represent the precessing of the axis of the vortex. It is generated because of present of the flow straightener at the outlet. Additionally, the radius of the circle and the phase shift angle increase by increasing the swirl number, and that shows a reactive torque behavior. Figures 4.11, D.1, and D.2 are references to this section.

4.2.3. Vortex breakdown

Section 4.1.1 highlighted, swirl flows above $S_w = 0.5$ exhibits a reverse axial flow region at the core of the vortex. Additionally, section 4.1.1 presented that the $S_w = 2.5$ illustrates a bull eye shape in the reverse region, which reflects the bubble-like breakdown structure with a stagnation point. The close examination of the axial velocity profile of $S_w = 2.5$ revealed that the axial velocity reaches to stagnation point at $Z/D = 13.18$ with a precise value of -0.002 m/s which compared with the surrounding fluids is significantly slower. This section tries to find out the possibility of the vortex breakdown on the most prone case of this research.

Leibovich [10] characterized the vortex breakdown by the formation of an internal stagnation point on the axis of the vortex. Faler [9] described the vortex breakdown comprehensively. Alekseenko [22] extends the vortex breakdown classifications for channels and unbounded flow in detail.

Bubble-breakdown creates a recirculation zone upstream of a stagnation point in the vortex axis. Flare [9] mentioned downstream of the bubble recirculation region; the axial velocity becomes positive at each radial position. Behind this region a new vortex is established accordingly.

Figure 4.12 shows the stagnation point at the cross-section $Z/D = 13.18$, and it reveals the stagnation area development (highlighted by white color, at the center). The development of the axial velocity profile exhibits

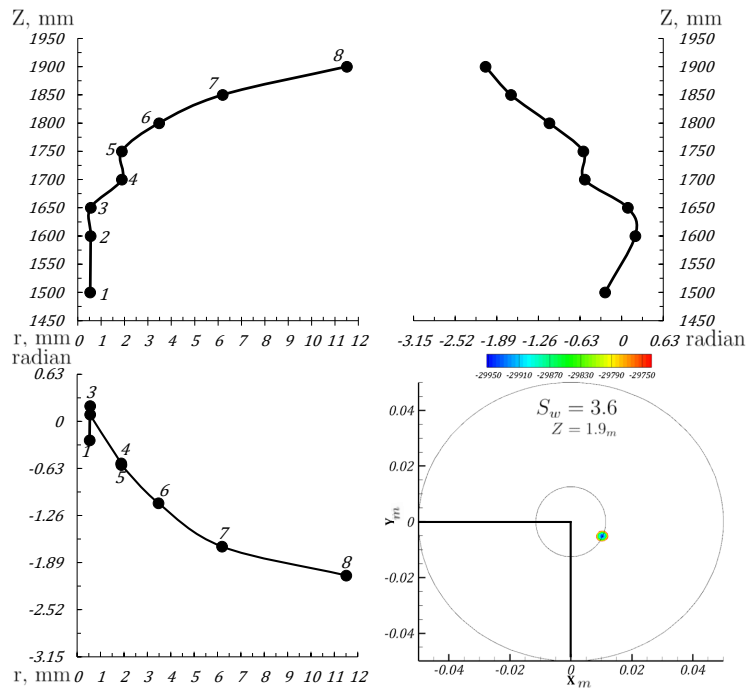


Figure 4.11: Circular motion of the axis of the vortex in three projections - $S_w = 3.6$

that the stagnation area started to develop at the vortex core from $Z/D = 10.18$. However, after the stagnation point, the axial velocity profile does not become positive, and the vortex is restored before its ultimate breakdown happens. Moreover, the relative helicity profile reveals that the axial velocity is almost zero, the value near to zero reveals that the streamwise velocity is significantly low. Figure 4.13 illustrates a complete restoration of the vortex axis at $Z/D = 16.18$. According to Gupta [23] and Sozou and Swithenbank [24], a precessing vortex core is one possible state of a swirl flow occurring after vortex breakdown. These conditions are not satisfied in $S_w = 2.5$ situations, and the precessing vortex core does not occur downstream of the stagnation point. Examining the pressure and tangential velocity profile does not suggest a formation of the new vortex beyond the stagnation point at $Z/D = 13.18$. According to Faler [9], the axial velocity profiles closely resemble the profile found in a conventional wake behind a solid body. None of the typical characteristics mentioned by scholars in above were developed. Thus, we hesitate to refer this stagnation point to as a vortex breakdown. One of the possible explanations is that the tube length is not long enough to develop vortex-break down. It

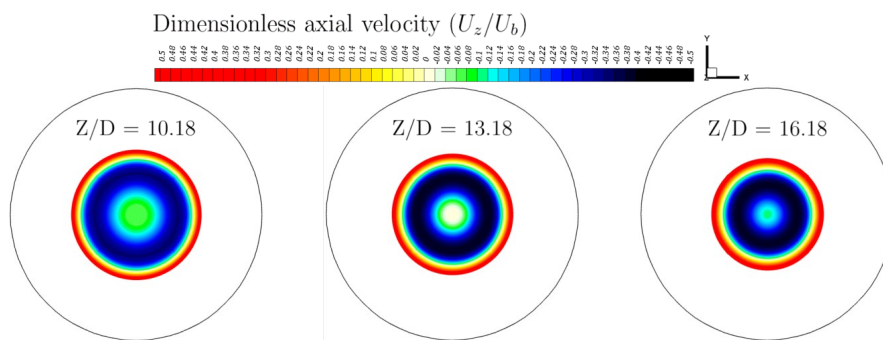


Figure 4.12: Dimensionless axial velocity - stagnation point at $Z/D = 13.18m$ - $S_w = 2.5$

appears the vortex breakdown is a function of swirling intensity, and swirl decay, which translates itself to the axial distance of the vortex core from the origin. Faler [9] pointed out that the swirl breakdown depends on the Reynolds and swirl number. Section 4.2.4 reviews the different structures that may occur inside the reverse flow zone.

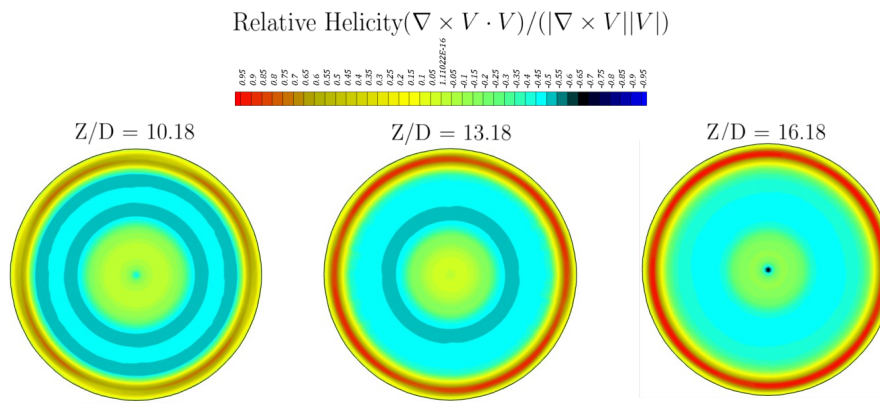


Figure 4.13: Relative helicity flow structure- stagnation point at $Z/D=13.18m$ - $S_w = 2.5$

4.2.4. Turbulent swirl flows

Kolmogorov's hypothesis for turbulence at very high Reynolds number defines the similarity roles in a turbulent flow. The first similarity hypothesis explains that the statistics of the micro-structure have a universal form. Figures E.1, E.2, E.3, and E.4 exhibit the axial and tangential velocity profiles of swirl flows for Reynolds numbers 150000, 100000, and 8000. As expected, the time-averaged velocity fields of a very high and close range of 150,000 and 100,000 present similarity, and this can even be extended to the much smaller Reynolds number as low as 8,000.

Nonetheless, the reverse flow zone exhibits subtle differences in close range of the high Reynolds numbers. Still, the main difference comes between lower and higher Reynolds numbers in the reverse flow region. The axial velocity profiles, figure E.1, present different behavior of the axial velocity in this zone. Additionally, figure E.2 shows the similarity is retrieved at $Z/D=19$.

Here, relative helicity is utilized to explain the different behaviors of the axial velocity profile inside the reverse flow zone. Sections 4.2.3 explains the conditions of a vortex breakdown, and fading the vortex axes is a sign of instability at the core of the vortex.

Figure 4.14 illustrates the relative helicity in various cross-sectional planes, which are known to the possible development of the instability in the vortex core. The vortex axis is located on the absolute maximum value of relative helicity. The flow with 150,000 Reynolds number presents a lower value of the absolute relative helicity from $Z/D = 10$ to $Z/D = 13$, which reflects that the axial velocity magnitude is getting closer to zero. The vortex axis is restored at $Z/D=17$, in which the absolute value of the relative helicity is increased. The flow with 100,000 Reynolds number illustrates the same behavior. Still, the axis core is retrieved at $Z/D=13$, and the vortex is more stable at $Z/D=17$, the absolute value of the relative helicity is larger at the core axis compared to 150,000 Reynolds number.

In contrast, the flow with a Reynolds number of 8,000 does not experience instability. The core axis remains at the pipe axis, and the core zone exhibits an area that the relative helicity remains at -1 throughout the pipe. Section 4.1.1 explained the characteristic change of the axial velocity profile is a sign of instability. Figure E.2 shows that for the high Reynolds numbers, the flow starts the formation of a W shape, while the flow with 8,000 reshaped from full U to V character. Here, we return to what was discussed before and presented that for swirl flow with a negative axial velocity at the center, V shape offers a stable vortex. Faler [9] identified the vortex stability is a Reynolds number dependence. Thus, for the same apparatus, the vortex breakdown can be seen if the Reynolds number is high enough.

4.2.5. Laminar swirl flows

The laminar behavior of the swirl flow in the pipe is beyond the scope of this research. However, a series of simulations were conducted to identify the limits of the steady-state and instantaneous unsteady behavior in the laminar regime. Table 3.3 presents the list of this numerical studies.

It appears that the swirl flow in the pipe is Reynolds and swirl number dependent in the laminar flow regime. The flow presented a steady-state behavior for all swirl numbers up to Reynolds number of 500. Then the swirl number unsteadiness kicks in at swirl number 2.5 for flows with Reynolds number of 500. The lower limit of the unsteady-state is Reynolds number of 500 and swirl number of 2.5. A comparison with higher Reynolds number simulation performed by H. A. Vaidya [21] (at Reynolds number of 1750) reveals

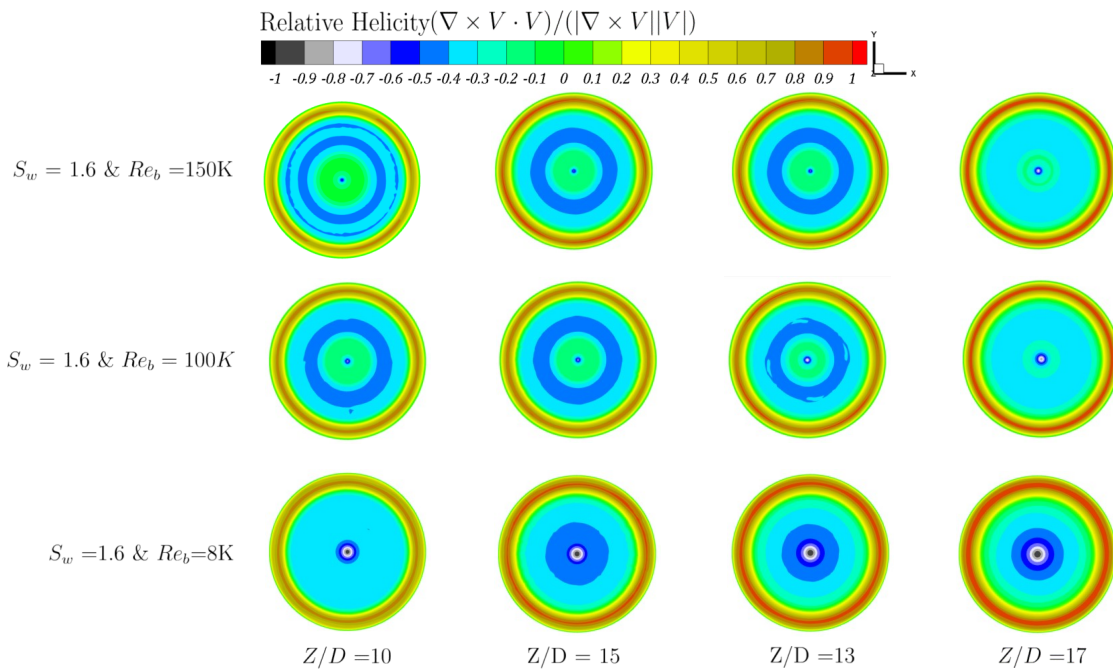


Figure 4.14: Dependence of swirl stability on Reynolds number - Relative helicity

that even in the laminar regime, the structure varies in different Reynolds number. Therefore, the behavior of the laminar swirl flows in the pipe requires more depth of study. Appendix F presents the velocity profiles obtained from the unsteady flow of swirl number 2.5 at Reynolds number 500. Figure 4.15 illustrates the structural differences between turbulent and laminar swirl flow in the pipe.

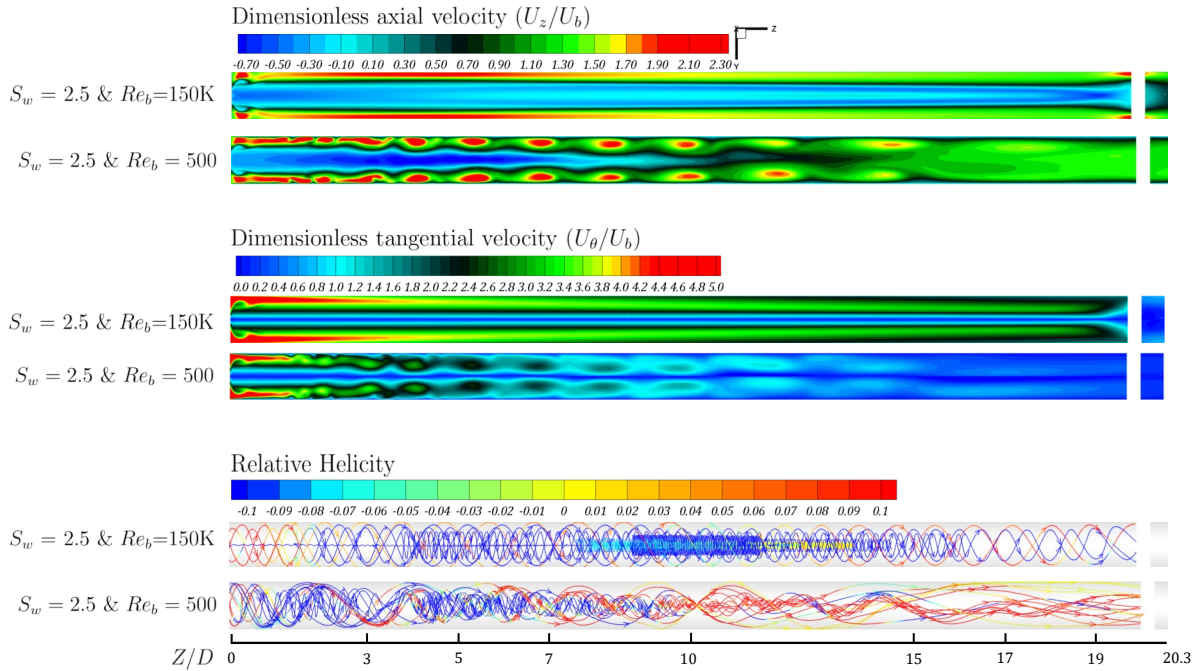


Figure 4.15: Comparison between unsteady laminar and turbulent swirl flows in a pipe

4.3. Flow morphology

This section provides an overview of swirl flow morphology in the pipe. Swirl flows are inlet boundary condition dependent, inbounded flows scale with apparatus diameter, and the vortex stretches out to the wall of the pipe, the geometry of the apparatus influences the instability of the vortex core and the vortex breakdown. This chapter exhibited that if the swirl number increases behind a critical number, a columnar vortex results with a reverse flow along the entire of the tube, which is reported by Kitoh [5]. Additionally, swirl flow instability is a function of the Reynolds number. Therefore increasing Reynolds number can lead to vortex breakdown in a given apparatus. Gupta [23] pointed out that combustion enhances the vortex breakdown. This research does not cover combustion, but it is essential to highlight the fact that prediction of the swirl flow in high Reynolds number requires RANS simulation, and Direct Numerical Simulation results OF lower Reynolds number cannot be extended to much higher Reynolds number. The fact that the performance of an inline swirl separator relies on the stability of the vortex generated inside the separator tube confirms that the industry still needs to rely on Reynolds Averaged Navier Stokes simulation to predict the performance of the swirl separators.

Moreover, the formation of the reverse flow beyond $S_w = 0.5$ indicates that inline swirl separators with a collector tube located downstream is born in the field of challenge. The next chapter covers the effect of the collector tube and swirls numbers in the design of Inline Swirl Separators. Figure 4.16 provides an overview of flow morphology based on two essential dimensionless numbers, S_w and Re_b . The morphology is defined as a function of these numbers. Plugging the numbers shall predict what is expected to be observed.

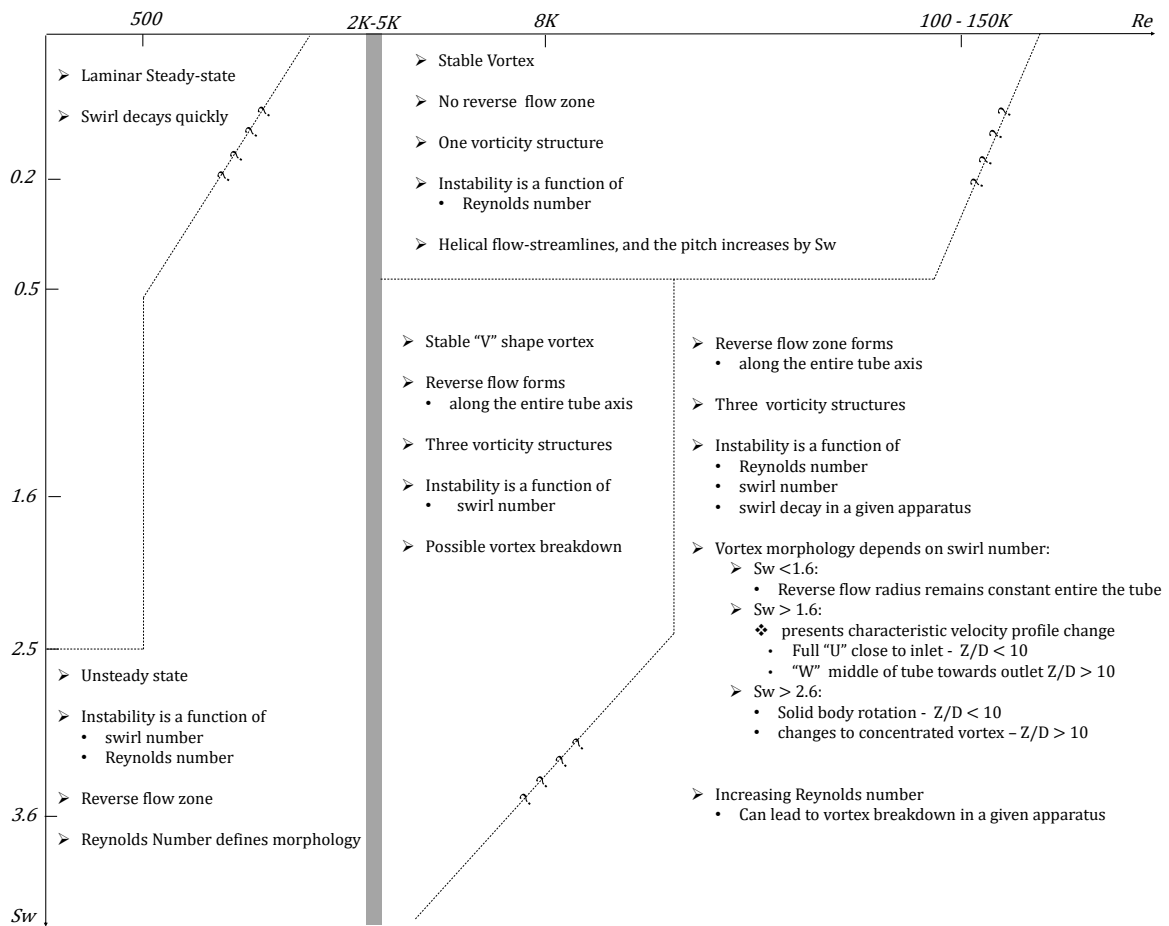


Figure 4.16: Prediction of the flow morphology based on Reynolds and swirl numbers- Axes are not scaled

5

Inline swirls separators

Inline Swirl Separators gained attention to replace the traditional gravitational separators, which are ill-favored due to the size and the processing time. Inline swirl separators with a downstream collector design draw more attention, as the collection process happens in the natural direction of the flow. Dirkzwager [8] worked on the design, Van Campen [1] performed two-phase flow experiments, Slot [2] simulated the test-setup from Van Campen, Star [3] performed pressure distribution experiment in a single-phase flow, and finally, Zeoten [4] develop a mechanistic model of the inline swirl separator. Chapter 4 covers the fundamental behavior of swirl flows in the separator tube. This chapter covers the effect of the collector tube on the behavior of the swirl and provides operation conditions for a design that will be used for a new mechanistic model.

Fifteen days of computation-time on 24-core of current CPU technology was consumed to complete each case that is presented in this and the previous chapters, a total of 28 times 15 days wall-clock is massive time for design considerations. The time and computation power highlight the requirement of building a new mechanistic model to predict the inline swirl separator efficiency at a more affordable time. The objective is to provide an accurate design platform to build the mechanistic model for the first tomography-controlled separator.

The two-phase results from Slot [2] reveal that the velocity fields of two-phase and single-phase swirl flow are identical. Thus, an accurate velocity field of one-phase is an acceptable approach to predict the operation efficiency of an inline swirl separator. This chapter focuses only on the optimum designs. The reader can find details of each case result in appendixes G, H, and I.

5.1. An accurate velocity field

Both Slot[2] and Zeoten [4] predicted the inline swirl separator efficiency. The result from both studies was close but significantly different from the experimental results from Van Camp [1]. Zeoten [4] assumed a constant axial velocity field based on the results from Slot. Slot [2] simulations did not predict the negative axial velocity at the center of the vortex. The negative axial velocity has a determinant effect on the performance of the inline swirl separator. Chapter 4 shown that when the swirl intensity reaches a critical level, a reverse flow along the entire tube axis is created. Harvey [25] and Kitoh [5] observed this type of flow. So, the future mechanistic model should consider this phenomenon. Additionally, chapter 4 revealed that the maximum diameter of reverse flow region happens between $Z/D = 3$ to $Z/D = 5$, where the tangential velocity reaches its maximum value. Therefore, the optimum design should to reduce the diameter of the negative velocity, while not causing a vortex breakdown in the separator tube.

Moreover, Van Camp [1] reported that the oil and water mixture formed an emulsion that hinders the separation efficiency. He assumed that the emulsion is the result of droplet breakdown through the narrow edge of the static swirl element. However, the emulsion could have been formed because of the recirculation of the oil inside the separator and collector tubes. This highlights the fact that the diameter of the reverse flow zone inside the collector should be either eliminated to minimized. Especially that the results for different mass flow-rate show that a secondary flow field forms at the verge of the entrance of the collector tube.

5.1.1. Indispensable change

Section 3.6 presented a comparison to Van Campen and Slot results, and the reverse flow zone was detected in that setup. Van Campen shows that increasing the Flow Split, hereafter (FS), improves the inline swirl separator efficiency. Nonetheless, within the range that separation is meaningful ($20 < FS < 80$), the dilute efficiency never exceeded more than 70%. A simulation was set to review the performance of the inline swirl separator with a swirl number, close to the range of Van Camp's setup, and higher FS. Figures 5.1 and 5.2 show the result of that simulation, with $S_w = 3.6$ and $FS = 50\%$. The simulation exhibits that the intensified swirl flow always creates a negative reverse flow at the center of the separator tube, which is extended into the collector tube. It appears that a design change is inevitable, and boosting the swirl intensity may not be

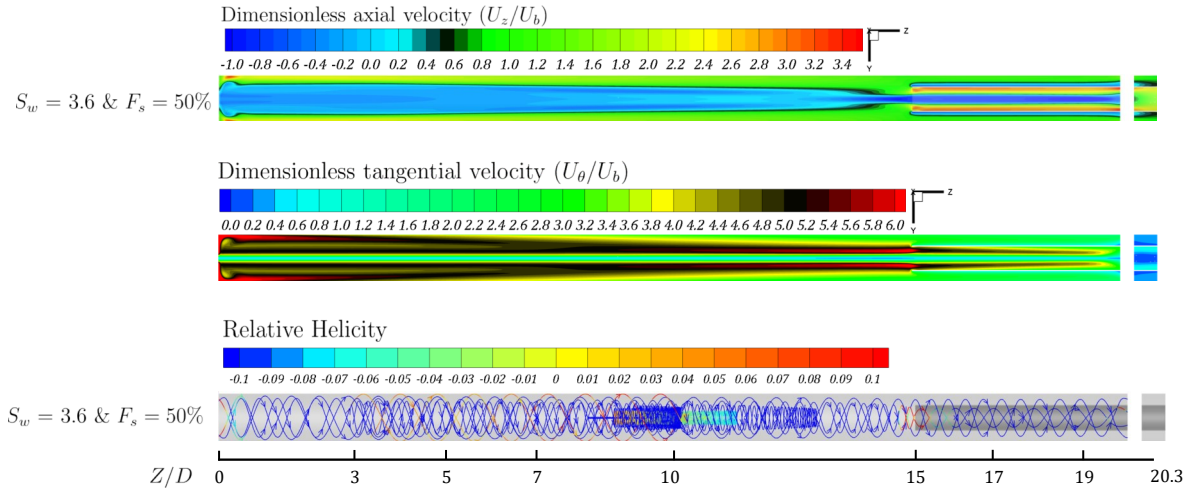


Figure 5.1: Intensified swirl design performance results - Cross-sectional at X=0

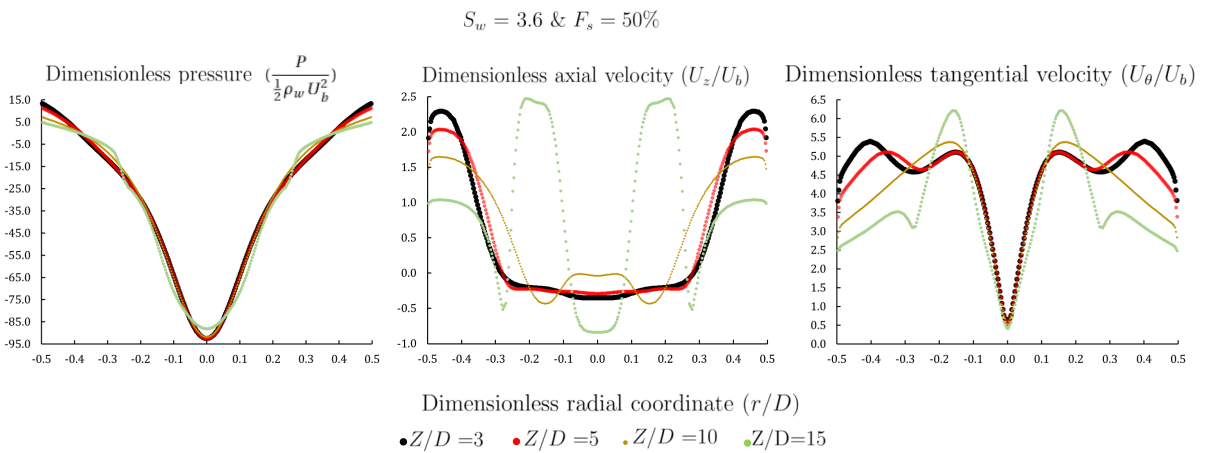


Figure 5.2: Dimensionless pressure, axial, and tangential velocity field at various transversal planes.

the best approach to design an inline swirl separator. Therefore, it is essential to understand the effect of the collector tube on the velocity field first. The next section covers the effect of the collector tube on the velocity field.

5.1.2. Collector tube and velocity field

Section 2.4.1 describes Flow Split (FS). A 25% setup represents a neutral flow split; therefore, it helps to recognize the effect of the collector tube on the velocity field. The collector tube causes an increase in critical S_w , and the diameter of the reverse flow zone decreases, and it forms a secondary velocity field at the verge of the collector tube with, an amplified tangential velocity and increase of the axial velocity. The effect is related to the fact that the area of the flow is reduced. Additionally, the vortex core, which is located at the pipe axis, is

confined inside a smaller diameter, and that boosts the magnitude of the tangential velocity locally. Figure 5.3 exhibits that the collector tube at the neutral flow split changes the velocity field to the extent that the reverse flow zone is almost eliminated. In the case of 25% , neutral, only the effect of the collector tube itself is considered.

Changes of the FS impacts the velocity field; since the flow is incompressible, the requirement of more mass flow-rate through the collector increases the axial velocity at the cross-section of the collector tube, and that is a positive impact to be explore more in detail.

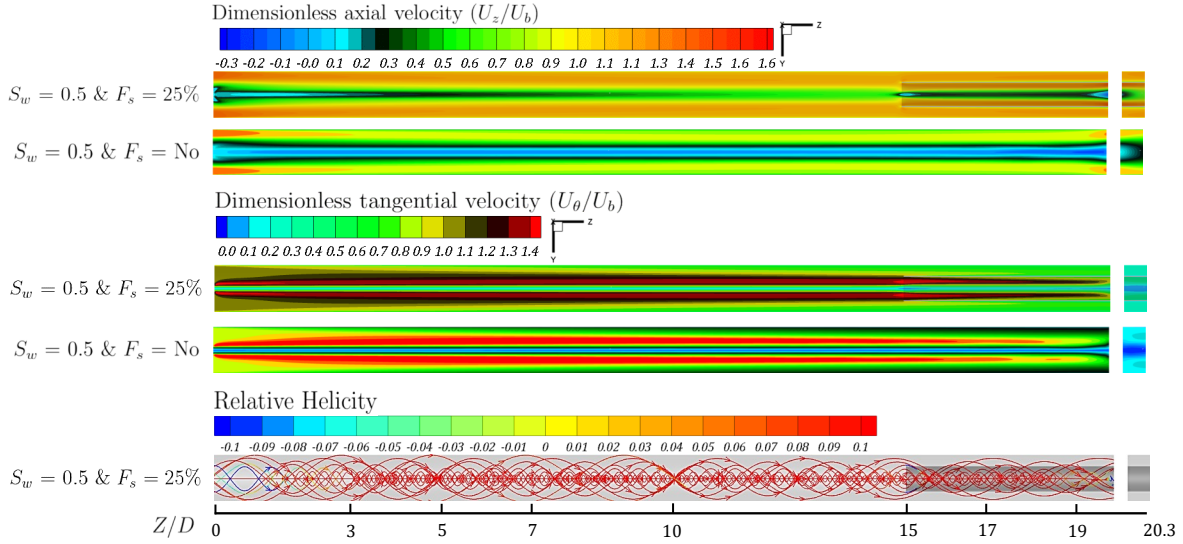


Figure 5.3: Effect of the collector tube and comparison with no collector- $S_w = 0.5$ & $F_s = 25\%$

5.2. Design considerations

A series of the simulations were executed to identify the best possible configurations in terms of the swirl number and the flow split to be considered as an optimum inline swirl separator for future design improvement and studies. Table 3.3 presents the list of the simulations, and appendixes G, H, and I provide the outcome of these numerical studies.

5.2.1. Essential design factors

The previous researches identified that the flow patterns in separators are intricate. This research tries to unveil the characteristic distribution of axial velocity, the criterion of reverse flow in the pipe, vortex breakdown features, and effect of collector tube on the velocity field of an inline swirl separator. It is crucial to consider the complexities of vortex flow for designing an inline swirl separator. In the past, the focus was to design a static swirl element that delivers enough angular momentum to separate two-phase liquid fluids. The tight spectrum of the specific gravities of liquids led the previous researchers to design a separator based on the delivery of the required high centrifugal force to achieve the separation. However, it appears to improve the separation efficiency the elimination of the reverse flow zone is the key. The higher swirl number generates enough angular momentum at the static swirl element, but the separation happens inside the tube. The separation efficiency is a function of the residence time of the lighter fluid inside the tube, and also, the centrifugal forces applied to the lighter fluid droplets. However, the separated lighter fluid should be transported out of the tube through the collector.

This part of the research highlights the essential considerations for the design of an inline separator.

Swirl intensity

This parameter is discussed in detail in this research. It is vital to consider that for every apparatus; there is a critical swirl intensity beyond, which a reverse flow region forms. In terms of a separator design, reverse flow is determinant, and causes low efficiency. However, every weak point is an opportunity. Perhaps an hollow static swirl element, which allows the collection in upstream, changes this disadvantage completely.

The hollow element opens an opportunity to increase the swirl intensity and take advantage of reverse flow. Nonetheless, collecting the low phase upstream is beyond the scope of this research.

Additionally, section 4.1.2 shows that the decay coefficient of the swirl is not constant, and it increases by increasing the swirl number. Therefore, the initial delivery of azimuthal velocity shall be compensated by vortex decay, vortex instability, and reverse flow region. Appendixes G, H, and I illustrate that there is a trade-off between the separation efficiency and the separation power.

Reynolds Number

Section 4.2.3 revealed that the vortex breakdown is a function of the Reynolds number. The Reynolds number dependency reveals that geometry and boundary conditions influence vortex instability. Vortex breakdown elimination is a prime objective of the design, at any expense.

Flow split

Section 5.1.2 showed that the collector effect on the velocity field. Van Campen [1] reported that an additional percentage of flow split increases efficiency. This chapter illustrates that additional mass flow-rate through the collector changes the pressure field on the verge of the collector tube entrance. Thus, the flow pattern changes in the vicinity of the collector tube, which has a positive impact on the efficiency. Figure I.6 shows the flow split effect for two swirl numbers. Appendixes G, H, and I present the pressure and velocity field behavior in detail.

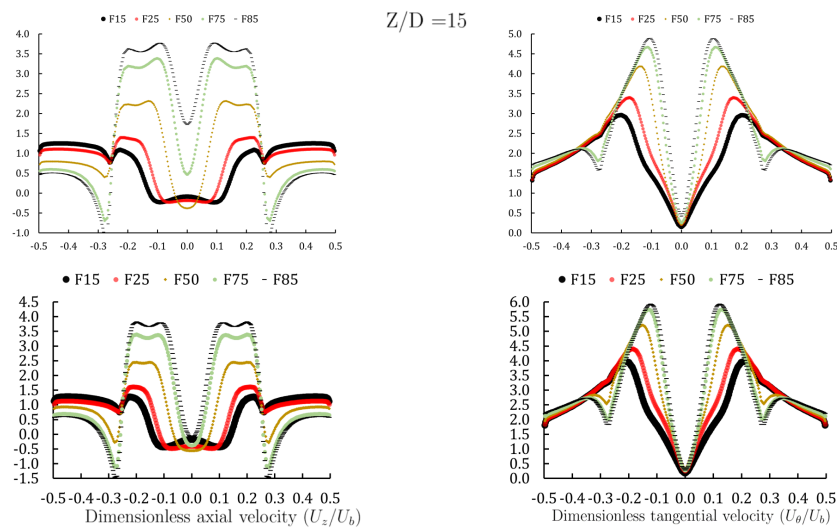


Figure 5.4: Effect of the flow split on velocity field at entrance of the collector tube. Top: $S_w = 1.6$ & Bottom $S_w = 2.5$

The counter effect of flow split

The intensive flow split has a counter effect on the separation efficiency. In addition to hindering the separation process by forcing the wrong phase into the collector tube, it causes a reverse flow along the wall of the collector tube in the annular section. Figure I.2 exhibit the reverse flow at $Z/D = 15$ and $Z/D = 19$. The same pattern happens in all high swirl numbers when the flow split goes over 50%. Figure 5.2 shows that in the case of $S_w = 3.6$ the reverse flow in the annular section happens even for a lower flow split.

Flow straightener

This research highlighted the positive impact of the flow straightener inside the collector tube. It appears that the swirling motion of the flow does not disappear for even a low swirl number. Therefore, for the integrity of the test rig and to avoid artificial effects on experimental results, it is recommended to use the flow straightener inside the collector tube. However, the main objective of the flow straightener is to recover the static pressure at the end of the separator and avoid a possible vortex breakdown inside the separator tube. The recommendation is to measure the accurate pressure drop across the flow straightener before the installation. In this research, a trial and error, with several simulations, was used to calculate the flow straightener inertial resistance coefficient.

Identical velocity fields

Slot [2] simulations reveal that the radial distribution of the velocity field for two-phase flow is similar to that of single-phase flow. This section takes advantage of this similarity to predict the oil droplet equation of the motion, to verify the performance of the swirl separator.

Water cut

Water cut is the ratio of water produced to total fluid produced. Typically, this ratio for brownfields, Enhanced Oil Recovery with water flooding techniques is high. The concept of selecting the separator is based on high water cuts, with dispersed oil droplets. The high volume of oil creates a column of oil at the center of the separator tube, which may reduce the requirement of the centrifugal forces; moreover, to understand the effect of the oil flooding (low water cut) requires separate research.

All factors mentioned above are considered to select the optimum inline swirl separator. The next section covers the detail, of the selected inline swirl separator.

5.2.2. The optimum Inline Swirl Separator

A careful examination of the simulation cases provided in appendixes G, H, and I revealed that the separator with a configuration of " $S_w = 1.6$ & $F_s = 50\%$ " passed all the critical design considerations and exhibited an acceptable performance for separation of the oil droplets.

$S_w = 1.6$ & $F_s = 50\%$

The performance of an inline swirl separator is sensitive to the operating parameters. We use the opportunity to reflect that a change of the flow split in percentages causes the change of the velocity field inside the separator tube. Figure 5.5 presents the performance of the separator in a close range of the flow splits. Furthermore, it illustrates that even for a selected design, a narrow margin of operation limits exists. It is vital to mention that the performance of the separator is a function of the fluid properties and the geometry of the apparatus. For instance, in the same apparatus, changing the inlet diameter will change the bulk Reynolds number, which affects the vortex instability, and the flow split ratio. Although there is no universality in design, the key parameters to start the design are U_b , D_{inlet} , S_w and $D_{collector}$. The other design parameters shall be calculated based on these essential factors.

5.2.3. Separator efficiency

The selection process exhibits that the best performer is much weaker than what has been initially designed by previous researchers. The last question remains in whether the total angular momentum field generated by the selected separator is strong enough to perform adequately, and what are the operation limits of the separator. This section utilizes the prediction of the radial trajectory of the particles to illustrate that $S_w = 1.6$ & $F_s = 50\%$ delivers sufficient angular momentum. However, the target is not to optimize the limit of the operation. Section 2.4.3 explains the assumptions for predicting the radial oil trajectory. The most important forces to predict the radial trajectory of the particle, are the buoyancy force F_B and the inertial forces F_I ; the ratio of these forces defines the separator efficiency. The following assumptions enable us to predict the oil droplet trajectory.

- Oil droplet is in a quasi-steady state, means the forces acting on the droplet are balanced.
- Flow-field is in a quasi-steady state, means the mean-flow properties do not change with the time
- Distribution of the velocity for two-phase flow is similar to that of single-phase flow.
- The effect of turbulence on the droplet motion is neglected. Only the forces due to the mean velocity field are considered

Figure 5.5 shows that the ratio of $\frac{U_\theta}{U_z}$ is at the minimum close to the wall in each cross-section. Therefore, the worst-case scenario in separation is an oil droplet that is located in the wall region. The initial coordinate of (0, 0.0498, 0.2) is considered, the diameter of the pipe is 0.050m.

The radial velocity of the oil droplet is computed based on the actual velocity field derived from the simulation. Based on the computed radial velocity and the actual velocity field, the trajectory of the oil droplet was computed for several cases to determine the oil specification that the separator can effectively separate from the brine. Figure 5.6 shows the oil droplet trajectory.

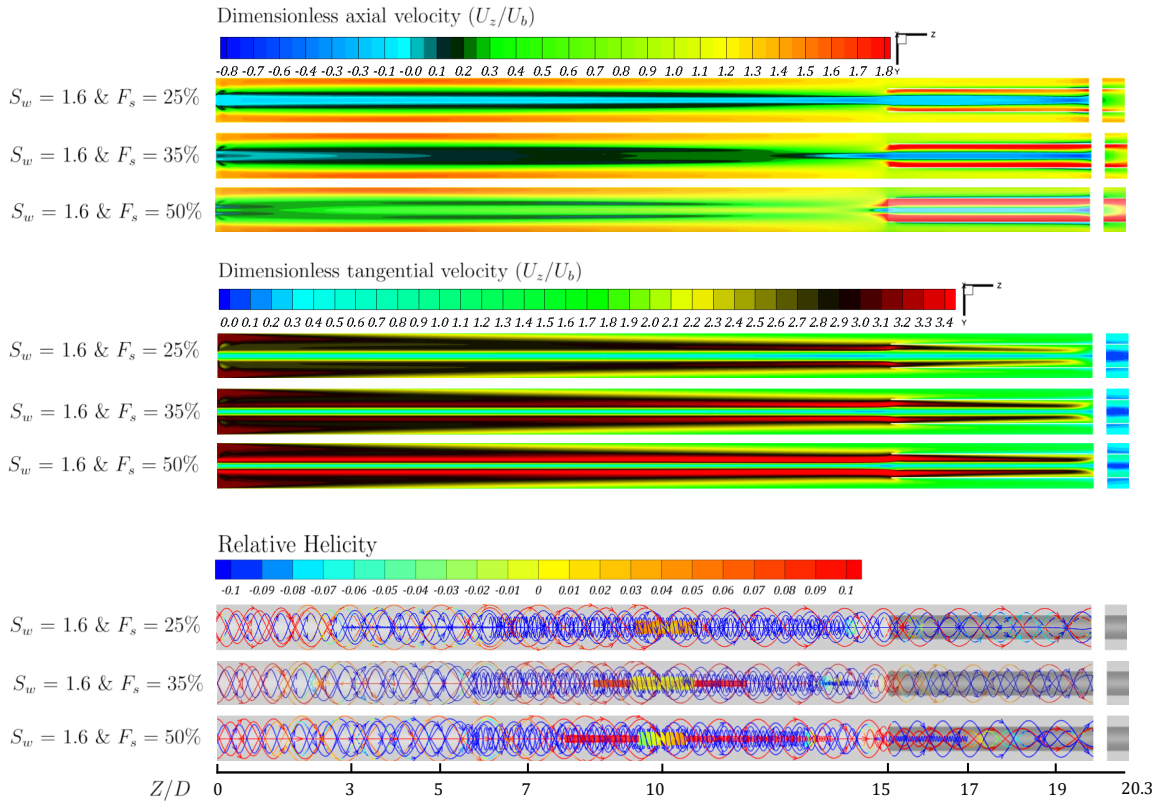


Figure 5.5: Dimensionless time-averaged axial, tangential, and pressure field. Colored flow-streamline $S_w = 1.6$

Table 5.1 presents the specification oil that the inline swirl separator extracts from its brine. The brine specifications were kept constant. It appears the inline swirl separator generates enough separation power to separate light oil with a droplet size larger than $90\mu m$. from the brine. The USA energy administration reports that the light oil composes 70% of the daily oil production in the USA. Thus, the candidate swirl separator has a market and worth further optimization and studies.

Table 5.1: Specification of the oil that $S_w = 1.6$ & $F_s = 50\%$ separates effectively - constant brine specification

Swirl Spec		Geometry	Brine spec		Oil Spec	
S_w	F_s		SG	μ	D_o	API - SG
1.6	$\approx 50\%$	Section 3.7	1.1	$1.183 \times 10^{-3} Pa.s$	$> 90\mu m$.	$>28^\circ - > 0.887$

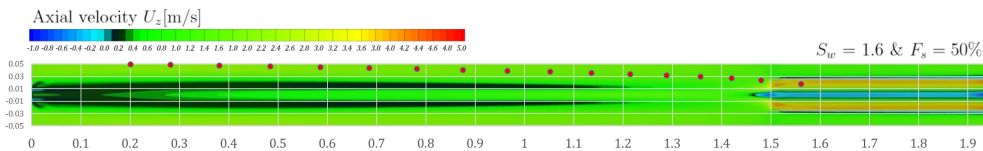


Figure 5.6: The oil droplet trajectory for $D_o = 100\mu m$. & $API = 30^\circ$ - Based on simulated velocity field

6

Conclusions and recommendations

6.1. Conclusions

This numerical study suggests that the dynamic behavior of swirl flows in a pipe is determined by the intensity of the swirl flow, which is quantified by the swirl number. The swirl intensity shapes the axial velocity profile at the core of the vortex. When the swirl number increases beyond a critical number, a columnar vortex appears, with a reverse flow along with the center of the entire tube.

The swirl intensity decays along the wall of the pipe; the swirl intensity, and the decay of it, form the shape of the axial velocity profile. In case the disturbance of the flow results in a stagnation point at the vortex axis, it may develop a vortex breakdown. The vortex breakdown in high Reynolds numbers ($Re_b > 100,000$) is a function of the swirl number, and the instability at the vortex core increases by increasing the swirl intensity.

Furthermore, the results show that the stability of the vortex is a function of the Reynolds number. Considerable reduction of the Reynolds number kicks in the effect of viscous forces, which stabilize the vortex core. Reynolds and swirl numbers determine the dynamic of the low Reynolds number but turbulent, swirl flow. Therefore, the industry needs to rely on Reynolds Averaged Navier-Stokes (RANS) simulations; Direct Numerical Simulation predictions obtained at much lower Reynolds numbers may not predict the occurrence of the vortex breakdown inside the pipe.

In the laminar region, the swirl flow remains in steady-state for low Reynolds number, and the flow becomes unsteady in the higher Reynolds and higher swirl numbers. In these regards, these limits were found at 500 and 2.5, for the Reynolds and swirl numbers, respectively. The study shows that for low Reynolds number, the viscosity is important, and the stability of the vortex is a function of the Reynolds and swirl numbers, both in turbulent and laminar flow.

These findings show that there are essential design considerations, which determine the efficiency of the swirl separator. Thus, a combination of the geometry parameters and the swirl flow characteristics should be considered to avoid the reverse flow zone and vortex breakdown inside the inline separator.

One of the vital elements of the inline swirl separator is the collector tube. The study shows that the collector tube at the neutral flow split, with no bias of the mass flow-rate at each outlet, changes the velocity to the extent that the reverse flow zone for $Sw=0.5$ is eliminated. Pressure actuators can control the flow; therefore, controlling the flow split at both outlets. The numerical results show that an additional percentage of flow split enhances efficiency by eliminating the reverse flow zone for the higher swirl numbers. Additionally, the study reveals the counter effect of the extreme flow splits, which hinders the efficiency of the inline swirl separator. These optimal settings for the geometry of this research were found at swirl number 1.6 and flow split of 50%.

6.2. Recommendations

For future numerical studies, it is recommended to consider a computational mesh that is refined at the center of the pipe, in order to capture the subtle axial velocity behaviors at the center of the pipe. The quadrilateral face of the hexahedral elements of the mesh should be in the order of one millimeter, and the angle that contains each element should be less than 3° . The simulation time steps should be small enough to capture the temporal behavior of the flow, and the criterion is to be at least one-quarter of the time that the Rankine vortex rotates at its radius. It was found that 0.25 milliseconds is the maximum time step that can be

set to obtain temporal behavior of the flow at an acceptable resolution, and the record rate can be adjusted for spatial time-averaged studies to 20 times the temporal recording rate.

It appears that initializing and starting the simulations with realizable $k-\epsilon$ helps the stability of the Reynolds stress model simulations.

The current hypothesis is that the length of the pipe in this research was not long enough to observe the vortex breakdown. Another numerical study with a longer pipe may reveal the details of the vortex breakdown and help to understand the operation limits of the inline swirl separator. Also, a precessing vortex core is one possible state of a swirl flow occurring after a vortex breakdown. A 3D Lagrangian particle tracking for the oil droplet trajectory could contribute to a better understanding of the separator efficiency.

A

Initial velocity distributions

The experimental results (Kitoh [5], Steenbergen [9], Drikzwagner [10], and Van Camp [1]) suggest the azimuthal component of velocity resembles a distribution similar Rankine vortex at the inlet, with a solid body rotation in the center and potential flow vortex at the larger radius. The different swirl numbers, with different experimental setup reveals the possibility of the simplification. The axial velocity profile at the inlet,

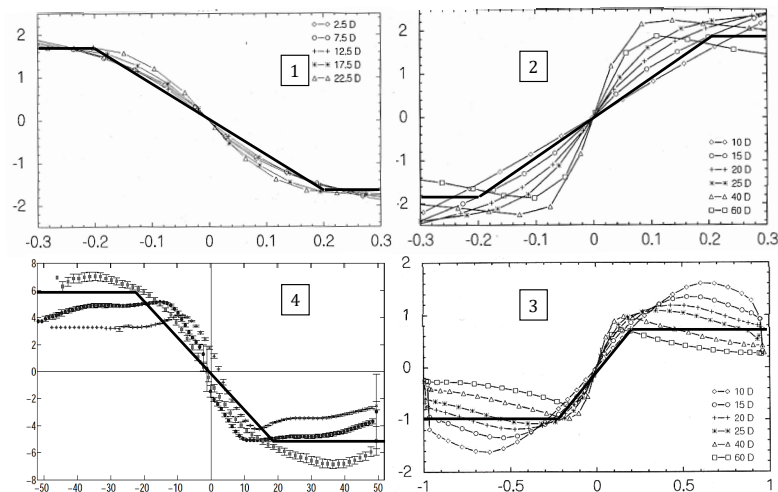


Figure A.1: pictures 1,2,3- Dirkwager[8] & 4: Van Campen [1] experiments for different swirl elements. Solid lines are simplified distribution - pictures from cross-section, close to the inlet $Z/D < 4$

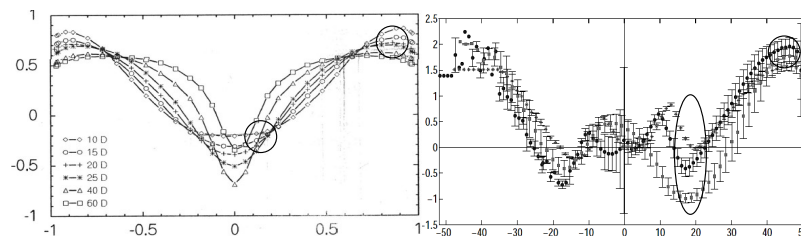


Figure A.2: Left: Dirkwager & Right: Van Campen experiments for the weak, strong, and big swirl elements- the circles indicate the radial position of the maximum and minimum of the axial velocity at inlet position $Z/D = 10$,

encounters its minimum value at the radius of the core of Rankine vortex. While, its maximum value, occurs at $\frac{7}{10}$ of the pipe radius (r).

B

Time-Averaged Velocity Profiles

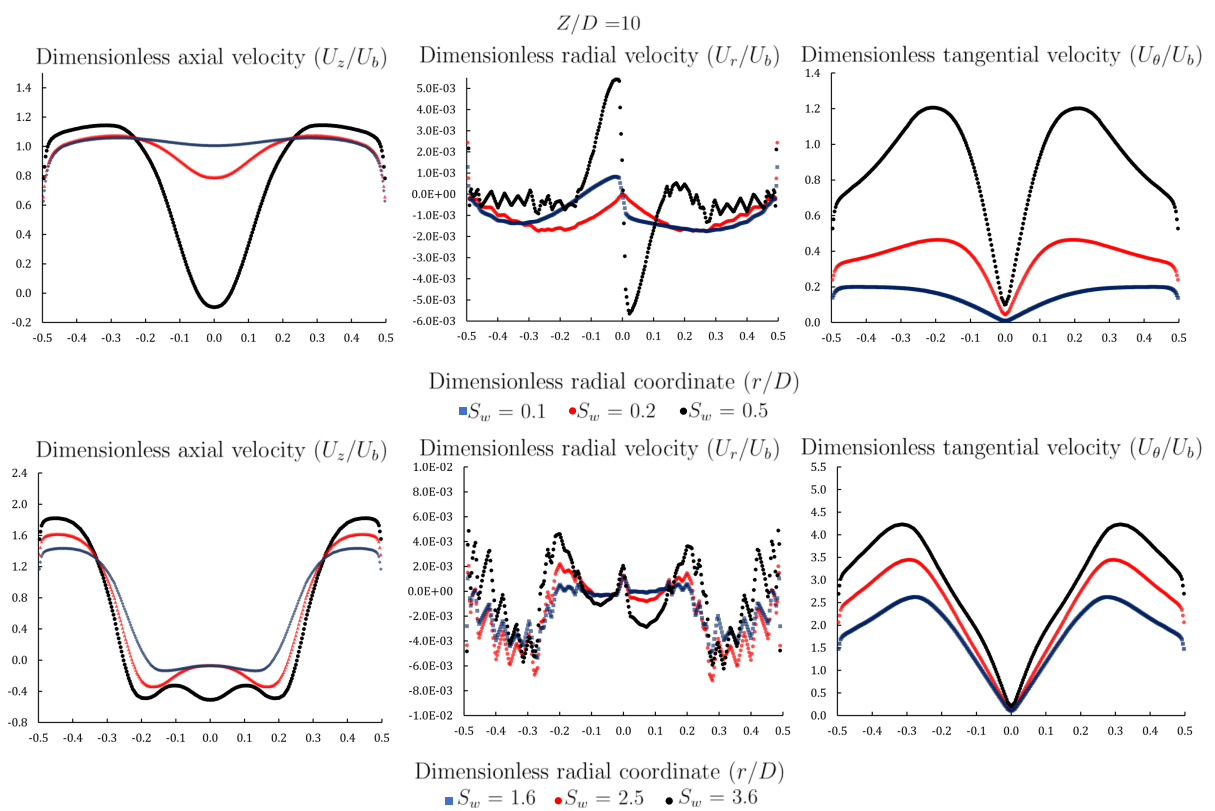


Figure B.1: Dimensionless time-averaged radial velocity contours for various S_w on the cross-sectional and transversal planes

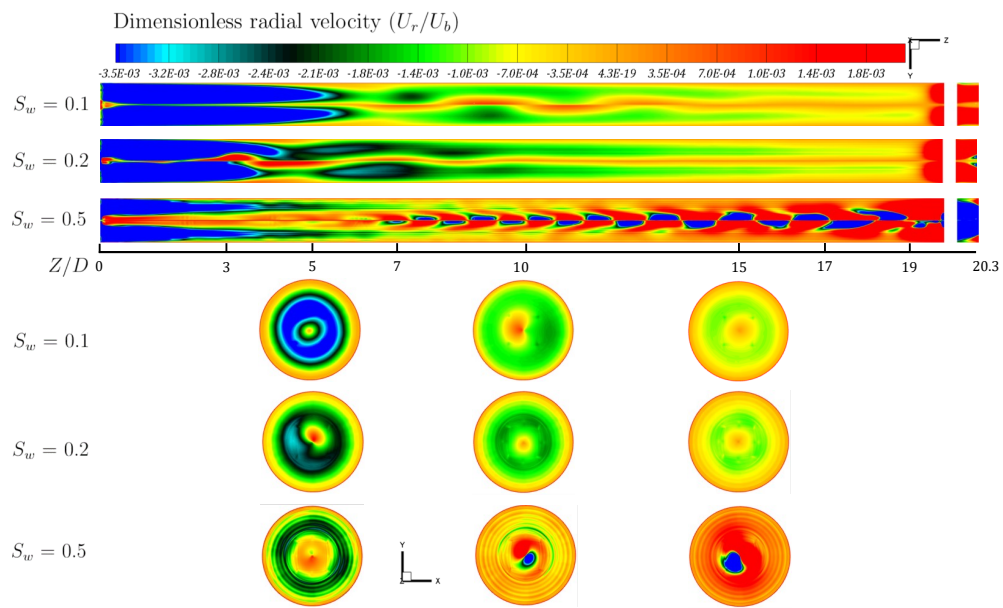


Figure B.2: Dimensionless time-averaged radial velocity contours for various S_w on the cross-sectional and transversal planes

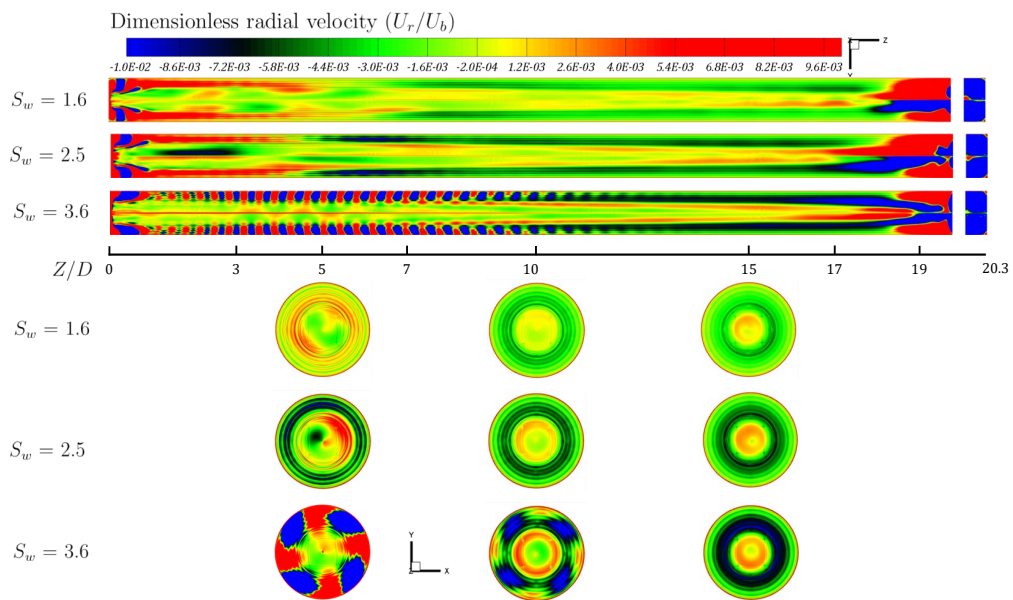


Figure B.3: Dimensionless time-averaged axial, radial, and tangential velocity profiles for various S_w on the transversal planes



Wall-pressure and velocity components signals

Table C.1: Equation of the signals - $S_w = 0.5$ - Velocity signals at the location of the maximum U_θ , and Pressure signals at the wall cross-section

Signal Component	Signal Equations		
	Z/D = 5	Z/D = 10	Z/D = 19
Axial velocity	$0.35 * \cos(4t + 1.3)$	$0.38 * \cos(4t - 2)$	$31.65 * \cos(9t + 2.6)$
	$0.75 * \cos(25t - 2.9)$	$1.66 * \cos(23t + 1.8)$	$11.00 * \cos(20t + 0.4)$
	$0.05 * \cos(50t + 3.1)$	$0.29 * \cos(45t - 0.9)$	$7.20 * \cos(40t - 0.49)$
Tangential velocity	$0.18 * \cos(4t + 1.5)$	$0.30 * \cos(4t + 0.8)$	$14.02 * \cos(9t + 0.76)$
	$1.30 * \cos(25t - 2.9)$	$2.39 * \cos(23t + 1.7)$	$5.04 * \cos(20t - 1.06)$
	$0.02 * \cos(50t + 1.6)$	$0.43 * \cos(45t - 0.2)$	$5.33 * \cos(40t - 1.36)$
Radial velocity	$0.28 * \cos(4t - 0.48)$	$0.45 * \cos(4t + 2.3)$	$47.43 * \cos(9t - 0.54)$
	$0.39 * \cos(25t + 1.1)$	$0.74 * \cos(23t - 0.6)$	$5.92 * \cos(20t - 5.88)$
	$0.05 * \cos(50t - 0.6)$	$0.24 * \cos(45t - 2.2)$	$5.63 * \cos(40t + 2.67)$
Wall Pressure			$3903 * \cos(9t - 0.45)$
	$8580 * \cos(21t + 2.9)$	$8591 * \cos(20t + 2.89)$	$6987 * \cos(20t - 2.82)$
			$1339 * \cos(47t - 0.47)$

Table C.2: Equation of the signals - $S_w = 3.6$

Signal Component	Signal Equations
Axial velocity	$148.50 * \cos(18t + 2.96)$
	$71.730 * \cos(36t + 1.50)$
	$25.060 * \cos(54t - 2.91)$
Tangential velocity	$247.70 * \cos(18t + 1.40)$
	$84.130 * \cos(36t - 0.27)$
	$10.880 * \cos(54t + 1.51)$
Radial velocity	$102.77 * \cos(18t - 0.03)$
	$46.730 * \cos(36t - 1.59)$
	$12.690 * \cos(54t - 0.23)$
Wall Pressure	$254137 * \cos(18t + 1.48)$
	$131778 * \cos(36t + 0.26)$
	$44799 * \cos(54t + 3.090)$

D

Circular motion of the axis of the vortex

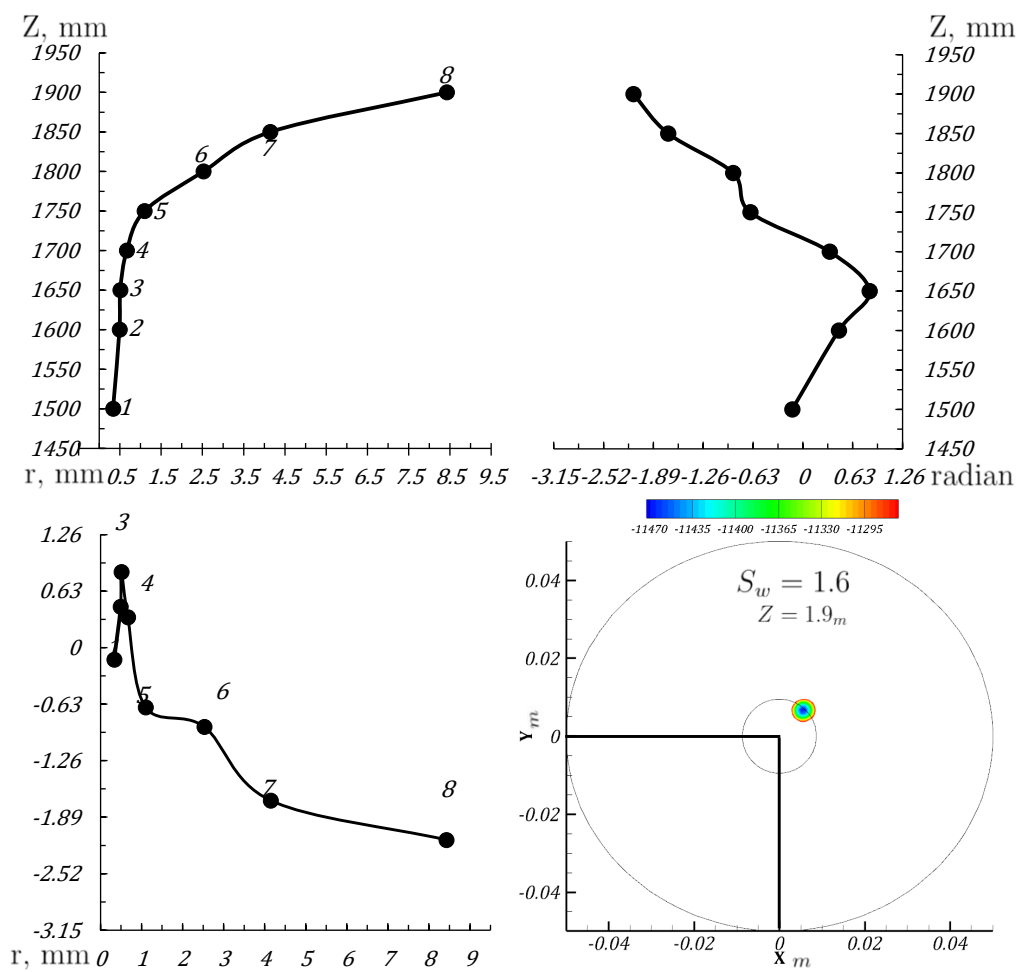


Figure D.1: Circular motion of the axis of the vortex at $Z=1.9\text{m}$ - $S_w = 1.6$

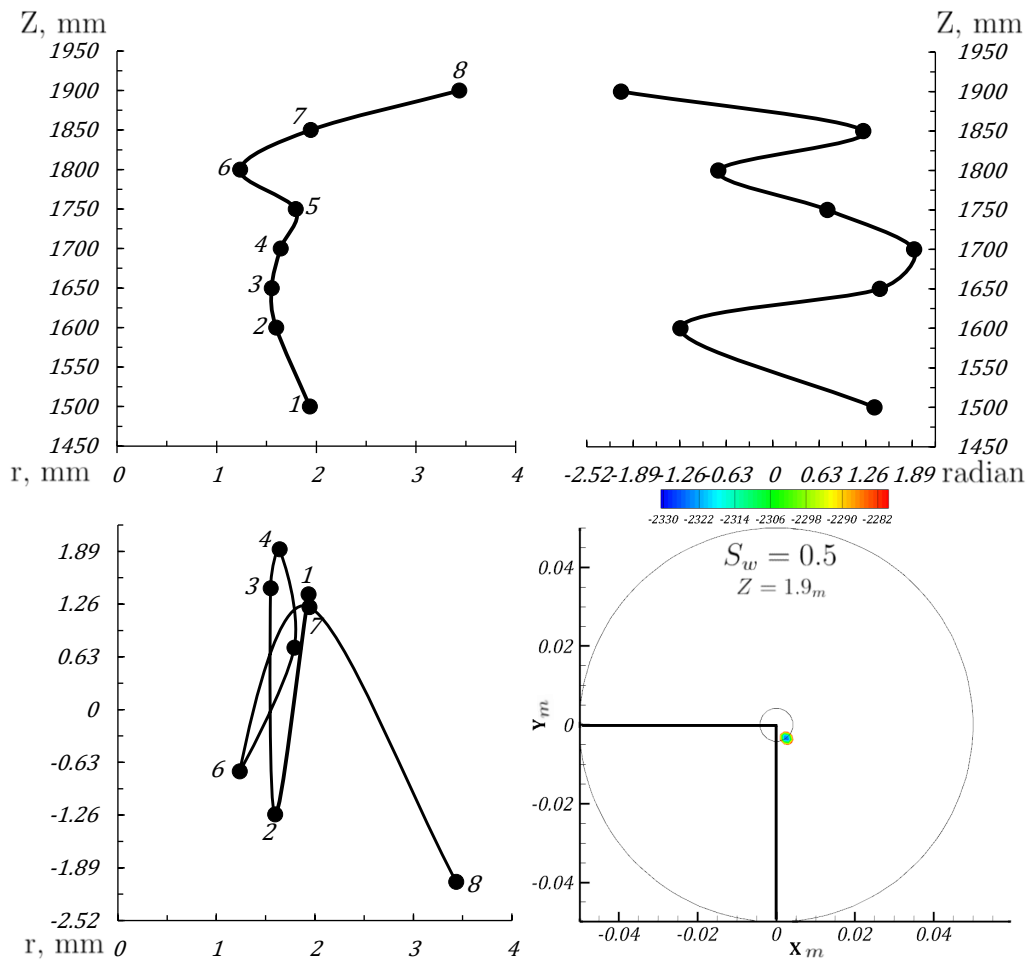


Figure D.2: Circular motion of the axis of the vortex at $Z = 1.9\text{m}$ - $S_w = 0.5$

E

Similarity Turbulent Vortex flow

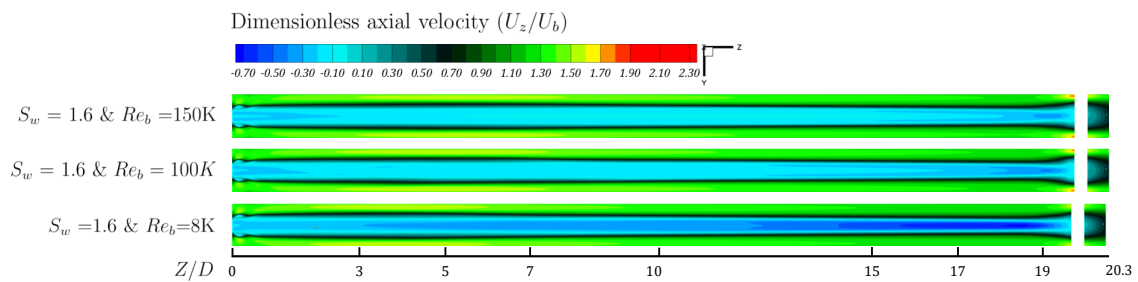


Figure E.1: Dimensionless time-averaged axial velocity profiles on various Reynolds numbers- $\frac{X}{D} = 0$

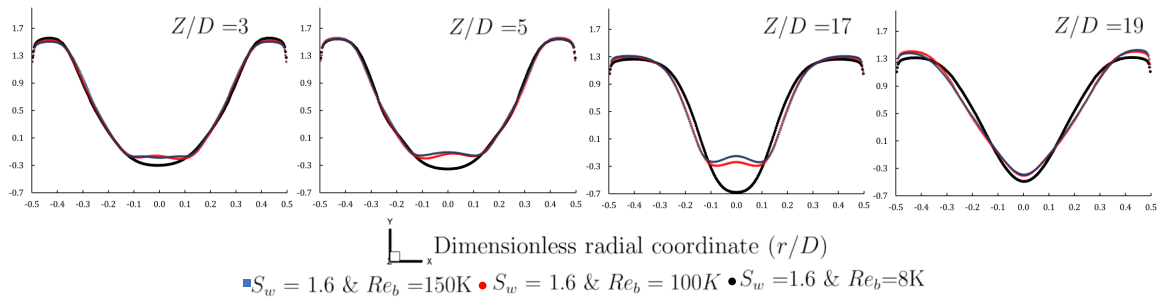


Figure E.2: Dimensionless time-averaged axial velocity profiles of various Reynolds numbers- $\frac{Z}{D} = 3, 5, 17 \& 19$

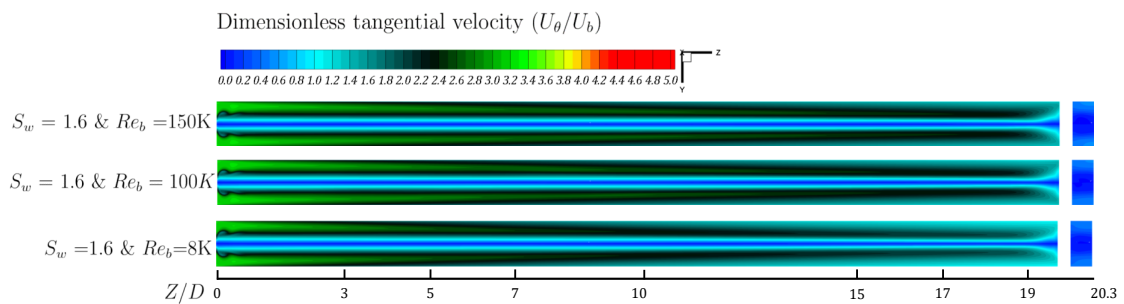


Figure E.3: Dimensionless time-averaged tangential velocity profiles of various Reynolds numbers- $\frac{X}{D} = 0$

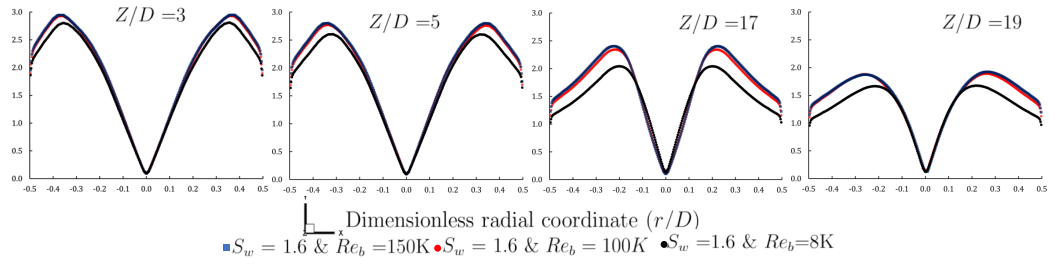


Figure E.4: Dimensionless time-averaged Tangential velocity profiles on various Reynolds numbers- $\frac{Z}{D} = 3, 5, 17 \& 19$

F

Comparison between turbulent and laminar Vortex flow

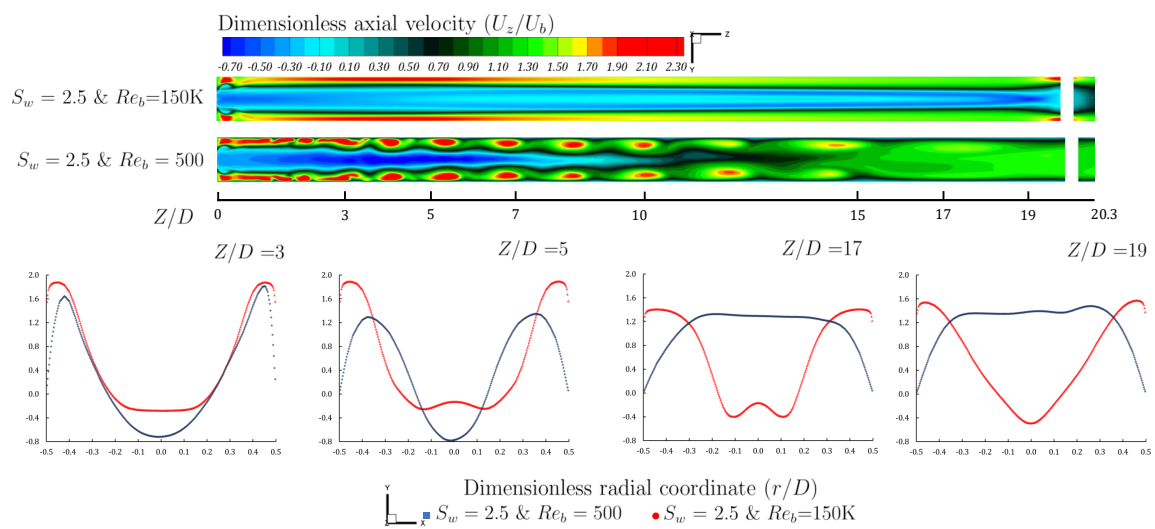


Figure E1: Comparison between unsteady laminar and turbulent swirl flows in a pipe -Axial Velocity profile

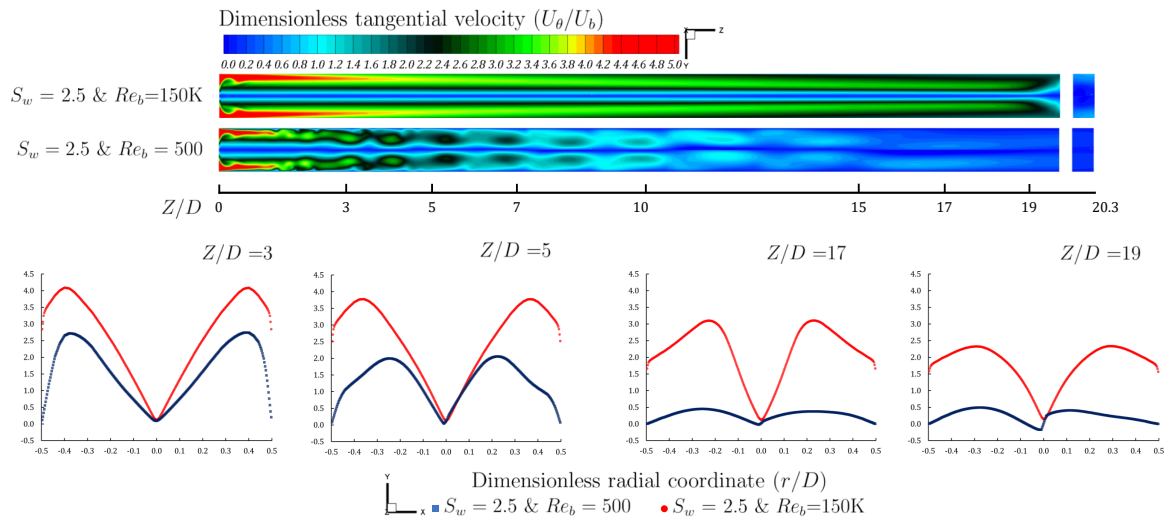


Figure E2: Comparison between unsteady laminar and turbulent swirl flows in a pipe -Tangential Velocity profile

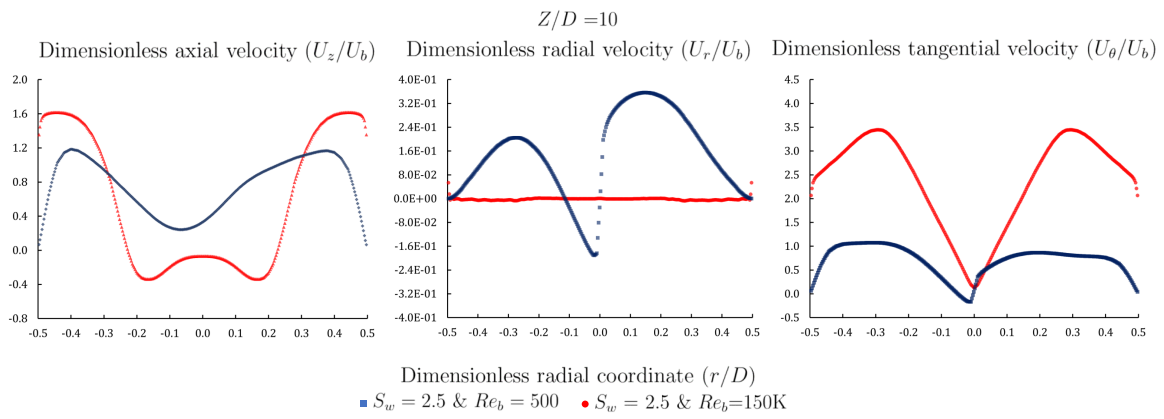


Figure E3: Comparison between unsteady laminar and turbulent swirl flows in a pipe, cross-section profile in the middle of the pipe

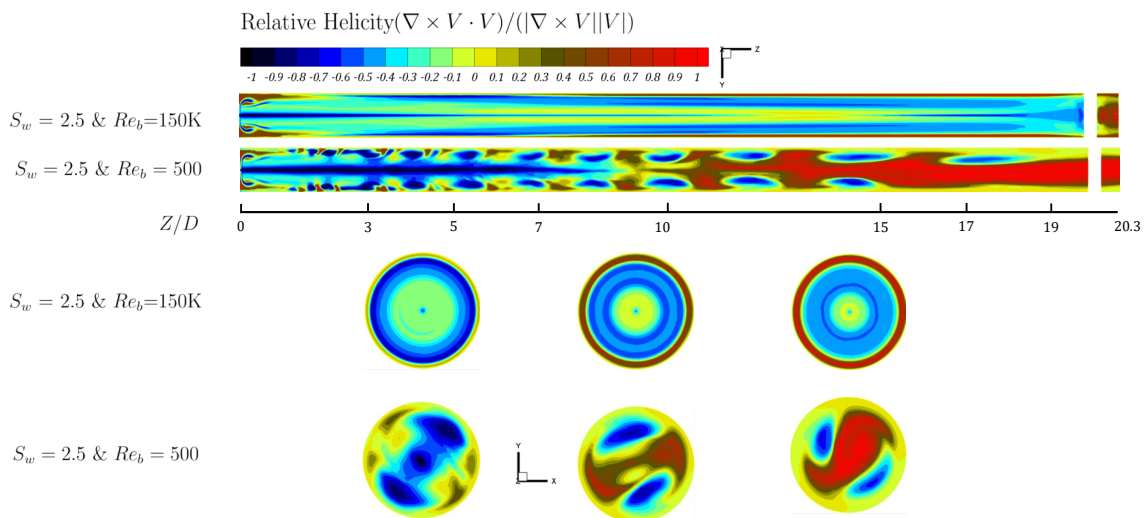


Figure E4: Comparison between unsteady laminar and turbulent swirl flows in a pipe - Structure of the flow

G

Inline swirl separator design $S_w = 0.5$

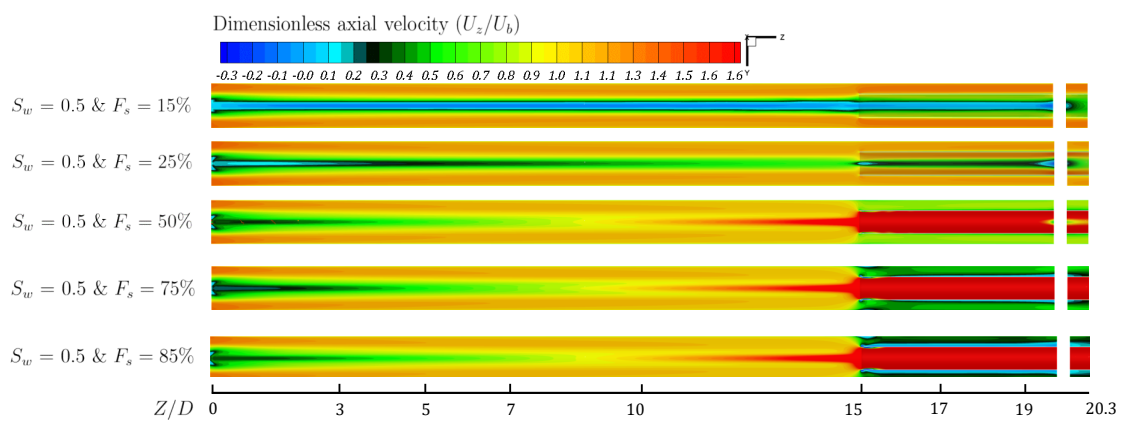


Figure G.1: Dimensionless time-averaged axial velocity for various Flow Splits - $\frac{X}{D} = 0$

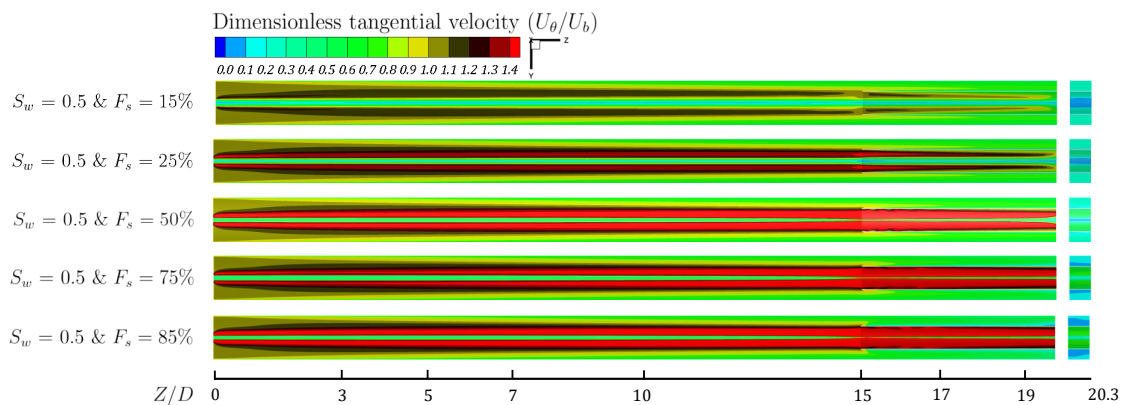


Figure G.3: Dimensionless time-averaged tangential velocity for various Flow Splits - $\frac{X}{D} = 0$

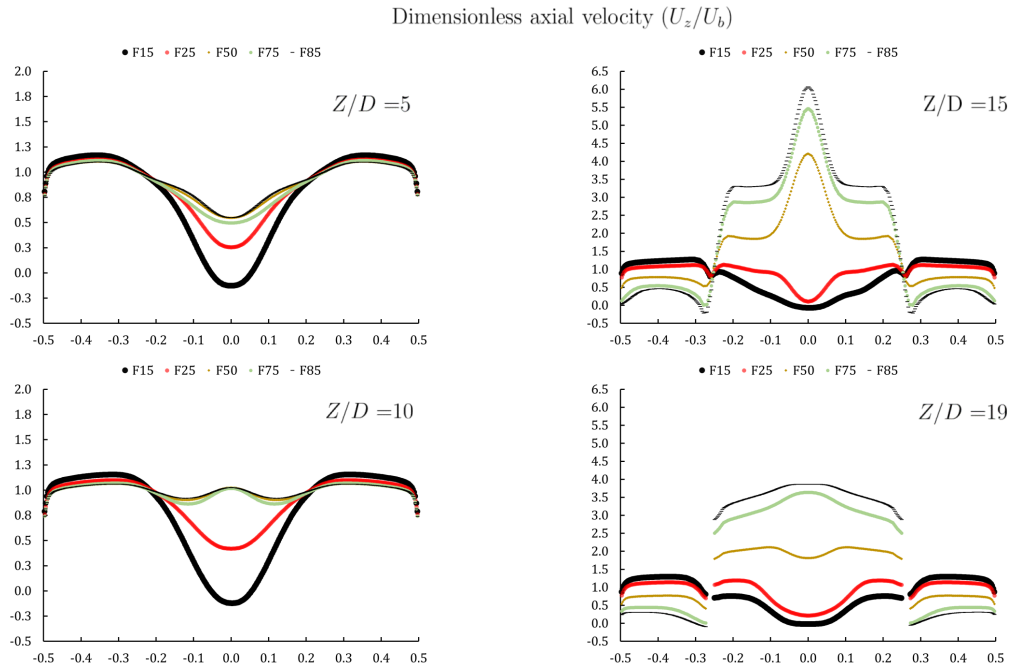


Figure G.2: Dimensionless time-averaged axial velocity for various Flow Splits - Dimensionless radial coordinate

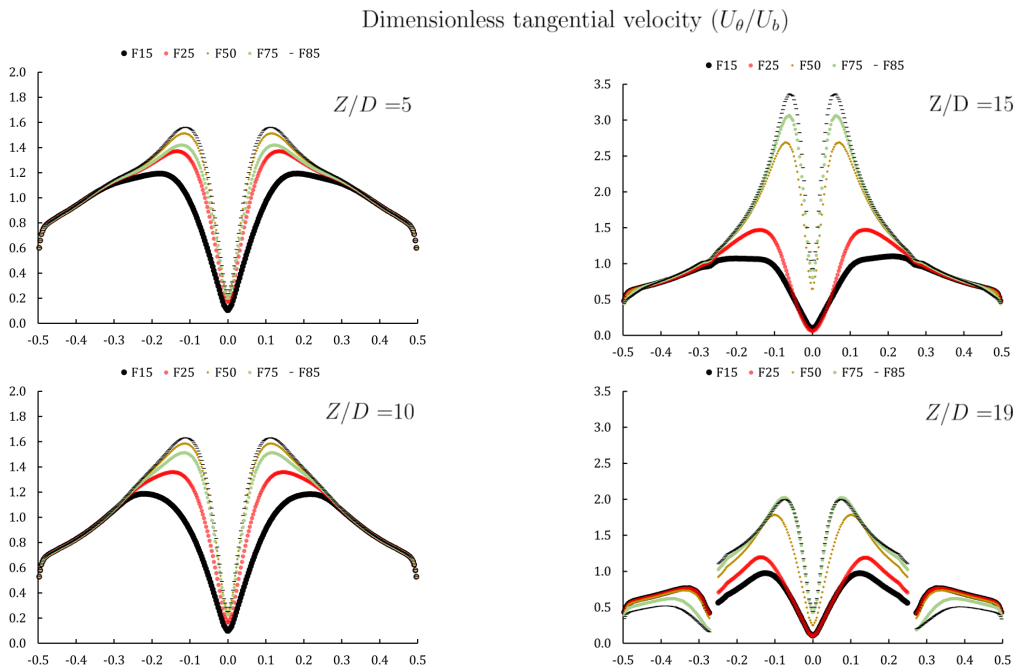
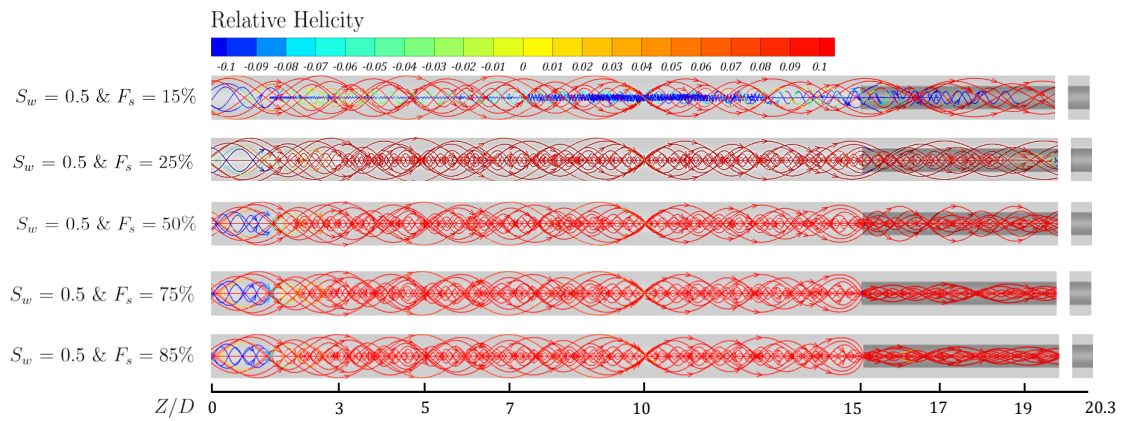
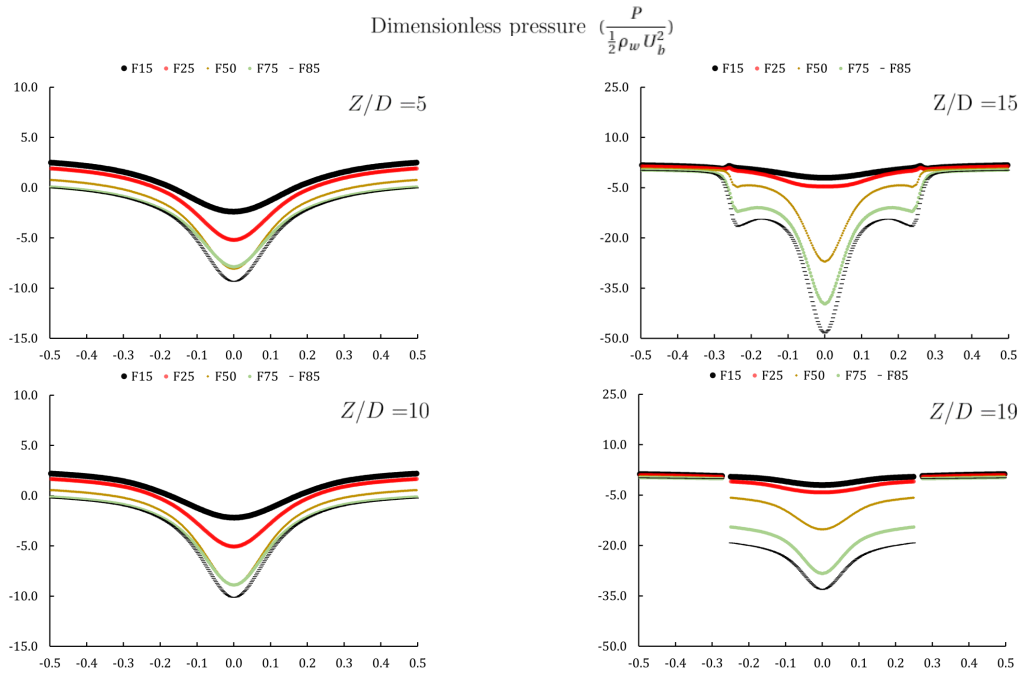
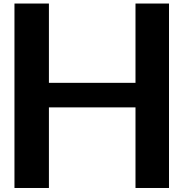


Figure G.4: Dimensionless time-averaged tangential velocity for various Flow Splits - Dimensionless radial coordinate





Inline swirl separator design $S_w = 1.6$

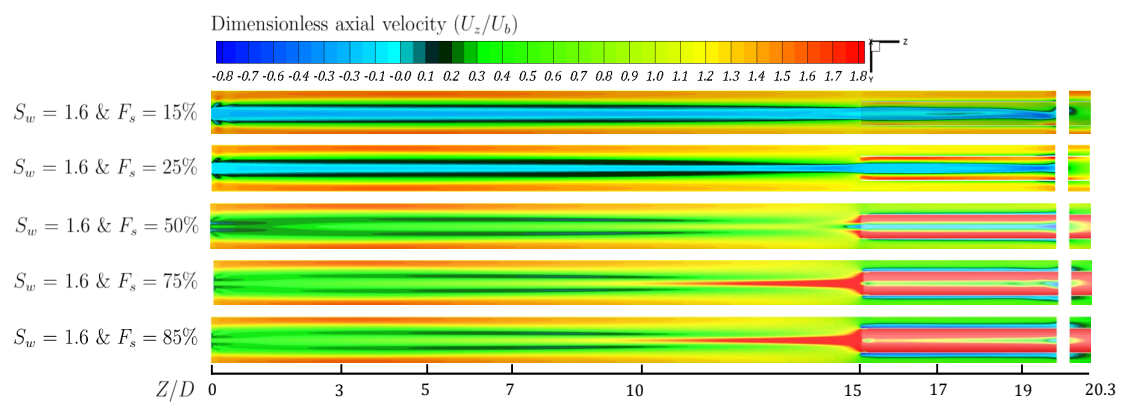


Figure H.1: Dimensionless time-averaged axial velocity for various Flow Splits - $\frac{X}{D} = 0$

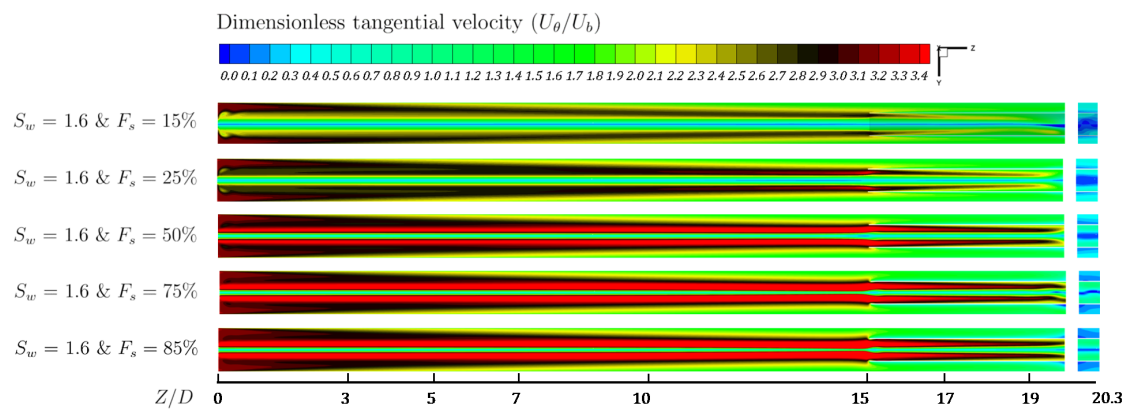
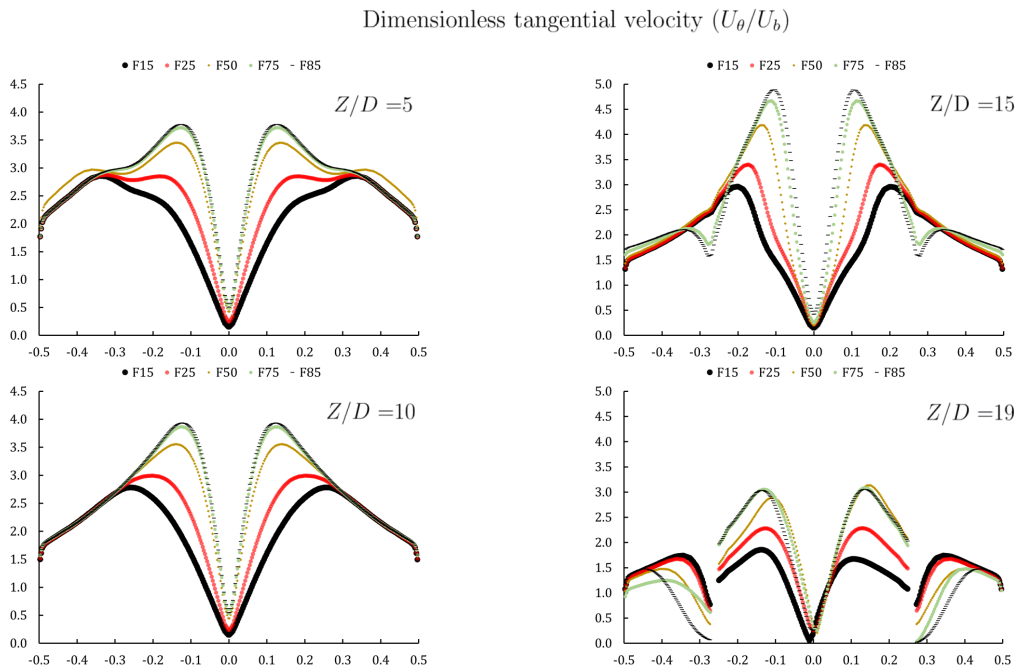
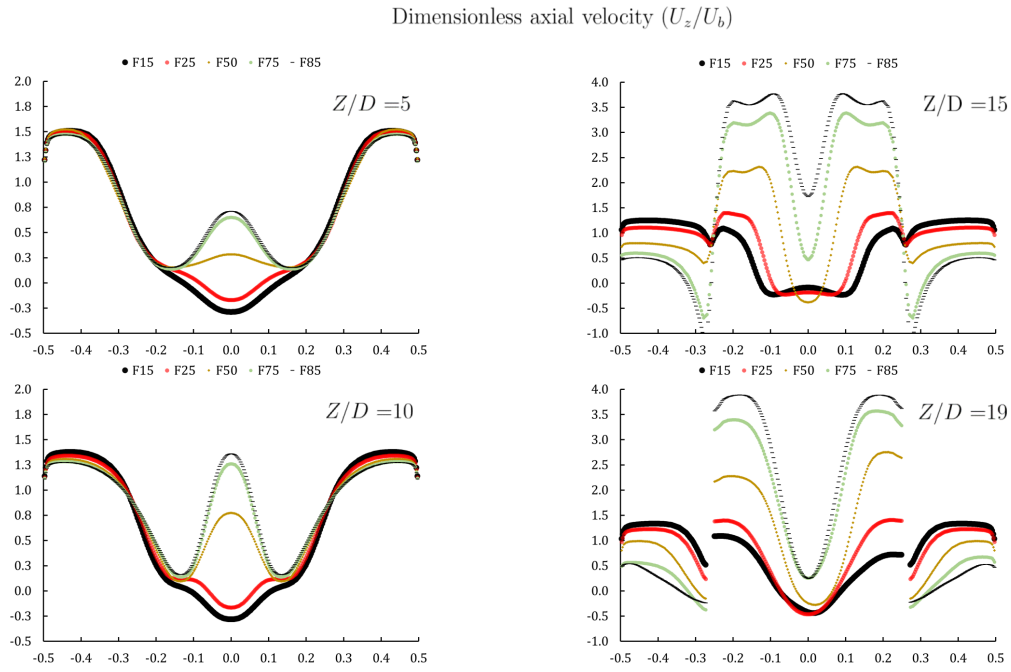
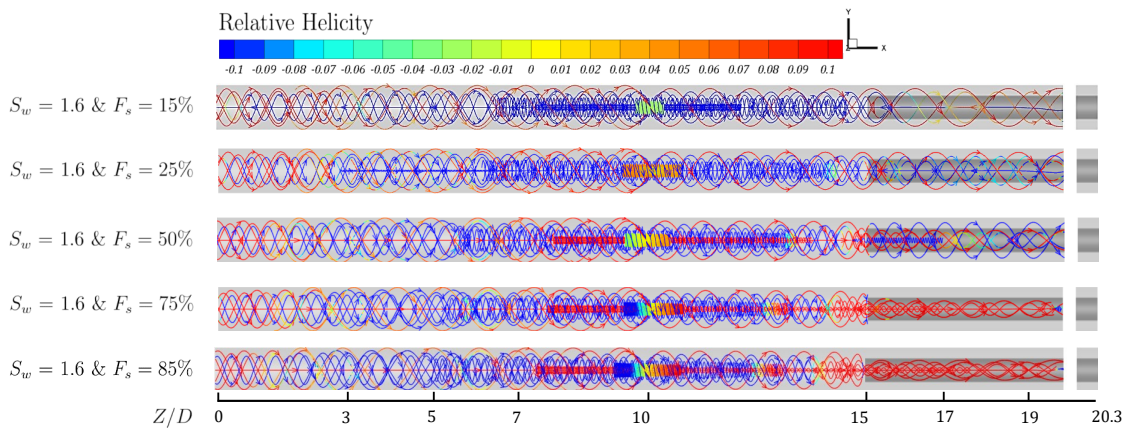
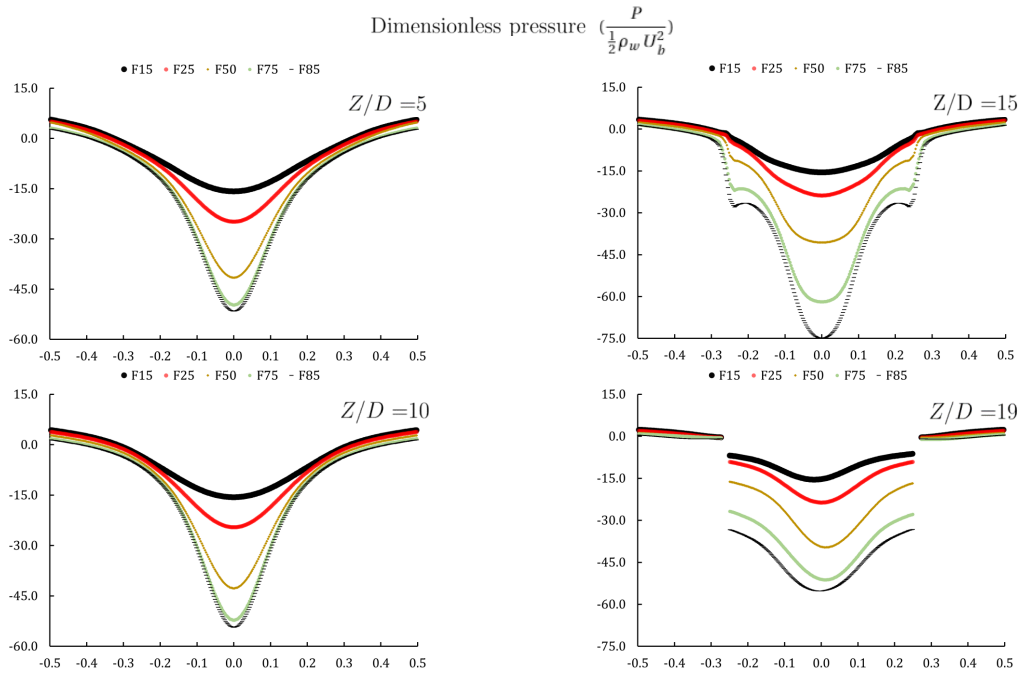


Figure H.3: Dimensionless time-averaged tangential velocity for various Flow Splits - $\frac{X}{D} = 0$





Inline swirl separator design $S_w = 2.5$

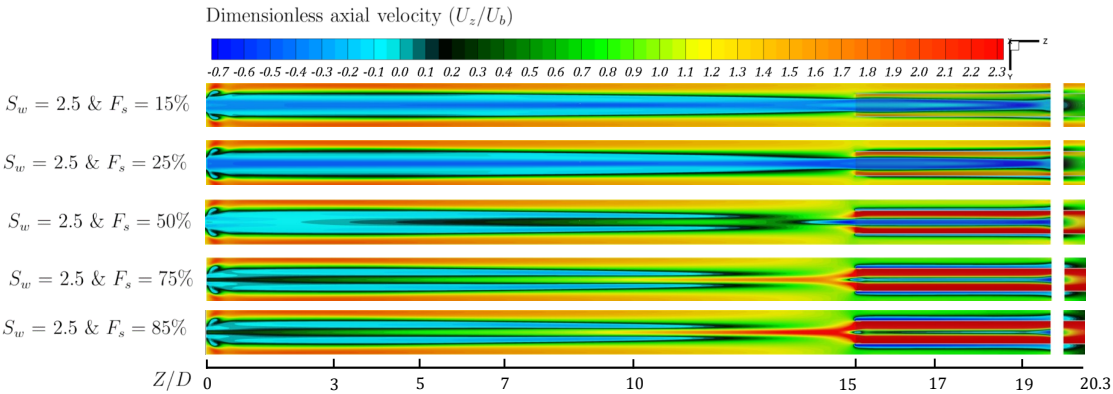


Figure I.1: Dimensionless time-averaged axial velocity for various Flow Splits - $\frac{X}{D} = 0$

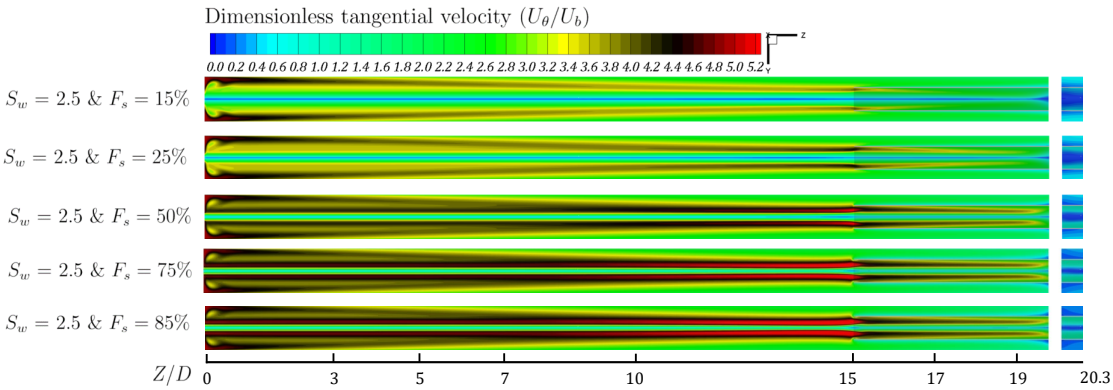


Figure I.3: Dimensionless time-averaged tangential velocity for various Flow Splits - $\frac{X}{D} = 0$

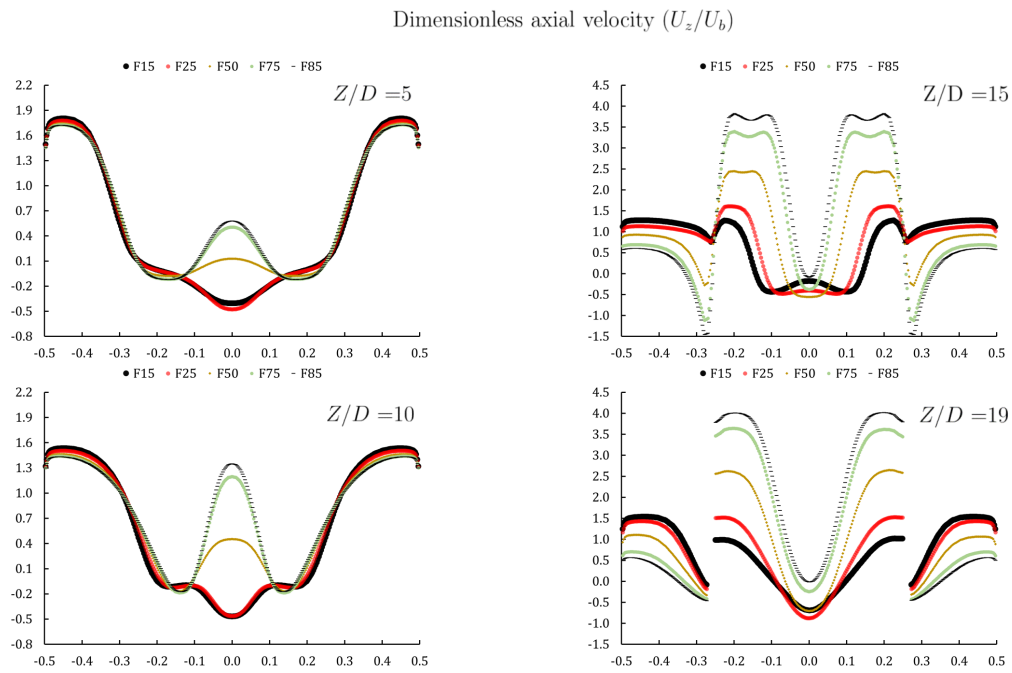


Figure I.2: Dimensionless time-averaged axial velocity for various Flow Splits - Dimensionless radial coordinate

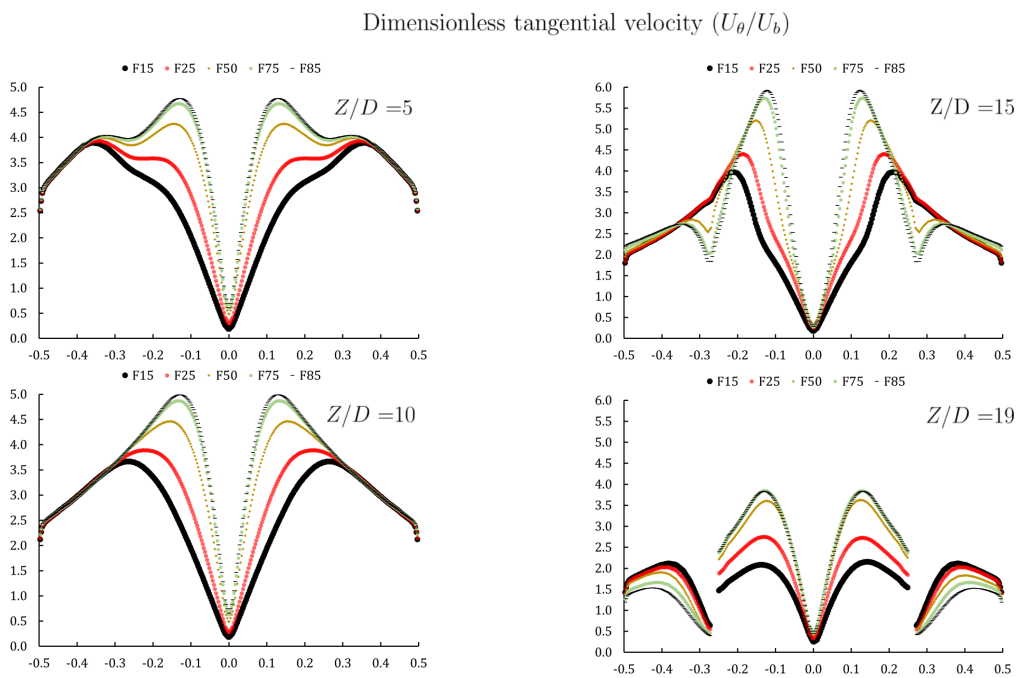
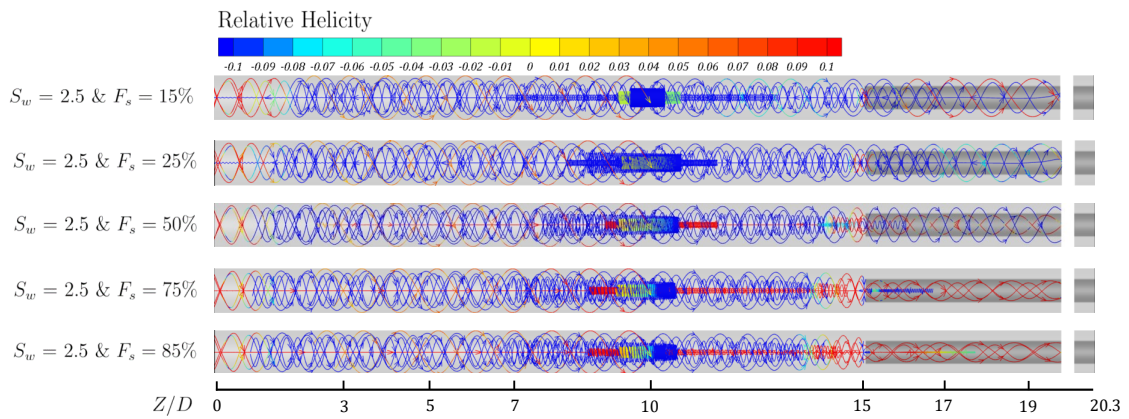
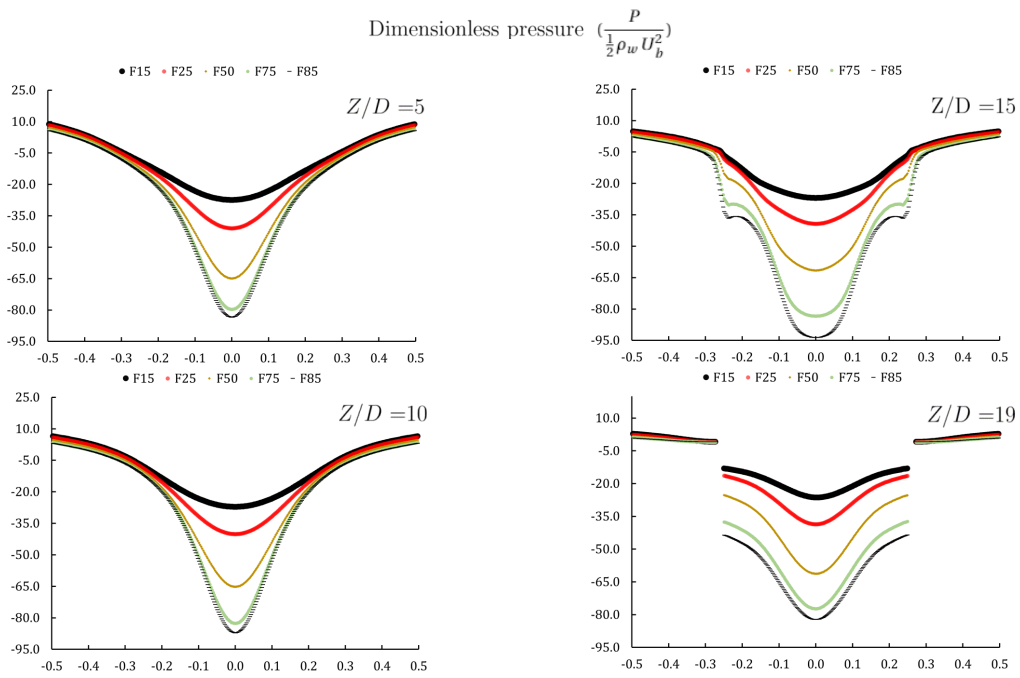


Figure I.4: Dimensionless time-averaged tangential velocity for various Flow Splits - Dimensionless radial coordinate



Bibliography

- [1] L. J. A. M. Van Campen, *Bulk dynamics of droplets in liquid-liquid axial cyclones*, (2014).
- [2] J. J. Slot, *Development of a centrifugal in-line separator for oil-water flows*, (2013).
- [3] S.K.Star, *Pressure distribution in a liquid-liquid cyclone separator* (Delft University of Technology, 2016).
- [4] deZoeten, *Mechanistic model of an inline liquid-liquid swirl separator* (Delft University of Technology, 2018).
- [5] O. Kitoh, *Experimental study of turbulent swirling flow in a straight pipe*, *Journal of Fluid Mechanics* **225**, 445 (1991).
- [6] Y. Levy, D. Degani, and A. Seginer, *Graphical visualization of vortical flows by means of helicity*, *AIAA journal* **28**, 1347 (1990).
- [7] W. Steenbergen, *Turbulent pipe flow with swirl (phd thesis)*, Technische Universiteit Eindhoven, Netherlands (1995).
- [8] M. Dirkzwager, *A new axial cyclone design for fluid-fluid separation*, (1996).
- [9] J. H. Faler and S. Leibovich, *An experimental map of the internal structure of a vortex breakdown*, *Journal of Fluid Mechanics* **86**, 313 (1978).
- [10] S. Leibovich, *The structure of vortex breakdown*, *Annual review of fluid mechanics* **10**, 221 (1978).
- [11] P. Yazdabadi, A. Griffiths, and N. Syred, *Characterization of the pvc phenomena in the exhaust of a cyclone dust separator*, *Experiments in fluids* **17**, 84 (1994).
- [12] F. T. Nieuwstadt, J. Westerweel, and B. J. Boersma, *Turbulence: introduction to theory and applications of turbulent flows* (Springer, 2016).
- [13] S. B. Pope, *Turbulent flows*, (2001).
- [14] C. G. Speziale, S. Sarkar, and T. B. Gatski, *Modelling the pressure-strain correlation of turbulence: an invariant dynamical systems approach*, *Journal of fluid mechanics* **227**, 245 (1991).
- [15] S. Murphy, R. Delfos, M. Pourquie, Ž. Olujić, P. Jansens, and F. Nieuwstadt, *Prediction of strongly swirling flow within an axial hydrocyclone using two commercial cfd codes*, *Chemical engineering science* **62**, 1619 (2007).
- [16] S. Grundmann, F. Wassermann, R. Lorenz, B. Jung, and C. Tropea, *Experimental investigation of helical structures in swirling flows*, *International Journal of Heat and Fluid Flow* **37**, 51 (2012).
- [17] H. Li and Y. Tomita, *Particle velocity and concentration characteristics in a horizontal dilute swirling flow pneumatic conveying*, *Powder Technology* **107**, 144 (2000).
- [18] S. Alekseenko, P. Kuibin, V. Okulov, and S. Shtork, *Helical vortices in swirl flow*, *Journal of Fluid Mechanics* **382**, 195 (1999).
- [19] G. Rocklage-Marliani, M. Schmidts, and V. I. V. Ram, *Three-dimensional laser-doppler velocimeter measurements in swirling turbulent pipe flow*, *Flow, Turbulence and Combustion* **70**, 43 (2003).
- [20] M. Pashtrapanska, J. Jovanović, H. Lienhart, and F. Durst, *Turbulence measurements in a swirling pipe flow*, *Experiments in fluids* **41**, 813 (2006).

-
- [21] H. Vaidya, Ö. Ertunç, B. Genç, F. Beyer, Ç. Köksoy, and A. Delgado, *Numerical simulations of swirling pipe flows-decay of swirl and occurrence of vortex structures*, in *Journal of Physics: Conference Series*, Vol. 318 (IOP Publishing, 2011) p. 062022.
- [22] S. Alekseenko and P. Kuibin, *Theory of concentrated vortices: an introduction* (Springer Science & Business Media, 2007).
- [23] A. K. Gupta, D. G. Lilley, and N. Syred, *Swirl flows*, Tunbridge Wells, Kent, England, Abacus Press, 1984, 488 p. (1984).
- [24] C. Sozou and J. Swithenbank, *Adiabatic transverse waves in a rotating fluid*, *Journal of Fluid Mechanics* **38**, 657 (1969).
- [25] J. Harvey, *Some observations of the vortex breakdown phenomenon*, *Journal of Fluid Mechanics* **14**, 585 (1962).